Transition of Free Convection Boundary Layer Flow

ALI SAAD ABDULLAH ALZWAYI

Transition of Free Convection Boundary Layer Flow

A Thesis Submitted for the degree
of Doctor of Philosophy

in the
School of Engineering
of the
University of Glasgow

By

Ali Saad
BSc, MSc & MPhil

System, Power & Energy Research Division
School of Engineering
University of Glasgow
Glasgow, UK

October, 2013

This work is dedicated to

My parents, my wife, my sons Mohamed and Sanad, my brothers and sisters

Declaration

I hereby confirm that all of the result described in this thesis is the original work of mine. Any published ideas or techniques from the others are fully acknowledged in accordance with the standard referencing practices.

.....

Ali Saad

October, 2013

Abstract

Transition of natural convection flow on a heated flat plate and inside a heated channel is studied numerically. Three different RANS based turbulent k-ε models namely standard, RNG and Realizable with an enhanced wall function are employed in the simulations. Additionally, a Large Eddy Simulation (LES) technique is also applied to particularly investigate the flow field and transition in a heated plate facing upward.

Numerous published papers presented the typical characteristic behaviour of natural convection flow inside a channel, however, none of these provided information about the transition behaviour of flow inside a channel, and importantly, how the transition is affected by the merging of two growing boundary layers which occur inside a channel. Therefore, taking the above important things into consideration, the aim of the study is to carry out in-depth investigations of the transition of the free convection flow inside a channel with an effect of its width, angular orientation and several important thermal and boundary conditions.

Moreover, the transition phenomena of the free convection flow developing in a heated channel facing both downward and upward are thoroughly investigated in the thesis. Numerically predicted results are compared with available experimental data in the published literatures. Fluid properties are assumed to be constant except for the density which changes with temperature and gives rise to the buoyancy forces and is treated by using the Boussinesq approach. Air with a Prandtl number of 0.7 is used as a test fluid in all the simulations.

In the RANS based models, the results show that the Realizable model with an enhanced wall function predicts numerical results well compared to the experiment than those obtained by the other two models (standard and RNG), therefore this model was selected to perform all the other RANS based numerical simulations in this work.

The results particularly indicate that the inclination of the channel has major effects on the transition stage. As the inclination angle is increased, the transition stage moves further downstream of the channel. However, the predicted local heat flux, reached its minimum further upstream of the channel, does not agree with that of the velocity and turbulent kinetic energy in a small channel width.

Natural convection from an isothermal plate is conducted by using a Large Eddy Simulation method. The results show that with an increase in the angle the peak of the thermal and velocity boundary layers move from the near outlet of the plate for the vertical case to the middle of the plate when θ = -70°. So the thermal and boundary layers become fatter which causes an early transition.

Acknowledgements

All the praises be to Allah (God), the Most Merciful and Beneficent. I would like to express my gratitude to my supervisor, Dr Manosh C. Paul, for all his guidance, support and encouragement during this research. His stimulating comments and suggestions have been of immense benefit to me.

Grateful thanks are due to the members of IT Support Team of School of Engineering, especially Mr Walter Robinson and Mr Ken McColl for their constant effort to keep the system always running and help in fixing any problems in the computer systems.

I would like to express my sincere thanks to all the friends and colleagues, Dr Md. Abdul Hye, Mr Blaid Alganash, Mr Najeeb Yahya, Mr Emad Mansour and Mr Ahmed Al Waaly. Their spirited support and encouragement has been of great help to me throughout the relentless endurance test of my PhD.

I am deeply indebted to my beloved parents, wife, sons, sisters and brothers. I owe you all much more than I can possibly express. I am also grateful to all of my well-wishers for their invaluable advice and support that has helped me greatly to make it this far.

Contents

List of Figures

List of Tables

List of Symbols

Roman Symbols

A_0 and A_S, C_1, C_2, $C_{1\varepsilon}$, $C_{2\varepsilon}$ and $C_{3\varepsilon}$ model constants

b	channel width (m)
C_p	air specific heat capacity (J/kg˚C)
Cs	Smagorinsky model constant
$\bar{f}$	generic filtered variable
g	gravitational acceleration (m/s^2)
Gr	Grashof number
G	grid filter function
G_k,, G_b	rate of turbulent kinetic energy and buoyancy force respectively
h	Average heat transfer (W/m^2)
k	kinetic energy of turbulence (m^2/s^2)
k_c	cut-off wave number, m^{-1}
L	channel , plate height (m)
$\dot{m}$	mass flow rate (kg/s)
Nu	average Nusselt number
n_y , n_x, n_z	number of grid nodes in the y , x and y directions respectively
p	pressure (N/m^2)
Pr	Prandtl number
q_p	heat flux of the plate (W/m^2)
Ra	Rayleigh number
Ra^*	modified Rayleigh number
St	Stanton number, $q_p/(\rho C_p U(T_P-T_\infty))$
S_{ij}	strain rate tensor
t	time, s

T	temperature (°C)
u_i or u, v,w	velocity components in Cartesian coordinate, *m/s*
x_i or x, y, z	Cartesian coordinate directions (m)

Greek Symbols

θ	angle of inclination with the respect to the vertical direction
β	thermal expansion coefficient
Γ	exchange coefficient for general transport defined as μ/Pr
ρ	density (kg/m^3)
κ	thermal conductivity (W/m.k)
v	kinematic viscosity (m^2/s)
v_{sgs}	sub-grid scale kinetic eddy viscosity(m^2/s)
ε	dissipation rate of turbulent kinetic energy (m^2/s^2)
C_μ	turbulent viscosity (Pa.s)
δ	thickness of boundary layer (m)
δ_{ij}	kronecker delta
Δx,Δy,Δz	mesh spacing in the x, y, z directions
Δ	filter width
μ	dynamic viscosity coefficient (Pa.s)
μ_t	turbulent molecular viscosity
μ_{sgs}	sub-grid scale eddy viscosity
σ	Kolmogorov velocity scale
σ_t	constant of turbulent Prandtl number
σ_k, σ_ϵ	turbulent Prandtl numbers for k and ε respectively
α	thermal diffusivity (m^2/s)
τij	subgrid scale stresses

Subscripts

a	Air
P	Plate
e	Experimental
n	Numerical
c	Critical
in	Inlet
∞	Ambient

Mathematical Accents

$\bar{.}$	grid filtering
$\tilde{.}$	test filtering
$\lvert . \rvert$	Magnitude

Chapter 1

Introduction

Heat transfer takes place when temperature differences exist within a system or between a system and its surroundings. In Thermodynamics, heat is defined as energy of a system and with a growing concern on environment and energy crisis; the investigation of heat transfer has been an important part of engineering research over the past several years. The applications cover a wide range of areas from the aspects of environmental, atmospheric and geophysical problems to manufacturing systems, space research and heat injection / rejection. The three modes of heat transfer are conduction, radiation and convection, all of these usually occur in most practical systems, where every mode of heat transfer can be investigated separately and the results of heat transfer is then combined to give a total heat transfer rate within systems. However, in some cases heat transfer coefficient from a system may involve a combination of two or three of modes of heat transfer which interact with each other.

Of the conduction and radiation, heat transfer processes, the former occurs when temperature difference exist in the material of a system and also due to the motion of particles which may comprise materials as well as microscopic particles. Diffusion of energy occurs due to the difference in the local temperature and fluid motion. The energy transfer in the radiation however occurs in the form of electromagnetic waves where the energy is emitted from

a material due to the temperature difference, which is larger for large temperature, and is transferred to other surfs through the superseding space.

Convection occurs when there is a relative motion between a surface and a fluid over the surface and there is a temperature difference between the surface and flow. The mechanism of flow on a heated surface is divided into three distinct groups: free convection, forced convection and mixed convection. The movement of mass in free convection depends on the density gradient which is driven by the buoyancy force of the flow, while the flow in forced convection is driven by other external forces such as flow speed and pressure gradient. On the other hand, mixed convection is driven by both free and forced convections. Over recent years, more attention has been given to natural convection as it occurs naturally in environmental systems. Moreover, most practical and economical methods for developing heating and cooling systems use natural convection induced by buoyancy forces.

Many experimental and numerical investigations have been carried out to study the behaviour of the development of convection on various geometries, for instance, cylinder, sphere, flat plate and channel under different boundary and flow conditions. In fact, the natural convection on vertical plates has received more attention because the phenomenon of natural convection is employed in many engineering applications, for example, cooling and heating of industrial and electronic equipment such as transistors, mainframe computers, plate heat exchangers, solar energy collectors, and cooling of nuclear reactor fuel elements. Moreover, by using natural ventilation a building can reduce conventional heating cost by 30% to 70% as reported by Liping and Angui [2004]. So, this is substantially reducing the energy consumption in a modern building. The major application of free convection links with solar energy

systems, e.g. see Wilson and Paul [2011], since natural ventilation systems use natural convection to supply a building with fresh air. A comprehensive literature review of free convection along plates and channels will be presented in the next Chapter.

Most of previous studies were carried out for either laminar or turbulent flow with transition neglected, and very little is known about the transition stage in vertical and inclined channels, where the heated plate of a channel is kept under isothermal condition. In particular, for free convection occurring in a relatively large scale, little reliable information about the transition stage inside the channel can be obtained from experiment and laboratory based experiments in some cases with varying of angular orientation may be a difficult and costly process. So, in this thesis I carry out various numerical simulations to investigate the transition problems mentioned above, and results are validated, where possible, with various experimental data found in the published literature.

Chapter 2

Review of previous works

Numerous researchers have thoroughly investigated the free convection on flat plates or channels in laminar / turbulent flow in the past decades. The most important studies related to the present work are reported in this chapter.

2.1. Natural convection from a flat plate

2.1.1. Vertical flat plate

Early some data of the flow on a vertical heated surface is provided by Griffiths and Davis [1922]. They measured the local heat transfer, temperature and velocity profiles, and poor agreement was obtained between the experimental data and the semi-theoretical results of Eckert and Jackson [1950] which led to suggestions that, the data were inaccurate. In Eckert and Jackson [1950], an integral boundary layer theory, with postulated velocity and temperature fields to develop the solution in turbulent flow, was employed to investigate local heat transfer and thickness of the boundary layer. The range of Grashof number chosen was from 10^{10} to 10^{12}, and the analysis was for the Prandtl number close to 1. The results of these calculations were close to the experimental data of Jakob [1949].

Simon [1952] performed numerical simulations to study the laminar natural convection flow on an isothermal vertical plate for different Prandtl numbers, e.g. 0.01, 0.72, 0.733, 1, 2, 10 and 1000. He investigated extensively the effects

of the Prandtl number on the rate of heat transfer and reported the results of the velocity, temperature and boundary layer thickness of flow, which became a reference data for many recent studies of laminar convection on parallel heated plates.

Empirical correlations based on experimental results have widely been used to predict the thermal properties of flow over an isothermal flat surface. Churchill and Ozoe [1973] and Churchill and Chu [1975] conducted experiments for different Prandtl numbers and for Grashof numbers covering laminar, transition and turbulent regions of flow. An inclusive review of these results is reported in many publications, e.g. see Louis [1993], Bejan [1995], Kakac and Yener [1995], Oosthuizen and Naylor [1999], Lindon [2000], William et al. [2005], Ioan and Derek [2001], Oleg and Pavel [2005], and Mickle and Marient [2009]. Most of these publications covered methods based on similarity solution as well as integral equations which are used for the simulation of convective heat transfer for conditions under which the boundary layer equations apply.

Major experimental works by Cheesewright [1967], Warner and Arpaci [1968] and Miyamoto and Okayama [1982] recorded the main properties of air flow on a large vertical plate ranging from 2.75 m to 5.0 m. Cheesewright [1967] recorded both the local temperature and the velocity of air flow, keeping the Grashof numbers within the range from 10^4 to 1.5×10^{11}. In addition, the structure of the flow in laminar, transition and turbulent flow was presented, which showed good agreement with the experimental results of Eckert and Jackson [1950]. Warner and Arpaci [1968] used smoke to determine the thickness of the boundary layer flow and the location where the flow became turbulent. Satisfactory agreement was obtained with the experimental results of Saunders [1936], but for the local heat transfer remarkable agreement was

obtained compared with the numerical correlation of Bayley [1955]. The characteristics of a boundary layer on a uniformly heated long vertical plate of 5m were examined by Miyamoto and Okayama [1982]. Comparison with various experimental data showed a good agreement particularly in the calculation of local heat transfer.

Characteristic behaviour of flow in the inner boundary layer has been investigated recently by Tsuji and Nagano [2008a, 2008b] and Koleshko et al. [2005], where Tsuji and Nagano used a hot-wire technique to record the turbulent quantities near the wall to present the wall shear stress in the flow. Their results indicated that the temperature fluctuation reached its maximum approximately in the inner layer, while the maximum of the velocity fluctuation recorded in the outer layer. Based on the experimental data, several correlation equations have been developed to characterise the flow behaviour, especially in the turbulent region. Koleshko et al. [2005] also paid attention to the study of the flow structure within the transition (buffer) and logarithmic regions, with a quantitative estimation reported for the structure of temperature in the turbulent boundary layer.

In some other published papers, experimental data were inadequate to provide in-depth understanding on the fundamental characteristics of natural convection flow. Several numerical papers appeared to date to study especially the turbulent boundary layer convection. For that, new wall functions for turbulent natural convection derived by Yuan et al. [1993] become very useful to turbulent flow simulations.

Large eddy simulation of free convection flow on a vertical heated plate was recently performed by Yan and Nilsson [2005] using both isothermal and non-isothermal wall laws. Attention was given to both the velocity and thermal

fields and they found that the intensity of velocity fluctuations at the transition point reaches its peak value. Mean wall shear stress, which was presented as a function of the Grashof number, shows good agreement with the experimental data of Cheesewright and Mirzai [1988].

Direct numerical simulation of natural convection was performed by Abedin et al. [2009] and Abedin et al. [2010]. A second-order Crank-Nicolson scheme was employed in the investigation to estimate the buoyancy terms and the viscosity. A second-order Adams-Bashforth time discretisation scheme was used to calculate thermal properties of air and water for which the Prandtl number was taken as 0.71 and 6.0 respectively. The results show that the mean velocity of air flow has good agreement with the experiments of Tsuji and Nagano [1988b], while in water flow though the measurements data of Tsuji and Kajitani [2006] did not match well for the numerically predicted velocity and temperature near the wall, the comparison of the critical Grashof number was relatively good.

2.1.2. Inclined flat plate

Rich [1953] seems to be the first scientist who carried out investigation on local heat transfer in laminar flow over an inclined plate. Rich focused on the measurement of the temperature field using a Mach-Zehendr interferometer for a set of local Grashof numbers ranging from 10^6 to 10^9. The inclination angle of the plate was varied from 0° to 40°, and his results indicated that the heat transfer coefficient for an inclined plate could be predicted using equations of a vertical plate case if the gravitational term in the Grashof number is taken as a component parallel to the inclined plate.

Levy [1955] modified the theoretical equations for an inclined surface, which was initially set out by Eckert and Jackson [1950], by using the gravitational component parallel to the heated surface. Kierkus [1968] introduced a perturbation to the boundary layer equations of flow to obtain the solutions for the temperature and velocity fields for laminar natural convection over an inclined isothermal plate. He used the Grashof number and plate inclination as the perturbation parameter, and by using a similarity solution for an isothermal vertical surface as the zeroth-order approximation, he determined a first order approximate solution for angles over 40°. The temperature, velocity, and local heat transfer results of Kierkus agreed well with those obtained by Rich [1953].

Later Tritton [1963a, 1963b] reported results of the turbulent natural convection flow of air over an isothermal heated plate. In Tritton [1963a] the temperature and velocity results were obtained but there was no indication of the range of Grashof number, whereas in Tritton [1963b] a fibre anemometer was used to record the transition point as well as the full turbulence stage on an isothermal plate. Information of the range of Grashof number, where the transition takes place, are recorded in this case. In the vertical plate case, Tritton reported that the critical Grashof number at which the flow transition occurs was 9.26×10^6, which is much lower than the previously published experimental data. Tritton, however, mentioned that this was due to the strong disturbances in the laboratory room and the method of investigation was not properly designed to measure the critical distance.

Vliet [1969] seems to be the first who reported experimental results of the local heat transfer of free convection on a constant heat flux inclined plate using both air and water as the test fluids. The experiment was for the Rayleigh number ranging from 10^7 to 10^{16} with an inclination angle of the plate varied

from its vertical position. The results were presented for laminar, transitional, and turbulent stages. But, the effects of trailing, side edges and leading edge of the plate on the heat transfer and flow regions were not presented. In the laminar flow region along the vertical plate the experimental data was found to correlate well with theoretical predictions as well as with Rich [1953]. The transition of the flow from laminar to turbulent region was found to be strongly affected by the plate inclination angle, and the critical Rayleigh number at the transition stage obtained was 10^{13} for the vertical plate and ~10^{8} for a surface inclined at an angle of 30 degrees to the horizontal.

Using a mass transfer technique, experiments were carried out by Lloyd and Sparrow [1970] to establish a relationship between the inclination angle of the plate and the nature of flow stability, where the angular dependence of the Rayleigh number on the onset of instability were determined. The range of angles was between -10° and 60° where a positive inclination angle indicates that the heated plate is facing upward. The results showed that, for an inclination angle $\theta \leq 14°$, waves are the primary mode of instability, while for $\theta > 17°$ the instability is characterised by longitudinal vortices.

Hassan and Mohamed [1970] measured the local heat transfer on an isothermal plate. The angle of inclination was varied from -90° to 90°, as the study particularly focused on the transition of flow on both downward and upward facing heated surfaces. However, their results did not show any transition stage for the downward facing heated surface due to the short length of the plate used in the experiment. However, the transition behaviour for the upward case was summarised, and correlation equations were suggested for presenting flow parameters at the transition region.

Turbulent free convection on a vertical / inclined upward and downward facing heated plate was investigated by Vliet and Ross [1975] under a uniform heat flux condition. Data were measured for the inclination angle ranging from 0° to 80° (downward facing), as well as from the vertical to 30° (upward facing). The experimental results confirmed the location of transition to be a function of the inclination of the plate and the local Nusselt number was correlated with a single equation in which gravity was taken as a component along the plate. On the other hand, Black and Norris [1975] used a differential interferometer to provide flow visualisation and measure the local heat transfer for natural convection from an inclined isothermal plate. They indicated that the flow structure within the turbulent thermal boundary layer can be separated into a thermal sub-layer and a core region that contains random fluctuations. The thermal sub-layer was shown to contain "thermal waves" that traversed the heated plate and caused significant variations in the local heat transfer coefficient and an overall increase in the heat transfer rate in the transition flow region did not affect the results in the turbulent flow region. The results for the local Nusselt number agreed with those obtained by other researchers.

AL-Arabi and Sakr [1988] provided local and average heat transfer data for the heat transfer of free convection flow of air from an isothermal vertical plate as well as an inclined heated plate facing upward. The angular range covered 0° to 80°, and the experiments covered both the laminar and turbulent regions. Their results of local transition data also agreed well with the previous data of Hassan and Mohamed [1970] for all the angles. However, a comparison with the data of Lloyd and Sparrow [1970] showed an uncertainty level of ±25% when $0° \leq \theta \leq 45°$, while comparison with the data of Lloyd and Sparrow [1970] for $\theta > 45°$ showed an under prediction.

2.1.3. Flow visualisation

The first flow visualisation experiments which dealt with transition of free convection flow over an inclined plate were conducted by Sparrow and Husar [1969] and Lloyd and Sparrow [1970]. An electrochemical technique in water was used to visualise the flow field over an isothermal inclined plate. They established a relationship between the inclination angle of the plate and the instability of the boundary layer of the flow, and their experimental data showed that the onset of transition was characterised by longitudinal vortices. Instability, transition and turbulence in buoyancy induced flows were reported by Gebhart [1973] where two different kinds of instability such as thermal and hydrodynamic instabilities were investigated with particularly their effects on transition on vertical, horizontal and inclined surfaces. Black and Norris [1975] also provided flow visualisation and data of local heat transfer coefficient for natural convection on an inclined isothermal plate. They found that the thermal sub-layer was shown to contain thermal waves, which traversed the surface of the heated plate and subsequently caused significant variations in the local heat transfer.

Experiments to visualise the transient flow field of free convection over an inclined plate was carried out by Komori et al. [2001] using a liquid crystal sheet as well as florescent paint in water where the plate inclination was tested in the range of 20^o to 75^o under a constant surface heat flux condition. The visualisation indicated that the separation of the boundary layer moved upstream with decreasing the plate angle. They further reported a new correlation between the heat transfer rate for visualisation of flow and temperature fields where the local Nusselt number in the transition range was proportional to the one-third power of the local modified Rayleigh number.

Natural convection over an upward facing inclined plate was visualised experimentally by Kimura et al. [2002] and Kimura et al. [2003] in order to observe the start of the mechanism of transition from laminar to turbulent flow. The flow fields over the heated plate and the wall temperature were visualised by fluorescent paint and liquid–crystal thermometry respectively. The visualisation indicated that the separation of the boundary layer takes place and the onset of streaks appears over the inclined plate when a modified Rayleigh number exceeds a characteristic value of each inclination angle.

2.2. Natural convection in channels

2.2.1. Vertical channel

In 1942 the first experimental work on buoyancy driven convection flow in a parallel walled vertical channel was done by Elenbaas [1942] using air as a test fluid. Results were presented for a set of inclination angles of the plate varying from 0˚ to 90˚, and particular attention was given to the prediction of the heat transfer coefficient. A good agreement was obtained between the theoretical and experimental data. One of his key findings was that the solution on the single plate would have to be approached for large plate spacing.

Bodia and Osterle [1962] performed the first numerical simulation of buoyancy induced flow developing on a vertical channel. The governing equations were expressed in finite difference form and the walls were treated as isothermal. The air flow velocity and heat transfer coefficient were provided, and validated with those of theoretical and experimental data of Elenbaas [1942]. Later the numerical techniques of Bodia and Osterle [1962] were widely used by many researchers to solve for the free convection in vertical channel with different

boundary and operating conditions, e.g. see the work presented in Miyatake and Fujii [1972], Aung et al. [1972] and Oosthuzien [1984].

Streamwise development of the turbulent free convection flow between two vertical plates was investigated experimentally by Miyamoto et al. [1983] and Katoh et al. [1991]. The test fluid in this case was also air and different width of the channel was examined. In Miyamoto et al. [1983] the channel was installed at various height from floor, e.g. 10, 90, 170 and 465 mm. The experimental data demonstrated that heat transfer coefficients in the vertical heated plate of over 2 m long are almost independent to the height of the channel when positioned 10 mm above the floor. In Katoh et al. [1991] a bell mouth was installed at the bottom of the channel, and the heat transfer between the channel with a bell mouth and without it was compared. The results showed that the heat transfer was similar in the two cases.

Numerical analysis of the turbulent convection of air in a symmetrically heated vertical parallel plate channel was done by Fedorov and Viskanta [1997]. The heated plate was tested with different values of heat flux. A low Reynolds number k-ε turbulent model was used in this analysis, and a finite difference numerical simulation technique was employed to solve the two-dimensional momentum and energy equations. The results of the local heat flux and Nusselt number distributions was reported and compared with the experimental data of Miyamoto et al. [1986]. The results particularly indicated that the transition point moves further downstream of the channel when the turbulent intensity at the inlet is increased. Two-dimensional numerical simulations of turbulent natural convection in a heated channel were performed by Said et al. [2005] and Badr et al. [2006]. The governing equations were solved by the finite volume discretisation method assuming all the thermal properties of the air to be constant, except the density which was solved by the Boussinesq

approximation. Specifically, Badr et al. [2006] covered a wide range of thermo physical aspects of the problems as well as geometrical ratios of the model. They also compared their results with the experimental data of Miyamoto et al. [1986] and presented numerical correlations for the average of heat transfer in terms to channel aspect ratio and Rayleigh number.

Another work on the natural convection in a vertical channel was recently reported by Ben-Mansour et al. [2006]. Different inlet boundary conditions of the turbulent flow were tested; e.g. uniform inlet pressure, adiabatic inlet, and uniform inlet velocity. Numerical results of five different k-ε turbulent models (standard, low Reynolds number k-ε of Launder and Sharma [1974], low Reynolds number k-ε of Yang and Shih [1993], Renormalization Group (RNG) k-ε, and Reynolds stress) were presented. Steady state and two-dimensional numerical models were developed and the results showed that the thermal field, obtained by the low Reynolds number k-ε model of Yang and Shih [1993] with a uniform pressure inlet condition, was very close to the experimental results of Miyamoto et al. [1986].

Experimental and numerical studies were made by Yilmaz and Fraser [2007] and Yilmaz and Gilchrist [2007]. Three different low Reynolds number k-ε turbulence models were employed in this work which are Davidson [1990], Lam and Bremhorst [1981] and To and Humphrey [1986]. A comparison between numerical results and experimental data was obtained. In Yilmaz and Fraser [2007] the comparison between numerical and experimental results was reported for a plate temperature of 100°C. The results particularly indicate that the turbulent model of Lam and Bremhorst underestimates the heat transfer when comparing with the experimental data while it overestimates mass flow. However, for the To and Humphrey model, both the heat transfer and mass flow were overestimated, and the Davidson model predicted similar result for

the mass flow but not for the heat transfer. In Yilmaz and Gilchrist [2007] the heated plate was kept under a uniform heat flux condition, and the temperature results, estimated by Lam and Bremhorst model, were very close to that of the experimental data. In this case the To and Humphery model showed an overall under prediction, but gave a good prediction of the peak temperature compared to the other turbulent models. The best prediction for the velocity distribution was found by the models of To and Humphery and Davidson.

Understanding heat transfer of free convection in vertical channels also receives a great deal of attention in heating / ventilation of buildings. In this context, natural convection phenomena inside channel have been recently investigated by Bacharoudis et al. [2007] experimentally and theoretically. The application was solar chimneys and the heated plate was assumed to be isothermal. Numerical simulation of thermofluid phenomena was carried out with six k-ε turbulent models, but the realizable k-ε has proved to be the best suited model for this application. In addition, an enhanced wall treatment was employed to solve the laminar sublayer developing in turbulent flow, and the governing equations were solved in a two dimensional domain by using the finite volume method. For the boundary condition setup, the inlet and outlet temperatures of the flow were set to ambient temperature, where the Rayleigh number has been estimated as 1.0392×10^{11}. Results of both the temperature and velocity profiles were presented with the Nusselt number correlated with the channel length and width.

In another recent study, thermal efficiency of flow in a vertical chimney (open ended channel) has been experimentally investigated by Burek and Habeb [2007]. From the experimental data some correlations have been obtained to calculate the mass flow rate of air as well as temperature. The major finding was that the mass flow rate is affected by both the channel depth and heat input

to the system with the thermal efficiency remaining unaffected by the depth of the channel. Taofeek et al. [2008], on the other hand, used Particle Image Velocimetry method to record turbulent characteristics of free convection in channel with anti-symmetric heating. Data was provided for two values of Rayleigh number, 1×10^8 and 2×10^8. The results indicated that the distributions of the velocity and temperature of the flow in this experimental model of vertical channel are similar to those in a closed cavity. And, with increasing the Rayleigh number by 50%, the location of peak velocity moved close to the surface wall, which has close agreement with data recorded a closed cavity. Further experimental results of developing natural convection in a heated channel with enclosure space have been published by Hatami and Bahadorinejad [2008]. Velocity and temperature of the flow inside the channel were measured by a hot wire anemometer, and exponential results suggest that the Nusselt number depend on the Rayleigh number as well as on the aspect ratio of the channel.

Low Reynolds number k-ω turbulent models has also been used to study the behaviour of developing buoyancy flows in a vertical channel, for example see the work of Zamora and Kaiser [2009]. They considered two heating conditions: uniform heat flux and uniform wall temperature. The work particularly covered a wide range of Rayleigh number from 10^5 to 10^{12}, and the test fluid used in the simulation was air. All the thermal properties of the flow were assumed to be constant except the density, which was solved by the Boussineq approximation. For the isothermal case, numerical results of the average of Nusselt number did show a level of agreement with those in Kaiser et al. [2004].

2.2.2. Inclined channel

As far as the flow of free convection on a tilted plate is concerned, the first experiment was carried out by Rich [1953]. Average heat transfer rate along the heated plate at various angles up to 40° was measured. After about 3 decades, Azevedo and Sparrow [1985] performed a comprehensive experimental study of laminar free convection in an inclined isothermal channel. They investigated three heating models: heating from above, heating from below, and symmetric heating, where the channel was closed from both sides. The average of Nusselt number was evaluated in all the experimental conditions in the range 0° to 45° from the vertical position, and they reported the data in a global correlation with an average error of ±10%. Later, the study of Manca et al. [1992] concerned a tilted channel with uniform heat flux, the experimental data was performed at different width / spacing (20, 32.25and 40 mm) with various angles of inclination from 0° to 90° and heat flux between 14 and 250 W/m^2. The Nusselt number of the inclination angle was reported in a single equation which became a function of the Rayleigh number for all the cases.

Onur et al. [1997] and Onur and Aktas [1998] provided experimental data of the effect of the inclination angle and width on developing heat transfer between inclined parallel plates with different heating conditions. In particular, Onur et al. [1997] considered the lower plate isothermally heated with the insulated upper plate, while in Onur and Aktas [1998] the upper plate was heated isothermally whereas the lower one was insulated. The channel inclination was varied from 0° to 30° and 45° with a range of Rayleigh number tested between 3×10^7 and 9×10^7. The measurement was carried out for different plate and air temperatures and the results indicated that both the inclination and width influence the heat transfer rate.

Numerical investigation of the free convention in an inclined channel was carried out by Baskaya et al. [1999]. However, they focused only on laminar convection flow. Recently, two-dimensional turbulent natural convection flow inside an inclined parallel walled channel has been studied numerically by Said et al. [2005a, 2005b], keeping both the upper and lower plates isothermal. They used the k-ε turbulent the model and the results obtained satisfactory agreed with those of Elenbaas [1942], Miyamoto et al. [1983], and Fedorov and Viskanta [1997]. Their results further indicated that the average Nusselt number is reduced with an increase in the plate angle. However, the process of transition that occurs from laminar to turbulence was not considered in the study. In fact, the most of papers cited above either considered laminar or turbulent flow and neglected the transition of developing free convection in an inclined channel.

2.3. Objectives of the thesis

From the literature review above, it has been clearly seen that several researchers have studied, theoretically or experimentally, the free convection flow developing over heated plates. However, as far as the flow of free convection inside a channel is concerned, most of the previous studies were carried out either for laminar or turbulent flow neglecting the process of transition that occurs between the laminar and turbulent flow, and therefore, little information is available in the literature about the flow transition of natural convection. Moreover, there is no published work that especially covers the application of natural convection in a large channel with high Grashof number. Furthermore, the majority of the cited papers in this Chapter presented the results of velocity, temperature and turbulence parameters across the boundary layer (horizontal direction) of a channel. None of these papers provides information of these along the boundary layer (e.g. in the vertical

direction), which are important to investigate the transition stage from the laminar to turbulent flow. Accordingly, the main topic and objectives of this study are highlighted in the bullet points below:

1- Critical distance and thickness of the boundary layer along an isothermal heated plate will be investigated analytically at different positions along the flow with different flow temperatures.

2- Analyse three different RANS based turbulent k-ε models, namely standard, RNG and Realizable with two different near wall treatment: standard wall function and enhanced wall function. Validation with experimental data available in the literature is given as well.

3- Effect of plate and air temperatures on the transition stage in a vertical channel is investigated. In addition, particular attention is given to the effect of channel width on the transition stage.

4- Effects of the width and angle of channel on the transition stage will also be examined under various thermal conditions by using local variations of velocity, turbulent kinetic energy and heat transfer. In addition, the main outlet parameters of the flow will be reported.

5- LES is employed to investigate the free convection flow and its transition on an inclined surface. Particular attention is paid on the 3D visualisation of flow and thermal fields.

6- Compare the results obtained by the various numerical simulation methods in the present work with those obtained by other investigators in order to refine and verify the accuracy of numerically predicted results.

2.4. Thesis outline

Chapter 1 presents a general background on the different types of heat transfer mode and their fundamental processes. Particular attention is given to the natural convection flow and its wide range of engineering applications.

Chapter 2 provides a literature review of previous research related to the present work.

Chapter 3 describes the mathematical formulations which are used in the analytical investigation. Governing equations for an incompressible fluid flow and heat transfer with three different RANS based turbulent k-ε models namely standard, RNG and Realizable are explained. Finally, the Large Eddy Simulation (LES) technique is presented which is used for investigating flow transition and turbulence in a three-dimensional model.

In Chapter 4 Analytical results of the boundary layer of natural convection air flow on a vertical heated plate are presented for both isothermal and constant heat flux plates and compared with different previous experimental studies.

In Chapter 5 Steady natural convection through a two-dimensional vertical channel is studied by applying the three turbulent models (standard, RNG and Realizable). In addition, effects of two near wall boundary conditions (standard wall function and enhanced) are investigated. The channel width was varied and the numerical results of the flow velocity, turbulent kinetic energy are

presented along the channel to examine the critical distance and transition of the developing flow.

In Chapter 6 Free convection in a vertical channel, where both the plates are kept under isothermal conditions, are considered and a comparison is given with the results obtained in Chapter 5.

In Chapter 7 Effects of the inclination and width of the channel on the free convection in an inclined parallel channel are investigated. The upper isothermally heated plate of the channel faces downward and the transition process is summarised under a set of parametric variation of physical conditions such as angular orientation, channel width etc.

In Chapter 8 Transition of free convection flow of air over a heated surface is investigated numerically by a Large Eddy Simulation method. Particularly we focus on how the transition is affected by the inclination angle of the heated plate facing upward.

In Chapter 9 The findings of the above investigations are summarised and some suggestions are made for future research in this area.

2.5. Publications from the thesis

2.5.1. Journal papers

1. A. S. Alzwayi & M. C. Paul (2014) "*Transition of free convection flow inside an inclined parallel walled channel: effects of inclination angle and width of the channel*", International Journal of Heat and Mass Transfer, v68, pp194-202.

2. A. S. Alzwayi & M. C. Paul (2013) "*Effect of width and temperature of a vertical parallel plate channel on the transition of the developing thermal boundary layer*", International Journal of Heat and Mass Transfer, v63, pp20-30.

3. A.S. Alzwayi & M. C. Paul, "*An analytical investigation of the physical dimensions of natural convection flow on a vertical heated plate*", Submitted to Heat and Mass Transfer.

4. A.S. Alzwayi, M. C. Paul & S. Navarro-Martinez, "*Large Eddy Simulation of Transition of Free Convection Flow over an Inclined Upward Facing Heated Plate*", In preparation for International Journal of Heat and Mass Transfer.

2.5.2. Papers in conference proceedings

1. A.S. Alzwayi & M. C. Paul (2013) "*Large Eddy Simulation of Transition of Free Convection Flow over an Inclined Upward Facing Heated Plate*", Proceedings of the 13th UK Heat Transfer Conference, UKHTC2013, Imperial College London, 2-3 September 2013.

2. A.S. Alzwayi & M. C. Paul (2012) "*Effect of width of a vertical parallel plate channel on the transition of the developing thermal boundary layer*", Proceedings of Computational Heat Transfer CH12, 1-6 July, Bath, UK, ISBN: 978-1-56700-303-1.

3. A.S Alzwayi & M. C. Paul (2010) "*An analytical investigation of the physical dimensions of natural convection flow on a vertical heated plate*", Proceedings of the World Congress on Engineering, June 30-July 2, 2010, London, UK, ISBN 978-988-18210-7-2, Vol II, pp1404-1408.

2.5.3. Other conference Talks/Posters

1. A.S. Alzwayi & M. C. Paul (2013) "*Large eddy simulation of transition of free convection flow over an inclined upward facing heated plate*", Scottish Fluid Mechanics Meeting, 29 May 2013, Aberdeen, UK.

2. A.S. Alzwayi & M. C. Paul (2010) "*Estimation of the dimensions of a solar heating system*", 3rd Scientific Symposium for Libyan Students in the UK, Sheffield Hallam University, 12 June 2010.

3. A.S Alzwayi & M. C. Paul (2010) "*Estimation of the physical dimensions of a natural convection heating system*", 23rd Scottish Fluid Mechanics Meeting, University of Dundee, 19 May 2010 (poster).

Chapter 3

Analytical and numerical methods

3.1. Analytical methods

In this section, methods used in the analytical investigation of free convection flow on a vertical heated plate are described.

3.1.1. Laminar flow on an isothermal plate

The growth of the boundary layer in natural convection and its transition from the laminar to turbulent state depend on many thermal and physical parameters such as T_P, T_∞, Pr, Gr, Ra and L. For a laminar free convection flow on an isothermal heated plate, the thickness of the boundary layer δ calculated by Holman [2002] as

$$\frac{\delta}{y} = 3.93Pr^{-1/2}(0.952 + Pr)^{1/4}\left(\frac{Ra}{Pr}\right)^{-1/4} \quad (3.\ 1)$$

where the Rayleigh number of the flow is defined as $Ra = Gr.\ Pr$,

$$Gr = \frac{g\beta(T_P - T_\infty)y^3}{\nu^2} \quad (3.\ 2)$$

and y is the longitudinal coordinate; distance from the leading edge of the plate, g is the gravitational acceleration, β is the thermal expansion coefficient of air, and ν is the kinematic viscosity of the fluid. The experimental results of

Incropera et al. [2001] and Louis [1993] suggest that the flow on a vertical isothermal plate becomes turbulent at $Gr \geq 10^9$, and approximately at this critical height ($y = L_C$) of the plate, determined by Equation (3. 3), the thickness ($\delta = \delta_c$) of the boundary layer in laminar flow becomes largest.

$$L_C = \sqrt[3]{Ra\nu^2 / (g\beta(T_P - T_\infty)Pr)} \tag{3. 3}$$

3.1.2. Turbulent flow on an isothermal plate

Several studies show that the local velocity and temperature within the region of a turbulent flow are significantly affected by the turbulent shear stress, and to date much attention is paid only to the theoretical and experimental investigation of the turbulent flow on a vertical isothermal plate. However, the majority of the equations used to determine the thickness of the boundary layer contain the fluctuating components of the turbulent flow, which in many analytical calculations are ignored. According to Kays and Crawford [1980], equation of shear stress is determined from

$$\tau = 0.0225\rho U^2 \left(\frac{\nu}{U\delta}\right)^{1/4} \tag{3. 4}$$

where U is the mean velocity of flow caused by the buoyancy and obtained from $U = \frac{\nu\sqrt{Gr}}{L}$.

The Stanton number, St is defined as a function in the rate of heat convection and shear stress as

$$St = \frac{q_p}{\rho CpU(T_P - T_\infty)} = \frac{\tau}{\rho U^2} Pr^{-2/3} \tag{3. 5}$$

The thickness of the boundary layer in turbulent flow is then approximately determined from Equations (3. 4) - (3. 5)

$$\delta = \left(0.0225 \left(\frac{\nu}{U}\right)^{1/4} \mathrm{Pr}^{-2/3}\, \mathrm{St}^{-1}\right)^4 \tag{3. 6}$$

The equations, which are used to determine the thermal properties is written as

$$\emptyset = \sum_{i=1}^{i=n} a_i T_f^i + b \qquad i \neq 0 \tag{3. 7}$$

where $\emptyset$ indicates the thermal property of the flow, *a* and *b* are unknown parameters, and *n* is the number of segments. Properties of air and water, reported by Kays and Crawford [1980], were used as data in Equation (3. 7). The thermal-physical properties of air flow (e.g. ν, *Pr*, *k*, C_P, ρ) determined as a function of the reference temperature $T_f = T_P + 0.38(T_\infty - T_P)$. They are determined by using Equation (3. 8)

Properties of air flow, $273 \leq T_f\,(K) \leq 373$ (3. 8)

$$\nu = \left(43.78894 - 0.4261292T_f + 1.5941113 \times 10^{-3}T_f^2 - 1.618569 \times 10^{-6}T_f^3\right)10^{-6}$$

$$Pr = 1.757623 - 9.3943793 \times 10^{-3}T_f + 2.8247901 \times 10^{-5}T_f^2 - 2.8561855 \times 10^{-8}T_f^3$$

$$\rho = 0.9380475 + 1.3550166 \times 10^{-2}T_f - 6.9079673 \times 10^{-5}T_f^2 + 8.8553321 \times 10^{-8}T_f^3$$

$$C_P = \left(1.290128 - 2.8180762 \times 10^{-3}T_f + 9.0782796 \times 10^{-6}T_f^2 - 9.5160644 \times 10^{-9}T_f^3\right)10^3$$

$$k = \left(58.8769 - 0.4907669T_f + 1.9291618 \times 10^{-3}T_f^2 - 2.1899 \times 10^{-6}T_f^3\right)10^{-3}$$

3.1.3. Critical distances on a flux plate

The transition of free convection flow on a vertical uniform flux plate has different characteristics than an isothermal plate. Results in Holman [2002]

show that the transition for a uniform heat surface flux occurs late compared to an isothermal plate. For water, air and oil, the flow becomes fully developed turbulent when $2\times 10^{13} < Ra^{*} < 1\times 10^{14}$, where the modified Rayleigh number is defined as $Ra^{*}=Gr^{*}Pr$ with the modified Grashof number, $Gr^{*} = GrNu$. The critical height in this case can be determined from

$$L_C = (Gr^{*} kv^2/(g\beta q_P))^{1/4} \tag{3. 9}$$

3.2. Numerical methods

3.2.1. Governing equations

The free convection over a heated plate is assumed to be governed by the three dimensional Navier–Stokes equations together with the energy equation. The fluid (air) flow is Newtonian, and all the physical properties are assumed to be constant except the density which will vary and relate to the buoyance terms in the momentum equations. Under the Boussinesq approximation the governing momentum and energy equations take the following forms.

$$\frac{\partial(\rho u_j)}{\partial x_j} = 0 \tag{3. 10}$$

$$\frac{\partial(\rho u)}{\partial t} + \frac{\partial(\rho uu)}{\partial x} + \frac{\partial(\rho uv)}{\partial y} + \frac{\partial(\rho uw)}{\partial z} = -\frac{\partial p}{\partial x} + \frac{\partial}{\partial x}\left(\mu\frac{\partial u}{\partial x}\right) + \frac{\partial}{\partial y}\left(\mu\frac{\partial u}{\partial y}\right) + \frac{\partial}{\partial z}\left(\mu\frac{\partial u}{\partial z}\right) + gsin\theta(\rho-\rho_0) \tag{3. 11}$$

$$\frac{\partial(\rho v)}{\partial t} + \frac{\partial(\rho vu)}{\partial x} + \frac{\partial(\rho vv)}{\partial y} + \frac{\partial(\rho vw)}{\partial z} = -\frac{\partial p}{\partial y} + \frac{\partial}{\partial x}\left(\mu\frac{\partial v}{\partial x}\right) + \frac{\partial}{\partial y}\left(\mu\frac{\partial v}{\partial y}\right) + \frac{\partial}{\partial z}\left(\mu\frac{\partial v}{\partial z}\right) + gcos\theta(\rho-\rho_0) \tag{3. 12}$$

$$\frac{\partial(\rho w)}{\partial t}+\frac{\partial(\rho w u)}{\partial x}+\frac{\partial(\rho w v)}{\partial y}+\frac{\partial(\rho w w)}{\partial z}=-\frac{\partial p}{\partial z}+\frac{\partial}{\partial x}\left(\mu\frac{\partial w}{\partial x}\right)+\frac{\partial}{\partial y}\left(\mu\frac{\partial w}{\partial y}\right)+\frac{\partial}{\partial z}\left(\mu\frac{\partial w}{\partial z}\right) \quad (3.\ 13)$$

$$\frac{\partial(\rho T)}{\partial t}+\frac{\partial\left(\rho u_j T\right)}{\partial x_j}=\frac{\partial}{\partial x_j}\left(\Gamma\frac{\partial T}{\partial x_j}\right) \quad (3.\ 14)$$

where x_j is the coordinate system and u_i is the corresponding velocity components, p is the pressure, g is the gravitational acceleration, ρ is the density, μ is the dynamic viscosity coefficient, T is the temperature, and Γ is the diffusion coefficient in the energy equation defined as μ/Pr where Pr is the Prandtl number.

In natural convection usually a low velocity exists, so the flow at the entrance of a channel is assumed to be laminar. As the flow develops along the channel, the transition will occur followed by the breakdown of boundary and thermal layers to generate turbulence toward the flow downstream. So, the above conservation Equations (3. 10) - (3. 14) are solved directly for the natural convection flow developing in laminar region, while in turbulent region both the Γ and μ are replaced by their effective values, Γ_{eff} and μ_{eff} respectively, as presented in Nicholas and Markatos [1978] and Bacharoudis et al. [2007]. These are defined as

$$\mu_{\text{eff}}=\mu+\mu_t \quad (3.\ 15)$$

$$\Gamma_{\text{eff}}=\frac{\text{k}}{\text{C}_\text{p}}+\frac{\mu_\text{t}}{\sigma_t} \quad (3.\ 16)$$

where μ_t is the turbulent molecular viscosity, σ_t is the turbulent Prandtl number taken as 0.85, k is the thermal conductivity of air, C_p is the air specific heat capacity.

The turbulent viscosity μ_t is also known as the eddy viscosity of the turbulent flow appearing in Equations (3. 15) - (3. 16), which depends on the mean flow rate of the deformation from the Boussinesq theory. A time averaging is carried out to the above governing equations (3. 10) - (3. 14) to obtain a Reynolds averaged Navier-Stokes (RANS) equations which are solved by using *k-ε* models as described later. However, these equations contain unknown Reynolds stresses which are expressed as the deformation of the mean flow quantises, for example, for the momentum equations these can be written as below (for further details see Versteeg and Malalasekera [2007]).

$$\tau_{ij} = -\rho\overline{u_i' u_j'} = \mu_t \left(\frac{\partial u_i}{\partial x_j} + \frac{\partial u_j}{\partial x_i} \right) \tag{3. 17}$$

where, τ is the shear stresses, u' is the velocity fluctuation in the turbulent flow.

As a direct numerical solution of the Navier-Stokes equations exists for only a laminar flow, the turbulent flows are modelled by using several turbulence modelling schemes. In this work, three different *k-ε* models such as standard model, RNG model, and Realizable model are used, which are described below briefly.

In terms of LES application, the turbulent viscosity μ_t will be replaced by dynamic eddy viscosity μ_{sgs} while the diffusion coefficient in the turbulent flow $\Gamma_t = (\mu_t/\sigma_t)$ will replaced by Γ_{sgs} . Further details about the LES modelling are reported in § 3.2.6.

3.2.2. Standard *k-ε* model

The standard *k-ε* model was initially proposed by Launder and Spalding [1972], which is based on the two terms, dissipation rate (ε) and turbulent kinetic energy (k). The model transport equation for ε is obtained by employing physical reasoning while the turbulent kinetic energy (k) is derived from an exact equation by assuming that the effect of molecular viscosity of the flow is negligible and the flow is fully developed. Since the launch of the standard model, it has become widely popular and applied to many industrial flow and heat transfer simulations.

Transport equations of standard model

The distributions of kinetic energy (k) and rate of dissipation (ε) can be determined from the following governing equations:

Turbulent kinetic energy: *k*- equation

$$\frac{\partial}{\partial t}(\rho k) + \frac{\partial}{\partial x_j}(\rho k u_j) = \frac{\partial}{\partial x_i}\left[\left(\mu + \frac{\mu_t}{\sigma_k}\right)\frac{\partial k}{\partial x_i}\right] + G_k + G_b - \rho\varepsilon \tag{3. 18}$$

Turbulent dissipation energy: ε- equation

$$\frac{\partial}{\partial t}(\rho\varepsilon) + \frac{\partial}{\partial x_j}(\rho\varepsilon u_j) = \frac{\partial}{\partial x_i}\left[\left(\mu + \frac{\mu_t}{\sigma_\varepsilon}\right)\frac{\partial \varepsilon}{\partial x_i}\right] - C_{2\varepsilon}\rho\frac{\varepsilon^2}{k} + G_{1\varepsilon}\frac{\varepsilon}{k}(G_k + G_{3\varepsilon}G_b) \tag{3. 19}$$

where σ_k is the Prandtl number for k, σ_ε is the Prandtl number for ε, and $C_{1\varepsilon}$, $C_{2\varepsilon}$ and $C_{3\varepsilon}$ are the constant models.

The two terms in the left hand side of Equations (3. 18) - (3. 19) represent respectively the transport of kinetic energy of fluctuation and dissipation of the rate of kinetic energy by convection, while the first two terms in the right hand side are their diffusion. G_k reflects the rate of the turbulent kinetic energy, which is defined by the gradients of the mean velocity of the flow as

$$G_k = \mu_t \left(\frac{\partial u_i}{\partial x_j} + \frac{\partial u_j}{\partial x_i} \right) \frac{\partial u_i}{\partial x_j} - \frac{2}{3} \rho k \delta_{i,j} \frac{\partial u_i}{\partial x_j} \quad (3.\ 20)$$

where G_b is the generation of the turbulent kinetic energy, which is defined by

$$G_b = g_i \beta \frac{\mu_t}{\sigma_t} \frac{\partial T}{\partial x_j} \quad (3.\ 21)$$

and g_i *is* the gravitational vector acting in the direction *j,* β is the thermal expansion coefficient of air, which can be defined as $\beta = -\frac{1}{\rho}\left(\frac{\partial \rho}{\partial T}\right)_{p_{constant}}$.

Turbulent viscosity

The turbulent viscosity μ_t of turbulent flow is computed by combining ε and k as described below

$$\mu_t = \rho C_\mu \frac{k^2}{\varepsilon} \quad (3.\ 22)$$

The standard k-ε model has four adjustable constants, $C_{1\varepsilon}$, $C_{2\varepsilon}$, $C_{3\varepsilon}$ and C_μ, and two Prandtl numbers σ_k and σ_ε. The standard values reported below are taken from the experimental data of air flow in full turbulent region in Launder and Spalding [1972], $C_{1\varepsilon} = 1.44$, $C_{2\varepsilon} = 1.92$, $C_{3\varepsilon} = 1.0$, $C_\mu = 0.09$, $\sigma_k = 1.0$ and $\sigma_\varepsilon = 1.3$.

3.2.3. RNG *k-ε* model

The renormalization group (RNG) was derived by Yakhot et al.[1992] with an extensive analysis of the eddy viscosity model. Compared with the standard *k-ε* model, the RNG model carries an additional factor in the turbulent dissipation energy (ε) equation, which leads to improving the accuracy of strain in the flow field. In addition, while the standard model was derived at a high Reynolds number flow, the RNG *k-ε* model is appropriate for a low Reynolds number flow as well.

Transport equations of the RNG *k-ε* model

The RNG *k-ε* model has a similar form of the kinetic energy *k* and dissipation energy ε equations as in the standard model

Turbulent kinetic energy: *k*- equation

$$\frac{\partial}{\partial t}(\rho k) + \frac{\partial}{\partial x_j}(\rho k u_j) = \frac{\partial}{\partial x_i}\left[\alpha_k \mu_{eff} \frac{\partial k}{\partial x_i}\right] + G_k + G_b - \rho\varepsilon \tag{3. 23}$$

Turbulent dissipation energy: ε- equation

$$\frac{\partial}{\partial t}(\rho\varepsilon) + \frac{\partial}{\partial x_j}(\rho\varepsilon u_j) = \frac{\partial}{\partial x_i}\left[\alpha_\varepsilon \mu_{eff} \frac{\partial \varepsilon}{\partial x_i}\right] + C_{1\varepsilon}\frac{\varepsilon}{k}(G_k + C_{3\varepsilon}C_b) - C_{2\varepsilon}\rho\frac{\varepsilon^2}{k} - R_\varepsilon \tag{3. 24}$$

where $\alpha_k = \alpha_\varepsilon \approx 1.393$ are the inverse effective Prandtl numbers, which have been determined by the RNG theory. The main deference between the standard and the RNG models is that the additional term R_ε which is related to the mean strain and turbulence quantities and defined as

$$R_\varepsilon = \frac{C_\mu \rho\eta^3(1-\eta/\eta_0)}{1+\beta\eta^3}\frac{\varepsilon^2}{k} \quad (3.\ 25)$$

where η_0 and β are constant taken as 0.012 and 4.38 respectively, and $\eta = Sk/\varepsilon$, where S is the definition of modulus of the mean strain tensor $= \sqrt{(2S_{ij}S_{ij})}$. The value of S_{ij} is then defined as $S_{ij} = \frac{1}{2}\left(\frac{\partial u_j}{\partial x_i} + \frac{\partial u_i}{\partial x_j}\right)$

Substituting the expression of R_ε in Equation (3. 25) to Equation (3. 24)

the turbulent dissipation energy equation becomes

$$\frac{\partial}{\partial t}(\rho\varepsilon) + \frac{\partial}{\partial x_j}(\rho\varepsilon u_j) = \frac{\partial}{\partial x_i}\left[\alpha_\varepsilon \mu_{eff}\frac{\partial \varepsilon}{\partial x_i}\right] + C_{1\varepsilon}\frac{\varepsilon}{k}(G_k + C_{3\varepsilon}G_b) - C_{2\varepsilon}^*\rho\frac{\varepsilon^2}{k} \quad (3.\ 26)$$

where $C_{2\varepsilon}^* = C_{2\varepsilon} + \frac{C_\mu\eta^3(1-\eta/\eta_0)}{1+\beta\eta^3}$, and the two model constants, $C_{1\varepsilon}$ and $C_{2\varepsilon}$ have been derived from the solution of the RNG theory, which are $C_{1\varepsilon}$ = 1.42 and $C_{2\varepsilon}$ = 1.68. In addition, the constant $C_{3\varepsilon}$ = 1.0.

Effective viscosity model

Different equations have been provided in the RNG theory for determining the turbulent viscosity. The equation below takes a simplistic form:

$$d\left(\frac{\rho^2 k}{\sqrt{\varepsilon\mu}}\right) = 1.72\frac{\hat{\nu}}{\sqrt{\hat{\nu}^3 - 1 + C_\nu}}d\hat{\nu} \quad (3.\ 27)$$

where $\hat{\nu} = \mu_{eff}/\mu$ and $C_\nu \approx 100$. Equation (3. 27) allows the RNG model to provide better results near the wall flow at a low Reynolds number. While at a

high Reynolds number, the turbulent viscosity μ_t is determined from Equation (3. 22) with $C_\mu = 0.0845$.

3.2.4. Realizable *k-ε* model

The Realizable *k-ε* model was proposed by Shih et al. [1995], which was derived based on dynamic equations of mean square fluctuation at a large range of flow Reynolds number. The model has its ability to control the Reynolds stresses, so the Realizable *k-ε* model may be useful to predict the development of boundary layer near the wall better than the other models. The transport equations are listed below:

Turbulent kinetic energy: *k* - equation

$$\frac{\partial}{\partial t}(\rho k) + \frac{\partial}{\partial x_j}(\rho k u_j) = \frac{\partial}{\partial x_j}\left[\left(\mu + \frac{\mu_t}{\sigma_k}\right)\frac{\partial k}{\partial x_j}\right] + G_k + G_b - \rho\varepsilon \tag{3. 28}$$

Turbulent dissipation energy: ε - equation

$$\frac{\partial}{\partial t}(\rho\varepsilon) + \frac{\partial(\rho\varepsilon u_j)}{\partial x_j} = \frac{\partial}{\partial x_j}\left[\left(\mu + \frac{\mu_t}{\sigma_\varepsilon}\right)\frac{\partial \varepsilon}{\partial x_j}\right] + \rho C_1 S_\varepsilon - \rho C_2 \frac{\varepsilon^2}{\varepsilon + \sqrt{\nu\varepsilon}}$$

$$+ G_{1\varepsilon}\frac{\varepsilon}{k} C_{3\varepsilon} G_b \tag{3. 29}$$

where $C_1 = \max\left[0.43, \frac{\eta}{\eta+5}\right]$ and $\eta = S\frac{k}{\varepsilon}$, both the parameters S and η are defined in Equation (3. 25)

Modelling the turbulent viscosity

The equation to calculate the eddy viscosity in the Realizable model is similar to the standard and RNG models and defined as $\mu_t = \rho C_\mu \frac{k^2}{\varepsilon}$, where the C_μ is a constant. However in the Realizable model a new formula is used to calculate C_μ as presented in Reynolds [1987] and Shih et al. [1995].

$$C_\mu = 1/A_0 + A_S \frac{kU^*}{\varepsilon} \quad (3.30)$$

where A_0 and A_S are the model constants given as $A_0 = 4.04$, $A_s = \sqrt{(6\cos\phi)}$ where $\phi = \frac{1}{3}\cos^{-1}\sqrt{(6W)}$. The details on the formulation of U^* can be found in Shih et al. [1995].

The turbulent viscosity formula as reported becomes a function of many factors of the characteristics of turbulent field such as k and ε, the mean rate of the rotation, and the angular velocity of the flow. As a result, the Realizable k-ε model has been extensively validated for high range of Reynolds number flows. The model constants in the model are $C_{1\varepsilon} = 1.44$, $C_2 = 1.9$, $C_{3\varepsilon} = 1.0$, $\sigma_k = 1.0$ and $\sigma_\varepsilon = 1.2$.

3.2.5. Standard wall function

This model was proposed by Launder and Spalding [1972], where the effect of the viscosity of the flow in a laminar sub-layer and buffer region was neglected.

Modelling mean velocity

The mean velocity can be calculated by the logarithmic low

$$V^* = \frac{1}{k}\ln(Ex^*) \tag{3. 31}$$

where $V^* \equiv \frac{V_P C_\mu^{1/4} k_P^{1/2}}{\tau_\omega/\rho}$, $x^* \equiv \frac{x_P C_\mu^{1/4} k_P^{1/2} \rho}{\mu}$, k is the von karman constant = 0.4187, E is the empirical constant = 9.793 ,V_P is the mean velocity of the flow at point P, k_P is the local turbulent kinetic energy and x_P is the normal distance between the point P and the surface.

In the laminar stress region, the mean velocity has a linear relationship with the vertical distance from the surface of wall as $V^* = x^*$.

Modelling mean temperature

Two different models are employed to calculate the temperature near the solid wall: first model is the linear law which is used in the thermal conduction sub layer and the second model is the logarithmic law which is for turbulent region. The mean temperature can be defined as

$$T^* \equiv \frac{(T_w - T_P)\rho C_p C_\mu^{1/4} k_P^{1/2}}{\dot{q}}$$

$$= \begin{cases} Prx^* + \frac{1}{2}\rho Pr \frac{C_\mu^{1/4} k_P^{1/2}}{\dot{q}} U_P^2 & x^* < x_T^* \\ \sigma t \left[\frac{1}{k} ln(Ex^*) + \dot{P}\right] + \frac{1}{2}\rho Pr \frac{C_\mu^{1/4} k_P^{1/2}}{\dot{q}} U_P^2 & \\ \quad + \frac{1}{2}\rho \frac{C_\mu^{1/4} k_P^{1/2}}{q_c}[\sigma t\, V_P^2 + (Pr - \sigma t\,)V_c^2] & x^* > x_T^* \end{cases} \tag{3. 32}$$

where $\dot{P}$ is a non-dimensional function of the turbulent Prandtl number and expressed as

$$\dot{P} = 9.24\left[\left(\frac{Pr}{\sigma t}\right)^{3/4} - 1\right]\left[1 + 0.28e^{-0.007Pr/\sigma t}\right] \quad (3.\ 33)$$

where

x_T^* is the thermal sub layer thickness which is determined from both the logarithmic and linear models, V_c is the mean velocity at $x^* = x_T^*$, ρ is density of the flow, σ_t is turbulent Prandtl number.

3.2.6. Enhanced wall function

To analyse the boundary layer near the wall, the following functions Kader [1981] were employed, where the model is extended to present the effect of the viscosity in the inner region.

Modelling mean velocity

The velocity was presented in two compounds, linear in the laminar flow and logarithmic in the turbulent flow,

$$v^+ = e^{\Gamma_v} v_{lam}^+ + e^{\frac{1}{\Gamma_v}} v_{turb}^+ \quad (3.\ 34)$$

where the factor $\Gamma_v$can be written as,

$$\Gamma_v = -\frac{a(x^+)^4}{1+bx^+} \quad (3.\ 35)$$

where a = 0.01 and b = 5.

The general derivative equation for the velocity, $\frac{dv^+}{dx^+}$ is

$$\frac{dv^+}{dx^+} = e^{\Gamma_v}\frac{dv^+_{lam}}{dx^+} + e^{\frac{1}{\Gamma}}\frac{dv^+_{turb}}{dx^+} \quad (3.\ 36)$$

The distribution of the velocities and temperatures are expressed as

$$\frac{dv^+_{lam}}{d^+_x} = 1 + \alpha x^+, \quad (3.\ 37)$$

$$\frac{dv^+_{turb}}{d^+_x} = \frac{1}{kx^+}[S'(1 - \beta \mathrm{v}^+ - \gamma(\mathrm{v}^+)^2 2)\,]^{1/2}, \quad (3.\ 38)$$

where S' is a factor, which depends on the local flux, shear stress and pressure gradients of the flow. The factor v^+ can also be defined as a function in the velocity as $v^+ = v / \sqrt{(\tau/\rho)}$.

Modelling mean temperature

The temperature is calculated from

$$T^+ = \frac{(T_w - T_P)\rho c_p v^*}{\dot{q}} = e^{\Gamma_t}T^+_{lam} + e^{\frac{1}{\Gamma_t}}T^+_{turb} \quad (3.\ 39)$$

where the blending factor can be presented as

$$\Gamma_t = -\frac{a(Prx^+)^4}{1 + bPr^3x^+} \quad (3.\ 40)$$

Both the coefficients *a* and *b* are already defined in Equation (3. 35). The distributions of the temperature in laminar and turbulent flow are respectively,

$$T^+_{lam} = Pr\left(v^+_{lam} + \frac{\rho v^*}{2\dot{q}}v^2\right), \quad (3.\ 41)$$

$$T^+_{turb} = \sigma t\,\left(v^+_{turb} + P + \frac{\rho v^*}{2\dot{q}}\left[v^2 - \left(\frac{Pr}{\sigma t} - 1\right)(v^+_c)^2(v^*)^2\right]\right), \quad (3.\ 42)$$

where v_c^+ is the value of v^+ at the crossover between the laminar and turbulent region.

3.2.7. Numerical techniques in *k*-ε models

Finite volume method is used to discretise the governing equations with a second order upwind scheme to solve the discretised equations, where the unknown quantities at the grid-cell faces are computed by using a multidimensional linear reconstruction approach described in Barth and Jespersen [1989] to achieve higher order at the cell faces through a Taylor series expansion of the cell centered solution about the cell centroid. More detail on the methodology to discretise the governing transport equations is reported in the documentation of FLUENT and will not be repeated here.

Additionally, the SIMPLE algorithm of Patankar [1980] is employed to solve the pressure based equation derived from the momentum and continuity equations such that the velocity and pressure fields are coupled to each other and solved by adopting an iterative solution strategy. In this algorithm, the discretised momentum equations are initially solved by using an assumed pressure field (p^*) to yield the velocity solutions (u^*, v^*).

A correction to the pressure (p'), which is the difference between the actual and assumed pressures, is then applied to achieve a better approximation of the pressure field using $p = p' + p^*$. Similarly, the velocity components are corrected to get u, v; and then the discretised equations of a scalar quantity e. g. the energy (T), turbulent energy (k) and its dissipation rate (ε) are solved using the most updated results of u, v, and p. All these equations are solved sequentially and iteratively using Fluent 6.3; and the final numerical solutions are achieved when the residuals of the continuity and velocity components

become less than 10^{-6}. The residual of the energy, turbulent kinetic energy and its dissipation however is reduced further to 10^{-8} to avoid any sensitivity to the solutions of the turbulent fluctuating components.

3.2.8. Large eddy simulation

To obtain the LES equations, the governing equations (3. 10) - (3. 14) are filtered first using a spatial filter which separates the large scale (resolved scale) flow field from the small scale (sub-grid scale). If, for example, $f(x_j, t)$ is considered to be a generic instantaneous variable at a location x_j, the corresponding filtered variable, also known as the resolvable component of $f(x_j,\ t)$ and denoted by $\bar{f}\ (x_j,\ t)$, is defined as the convolution of $f(x_j,\ t)$, with a filter function *G* (Leonard [1974]) as

$$\bar{f}\ (x_j, t) = \int_D f(x'_j, t) G\left(x_j - x'_j, \Delta(x_j)\right) dx'_j, \tag{3. 43}$$

where *D* is the entire domain; $\Delta(x_j)$ is the filter width which in LES practice is generally related to the mesh size, e.g. $\Delta(x_j) = \sqrt[3]{\Delta x \Delta y \Delta z}$ .The filter function *G* is usually defined as the product of three one-dimensional filters,

$$G\left(x_j - x'_j, \Delta(x_j)\right) = \prod_{j=1}^{3} g\left(x_j - x'_j, \Delta(x_j)\right), \tag{3. 44}$$

which must satisfy the normalisation condition,

$$\int_D G\left(x_j - x'_j, \Delta(x_j)\right) dx'_j = 1. \tag{3. 45}$$

Defining the Fourier transform $\hat{f}\ (k_j, t)$ of $f(x_j, t)$ as

$$\hat{f}\ (k_j, t) = \iiint_{-\infty}^{\infty} f(x'_j, t) e^{-ik_j x_j}\ dx'_j, \tag{3. 46}$$

the spatial filter $\bar{f}\left(x_j, t\right)$ defined in (3. 43), can now be written in the Fourier space as

$$\hat{\bar{f}}\left(x_j, t\right) = \hat{G}\ \hat{f}\left(k_j, t\right), \tag{3. 47}$$

where $\hat{G} = \prod_{j=1}^{3} \hat{g}\left(k_j,\ \Delta\left(x_j\right)\right)$ is now the Fourier transform of the filter function. It is important to note that this filter function determines the size and structure of the smallest resolvable eddies. Various distributions for the filter function are available in the literature; for example, see Leonard [1974], Germano et al. [1991] and Ghosal and Moin [1995]. But the most commonly used filter functions and their Fourier transforms are given below.

The "top hat" filter:

$$G\left(x_j - x'_j, \Delta\left(x_j\right)\right) = \begin{cases} \frac{1}{\Delta\left(x_j\right)} & \text{if} \quad \left|x_j - x'_j\right| \leq \frac{\Delta\left(x_j\right)}{2} \\ 0 & \text{otherwise} \end{cases} \tag{3. 48}$$

and the Fourier transform of the top hat filter is

$$\hat{g}\left(k_j, x_j\right) = \sin\left(k_j \frac{\Delta\left(x_j\right)}{2}\right) / k_j \frac{\Delta\left(x_j\right)}{2}. \tag{3. 49}$$

The Gaussian filter,

$$G\left(x_j - x'_j, \Delta\left(x_j\right)\right) = \left(\sqrt{\frac{6}{\pi}} \frac{1}{\Delta\left(x_j\right)^2}\right) \exp\left[-\frac{6\left(x_j - x'_j\right)^2}{\Delta\left(x_j\right)}\right], \tag{3. 50}$$

and its Fourier transform is

$$\hat{g}\left(k_j, \Delta\left(x_j\right)\right) = \exp\left(-\frac{k_j \Delta\left(x_j\right)}{24}\right), \tag{3. 51}$$

The Fourier cut-off filter,

$$G\left[x_j - x'_j, \Delta(x_j)\right] = \frac{sin\ \left(k_c\left(x_j - x'_j\right)\right)}{\pi\left(x_j - x'_j\right)} \tag{3. 52}$$

where $k_c = \frac{\pi}{\Delta(x_j)}$, and the corresponding Fourier transform is

$$\hat{g}\left(k_j, \quad \Delta(x_j)\right) = \begin{cases} 1 & \text{if} \quad |k| \leq k_c \\ 0 & \text{otherwise} \end{cases} \tag{3. 53}$$

So, in the Fourier cut-off filter if $\hat{g}$ is zero for $k^2 = k_j k_i > k_c^2$, where k_c is a cut-off wave number defining the limit of wave resolution, $\bar{f}$ will contain no contribution from the wave numbers greater than k_c, that is, the wave numbers greater than a cut-off value are completely removed from the flow field leaving the smallest wave numbers unaffected. In contrast, both the top hat and Gaussian filter functions affect all the wave numbers without removing completely any particular part of the spectrum. In this simulation I have used the "top hat" filter given in Equation (3. 48) and suggested by Germano et al. [1991], as it naturally fits into a finite volume formulation (see di Mare and Jones [2003], Paul and Molla [2012]).

Filtered governing equations

By applying the above filter function (3. 48) to the Navier-Stokes and energy Equations (3. 10)- (3. 14), we obtain the following filtered equations:

$$\frac{\partial\left(\rho\bar{u}_j\right)}{\partial x_j} = 0 \tag{3. 54}$$

$$\frac{\partial(\rho\bar{u})}{\partial t}+\frac{\partial(\rho\bar{u}\bar{u})}{\partial x}+\frac{\partial(\rho\bar{u}\bar{v})}{\partial y}+\frac{\partial(\rho\bar{u}\bar{w})}{\partial z}=-\frac{\partial\bar{p}}{\partial x}+\frac{\partial}{\partial x}\left(\mu\frac{\partial\bar{u}}{\partial x}\right)+\frac{\partial}{\partial y}\left(\mu\frac{\partial\bar{u}}{\partial y}\right)+\frac{\partial}{\partial z}\left(\mu\frac{\partial\bar{u}}{\partial z}\right)-\frac{\partial\tau_{ij}}{\partial x}+gsin\theta(\rho-\rho_0) \quad (3.\ 55)$$

$$\frac{\partial(\rho\bar{v})}{\partial t}+\frac{\partial(\rho\bar{v}\bar{u})}{\partial x}+\frac{\partial(\rho\bar{v}\bar{v})}{\partial y}+\frac{\partial(\rho\bar{v}\bar{w})}{\partial z}=-\frac{\partial\bar{p}}{\partial y}+\frac{\partial}{\partial x}\left(\mu\frac{\partial\bar{v}}{\partial x}\right)+\frac{\partial}{\partial y}\left(\mu\frac{\partial\bar{v}}{\partial y}\right)+\frac{\partial}{\partial z}\left(\mu\frac{\partial\bar{v}}{\partial z}\right)-\frac{\partial\tau_{ij}}{\partial y}+gcos\theta(\rho-\rho_0) \quad (3.\ 56)$$

$$\frac{\partial(\rho\bar{w})}{\partial t}+\frac{\partial(\rho\bar{w}\bar{u})}{\partial x}+\frac{\partial(\rho\bar{w}\bar{v})}{\partial y}+\frac{\partial(\rho\bar{w}\bar{w})}{\partial z}=-\frac{\partial\bar{p}}{\partial z}+\frac{\partial}{\partial x}\left(\mu\frac{\partial\bar{w}}{\partial x}\right)+\frac{\partial}{\partial y}\left(\mu\frac{\partial\bar{w}}{\partial y}\right)+\frac{\partial}{\partial z}\left(\mu\frac{\partial\bar{w}}{\partial z}\right)-\frac{\partial\tau_{ij}}{\partial z} \quad (3.\ 57)$$

$$\frac{\partial(\rho\bar{T})}{\partial t}+\frac{\partial\left(\rho\bar{u}_j\bar{T}\right)}{\partial x_j}=\frac{\partial}{\partial x_j}\left(\Gamma\frac{\partial\bar{T}}{\partial x_j}\right)-\frac{\partial\left(\tau_j^{sgs}\right)}{\partial x_j} \quad (3.\ 58)$$

where the effects of the small scales, appearing in the subgrid-scale stress terms, are defined as

$$\tau_{ij}=\rho\overline{u_\iota u_j}-\rho\bar{u}_\iota\bar{u}_j \quad (3.\ 59)$$

and

$$J_j^{sgs}=\rho\overline{u_jT}-\rho\bar{u}_j\bar{T} \quad (3.\ 60)$$

which are unknown and referred to the sub-grid scale stresses and the sub-grid scale scalar fluxes respectively. These unknowns must be modelled and explained in the section below.

Subgrid-scale modelling

The Smagorinsky model [1963], used to model the sub-grid scale stresses, is based on the eddy viscosity assumption of the form,

$$\tau_{ij} - \frac{1}{3}\delta_{ij}\tau_{kk} = -2\mu_{sgs}\,\bar{S}_{ij} \tag{3. 61}$$

where the sub-grid dynamic eddy viscosity, μ_{sgs}, is obtained by assuming that the turbulent dissipation is in equilibrium with the turbulent energy production which yields an expression of

$$\mu_{sgs} = \rho(C_s\Delta)^2|\bar{S}|, \tag{3. 62}$$

where C_S is the Smagorinsky model constant and $|\bar{S}| = \sqrt{2\,\bar{s}_{ij}\bar{s}_{ij}}$ is the magnitude of the resolved scale strain rate tensor $\bar{s}_{ij}$ defined as

$$\bar{S}_{ij} = \frac{1}{2}\left(\frac{\partial\bar{u}_i}{\partial x_j} + \frac{\partial\bar{u}_j}{\partial x_i}\right) \tag{3. 63}$$

Thus, the Smagorinsky model takes the form of

$$\tau_{ij} - \frac{1}{3}\delta_{ij}\tau_{kk} = -2\rho(C_s\,\Delta)^2|\bar{S}|\bar{S}_{ij.} \tag{3. 64}$$

The unknown Smagorinsky constant, C_s, is calculated using the *localized* dynamic model of Piomelli and Liu [1995]. For the sub-grid scale scalar fluxes a gradient model, Schmidt and Schumann [1989], is applied:

$$J_j^{sgs} = -\rho\,\Gamma_{sgs}\frac{\partial\bar{T}}{\partial x_j} = -\rho\,\frac{\mu_{sgs}}{\sigma_{sgs}}\frac{\partial\bar{T}}{\partial x_j} \tag{3. 65}$$

where σ_{sgs} is the sub-grid scale Prandtl/Schmidt number which is here assigned a value of 0.70.

3.2.9. Numerical procedures in LES

An overview of the computational procedure employed in the LES is presented in this section. An in-house FORTRAN code, LES-BOFFIN (Boundary Fitted Flow Integrator), which was initially developed at the Imperial College London for simulating turbulent combustion reacting flow, has been modified and extended in the thesis in order to solve the incompressible governing equations for free convection.

The code is fully implicit and second order accurate in both space and time. The BOFFIN code has previously been applied to simulate turbulent flow in other engineering contexts, for examples, see LES of a gas turbine combustor by di Mare and Jones [2003], Paul et al. [2006], Paul [2008] and Jones and Paul [2006], turbulent flow past a swept fence by di Mare and Jones [2003], pulsatile blood flow in an arterial stenosis by Paul and Molla [2012], and turbulent cross flows of jets by Wille [1997].

The filtered governing equations (3. 54) - (3. 58) in the Cartesian coordinates are transformed into a curvilinear coordinate system according to Thomson *et al.* [1974], and the finite volume approach is used to discretise the partial differential equations to yield a system of quasi-linear algebraic equations. To discretise the spatial derivatives in equations, the standard second order accurate central difference scheme is used, except for the convective terms in the momentum equations for which an energy conserving discretisation scheme is used (Morinishi [1995]).

Total Variation Diminishing (TVD) scheme, e.g. see Sweby [1984], has also been used for the convective terms in the energy equation to avoid any overshooting / undershooting in the boundary conditions of the scalar field such as the flow temperature. While for the Poisson like pressure correction

equation an ICCG (Kershaw [1978]) solver is applied due to its symmetric and positive definite nature. More details about the numerical algorithm are given in the cited references above as well as in the reference papers therein.

Chapter 4

Physical characteristics of natural convection flow on a vertical heated plate

4.1. Introduction

Boundary layers in natural convection flow have been analysed extensively for a number of decades. Consequently, many experimental and numerical investigations have been carried out to study the behaviour of the development of boundary layer flow on various geometries as pointed out in § 2.1 of Chapter 2. Surprisingly, to the authors' best of knowledge, majority of the experimental and numerical works, reported above in the context of free-convection on a heated plate, presented only the results of the physical properties of the boundary layer as a dimensional quantity in local velocity and temperature. However, these quantities should be known at different locations and different thermal conditions for the flow to predict the thickness of the boundary layer. In this Chapter, the critical distance and the thickness of boundary layer are investigated at various positions along the wall for different flow temperatures. In addition, numerical simulations are performed to investigate the distributions of velocity and kinetic energy and its production along the heated plate where The Realizable k-ε model was employed in this

simulation. Finally, both the analytical and numerical results are compared with experimental data available in literature.

The layout of this chapter is as follows: a description of the model geometry and boundary conditions is given in § 4.2, while numerical method is presented in § 4.3. Results with discussion and comparisons of present results with experimental data are given in § 4.4 and § 4.5, respectively, and finally a general conclusion of this chapter is drawn in § 4.6.

4.2. Geometry and boundary conditions

The computational domain for the numerical simulation was chosen as 4 m × 1 m (vertical and horizontal distances respectively). A schematic drawing of the flow geometry with the co-ordinate systems is shown in Figure 4. 1. The simulations were focused on the effects of the transition of the flow developing on the heated plate under various temperatures of the plate and the ambient air, as reported in the experimental work of Tsuji and Nagano [1988a].

The flow in the leading edge of the plate was assumed to be developed from the laminar stage, therefore, the turbulent kinetic energy, k, and turbulent dissipation energy, ε, were set to zero at the inlet boundary. In addition, the outlet and the right-hand side boundary facing the plate were left free to the atmosphere keeping zero gauge pressure.

4.3. Results and discussions

Results of the analytical investigation of both laminar and turbulent flow of air under the isothermal and heat flux condition of the heated plate are reported in the first section, followed by the numerical results which particularly focus on

the distributions of the velocity, temperature and kinetic energy of the air flow on the isothermal heated plate including the characteristic and transition natures of the boundary layer flow. Comparisons between the present results with some experimental data are given here.

4.3.1. Analytical results on isothermal plate

Laminar flow case

Figure 4. 2 and Figure 4. 3 show the Grashof number and the thickness of the boundary layer respectively. Note that Equation (3. 1) was used to determine the thickness of the boundary layer flow in this case. In general, the results in Figure 4. 2 and Figure 4. 3 show that an increase in the temperature of the plate causes an early transition of the flow from the laminar to turbulent stage. For instance, at T_P = 40°C the flow becomes turbulent at a plate distance of about 0.77 m. While for the case of T_P = 90°C it is occurring approximately at a vertical distance of 0.60 m. By employing Equation (3. 2) the influences of both T_P and T_a on the critical distance of the plate along with the thickness of the boundary layer at the critical distance are presented in Figure 4. 4 and Figure 4. 5. Note that the thickness of the boundary layer at the critical distance is calculated by using Equation (3.1) when $Gr \approx 10^9$. The results show that, when T_P = 30°C and T_a = 27°C, the critical distance is located approximately at 1.578 m and the corresponding thickness of the boundary layer at this location is calculated to be 0.042 m. However, fixing the plate temperature at T_P = 30°C and reducing the air temperature to T_a = 15°C, both the critical distance and the thickness of the boundary layer drop to 0.88 m and 0.0235 m respectively. Furthermore, if we fix the air temperature at T_a = 24°C and increase T_P from 35°C to 60°C, i.e. increasing T_P by 70%, the results show that

both the critical distance and the thickness drop by approximately 30% and 36% respectively.

Turbulent flow case

The results in Figure 4. 6 shows that the thickness of the boundary layer, determined by using Equation (3. 6), increases sharply in the turbulent flow regime compared to that found in the laminar flow regime due to the effect of the buoyance force on the growth of the boundary layer. Effects of the roles of the turbulent flow quantities on this will be assessed latter in Section 4.4.3 in this Chapter with the aid of the detailed numerical results. However, it is important to note that the ambient temperature of air shows significant effects on the thickness and in fact has a large influence in the turbulent flow regime. For instance, at Ta = 21°C and L= 2.8 m the thickness of the boundary layer becomes approximately 0.22 m, while with an increase in the air temperature to 24°C, the thickness drops by 26%.

4.3.2. Analytical results on the heat flux surface

Figure 4. 7 summarises the effects of the variation in the heat flux on the critical height of the vertical plate for the various air temperature of 9°C, 19°C and 29°C. The most important point to note in this figure is that the temperature variation of the flow has a little effect on the transition stage. The critical distance is mainly affected by the heat flux of the plate, for example, at q_p = 220 W/m^2 with dropping the air temperature (i.e. from 29°C to 9°C) the critical height declines by 3.8% (i.e. from 1.84 m to 1.77m). However, at Ta = 19°C with declining the heat flux by 74% (from 553 W/m^2 to 145 W/m^2), the critical height increases by 18% (1.625-1.93 m). This phenomenon is understood by the fact that the critical distance on the uniform heat-flux plate

depends on both the heat flux and thermal properties of the air, as shown in Equation (3. 8). The change in the air temperature within the range from 9°C to 29°C seems to have less impact on the thermal properties of the air, Equation (3. 7) . So, the critical distance is affected more by the heat flux of the plate.

4.3.3. Numerical results

Important selected numerical results for both the laminar and turbulent flow stages are presented. Initially, comparisons of the simulated results of the laminar flow against the experimental results of Tsuji and Nagano [1988a] will be provided, which will then be followed by the assessment of the turbulent flow quantities against the relevant experiment data along with their roles into the process of flow transitions occurring on the heated vertical plate. In the laminar flow, the mean velocity and temperature presented in Figure 4. 8 show very good agreement with the experimental results of Tsuji and Nagano [1988a]. The Grashof number at this stage is taken as 1.95×10^{8} as was in the experiment work, but the velocity and the flow temperature results are non-dimensionalised by using $dv= (vy/v_{\infty}) Gr^{-1/2}$ and $dT = (T-T_a)/(T_P-T_a)$ respectively.

Comparison between the numerical results and experimental data of Tsuji and Nagano [1988a] for the velocity in the turbulent flow is given in Figure 4. 9 (a) for Grashof number 8.44×10^{10}. The result indicates that there are some agreements between the numerical and experimental results especially in the inner layer region as well as at the location where the flow velocity becomes maximum, but, in the out layer regime, specifically within $1 \leq (x/y)\, Nu \leq 10$, the velocity results are over-predicted compared to the experiment, which is possibly due to the fact that the growth rate of the ambient air temperature

beside the hot plate in the experimental work was slightly greater than that of the numerical results.

The distribution of the temperature in the turbulent flow can also be seen in Figure 4. 9 (b) where the comparison between the present result and the experimental data of Yan and Nilsson [2005], which was measured at $Gr = 4.3\times10^{10}$, is shown; and clearly the predicted results are very close to the measurements. The sensitivity of Realizable model to present some especial turbulent characterise has been reported in this section, the distribution of the turbulent kinematic viscosity ν_t and the turbulent kinetic energy k were plotted, and comparison have been done with some numerical results, which reported by Henkes and Hoogendoorn [1989], the kinematic viscosity ν_t presented as function in molecular kinematic viscosity ν, while the kinetic energy k was reported as function in velocity scale $v_0 = (g\beta(T_P-T_\infty)\nu)^{1/3}$, the results were plotted in Figure 4. 10 for $Gr = 1.10^{11}$. The figures indicate that, the kinetic energy reached its maximum value close to the outer region, where the kinematic viscosity reached its maximum. However, their value at the inner region is very small, where the flow more effected by the viscosity of the flow.

Temperature profiles across the boundary layer are presented in Figure 4. 11 at six different elevations to assess the development of thermal boundary layers along the heated plate. Air temperature (T_a) is also varied from 15°C to 28°C and the effect it has on the flow temperature as well as on the growth of the thermal boundary layer is examined. The temperature profiles show a systematic rise as y is increased, irrespective to the variation in the air temperature. Close to the heated plate the temperature gradient is considerably large and the development of the thermal boundary layer can easily be traced from the profiles. For example, near the inlet section at $y = 0.1$ m the thickness of the boundary layer is very small (<0.025m). But, as the vertical distance (y)

in the flow direction is increased, the thickness of the thermal boundary layer as well as the temperature in the core region is increased.

Finally, in this section, the transition behaviour of the boundary flow developing on the isothermal heated plate is further assessed by thorough investigation of the key results of the turbulent quantities of the flow. In this regard, the numerical results of the maximum values of the flow velocity, turbulent kinetic energy and its production are depicted in Figure 4. 12. Note that the maximum quantities are determined in the flow field, using $f_{\max}(y) = \underset{x\min \le x \le x\max}{Max} f(x,y)$ where f is a generic function, and then plotted along the vertical axis *y*.

Generally, it could be revealed from the results in Figure 4. 12 that the change in the ambient air temperature has a great impact on the development of the boundary layer on the plate. Particularly, when the air temperature (Ta) is risen from 15ºC to 28ºC, the change in the velocity clearly indicates that, the turbulent stage of the flow develops further downstream of the plate and the locations of the transition points are recorded approximately at y = 0.44 m and 0.62 m respectively.

Additionally, important to note that the velocity grows slowly in the laminar stage, while this growth becomes sharp at the turbulent region. The same behaviour is noticed for the distributions of the turbulent kinetic energy at the turbulent stage. The values of the turbulent kinetic energy and its production in the laminar stage remain approximately zero, but the production of the kinetic energy reaches its peak at the transition stage, followed by a fall to a constant growth towards the downstream. However, it starts to increase slightly again to the far downstream, where the flow becomes fully turbulent.

4.3.4. Further comparisons of the present results with experimental data

In Table 4. 1 comparisons among the analytical, numerical and experimental results of the critical distance and the thickness of the boundary layer along with the Rayleigh number are given. When comparing the Rayleigh number at the beginning of the turbulent flow for the isothermal case of T_P = 54ºC and T_a = 28ºC, general agreement between the three results can be seen. In fact, the numerically obtained Rayleigh number of 4.89×10^8 shows a very close agreement with the experimental result which is 4×10^8 obtained by Charles and Vedats [1968]. But, surprisingly, both the critical distance and the boundary layer thickness show slightly better agreement with the analytical results. For example, the experimental result shows that the turbulent flow starts at 1.01m, while under the same thermal conditions the analytical and numerical investigations predict this critical distance to be 0.75 m and 0.61 m respectively. Changing the operating temperature for the plate as well as for the ambient air, for example when T_P = 60ºC and T_a = 14ºC, a similar behaviour is observed. That is, the Rayleigh number obtained in the numerical simulation shows better agreement with the experiment of Tsuji and Nagano [1988a] than the analytic result. But, the opposite is found in the thickness, while the analytical result is closer to the experiment than the numerical result.

In the case of a flux plate, the results of the Rayleigh number which correspond to the critical distance of 1.5 m - 2.3 m are not available in Yasou et al. [1991], so it was not possible for us to make a direct comparison with the analytical result. However, taking a turbulent Rayleigh number of 2.0×10^{13}, the analytical method predicts the range of the critical distance to be 1.85 m - 2.7 m, which might be a little over-prediction but acceptable given the uncertainty in the

choice of the Rayleigh number. Furthermore, though it was possible to get the Rayleigh number from the paper of Chen et al. [2003], it was not quite clearly mentioned about the value that relates to the critical distance of 2 m. However, the critical distance of 1.67-1.85 m from the analysis at $2.0\times10^{13} \leq Ra^* \leq 10^{14}$ gives again a close agreement to the experiment.

4.4. Conclusion

Development of the shape of the boundary layer of the natural convection flow on a vertical heated plate has been investigated theoretically as well as numerically considering the smooth surface of a vertical plate. Various temperatures of the plate have been employed, and some experimental results of the plate temperature and heat flux have been used as an input data to some calculations in order to make a direct comparison of the predicted results with those of the experiments.

The results showed that the difference between the temperature of air and plate has a significant effect on the transition of the flow from laminar to turbulence. Particularly, we have reported that with an increase in the temperature of both plate and air the critical height as well as the thickness of the boundary layer drops systematically. Specifically, from the theoretical analysis the range of the boundary layer thickness of the laminar flow of air is found to be within the range of 0.017 m – 0.0425 m. Moreover, it is also found that the temperature of the flow and the plate in the isothermal case has a major effect on the transition of the flow. But particularly, when the plate temperature T_p was greater than 60°C, this effect was less pronounced. And under this operating condition, the transition approximatly depends solely on the tempreature of the plate. The investigation on the heat flux surface shows the same behaviour as well, i.e. the

temperature of the flow has a little effect on the transition which is largely affected by the amount of heat flux used.

Furthermore, from the comparison between the results of our calculations and experiments it is reported that the theoretical results predict satisfactorily well the behaviour of the development of the boundary layer of air on the vertical plate. Additionally, the Realizable turbulent model is proved to be a suitable numerical method for predicting the distributions of the thermal properties in both the laminar and turbulent flow regions, leading to the mean characters of the flow such as the temperature and velocity of the flow as well as the turbulent quantities (kinetic energy and its production). Numerical predictions also show satisfactory agreement with various experimental results.

Table 4. 1 Comparison of the transition stage with experimental data

Heated plate		Reference	*(Gr. Pr)* (Turbulent)	Distance L_C (m)	Thickness δ_C (m)
Isothermal	T_p=54˚C T_a=28˚C	Charles and Vedats [1968]	4×10^8	1.01	0.0135
		Analytical	1×10^9	0.75	0.0171
		Numerical	4.89×10^8	0.61	0.0206
	T_p=60˚C T_a=14˚C	Tsuji and Nagano [1989]	3.1×10^9	N/A	0.023
		Analytical	1×10^9	0.62	0.018
		Numerical	1.44×10^9	0.43	0.015
Heat flux	$50\leq q_p\leq202$ (W/m^2)	Yasou et al [1991]	N/A	1.5-2.3	N/A
		Analytical	$Ra^*= 2.0\times10^{13}$	1.85-2.7	
	$200\leq q_p\leq600$ (W/m^2)	Chen et al [2003]	$2.0\times10^{13}\leq Ra^*\leq 10^{14}$	≈ 2	N/A
		Analytical	$Ra^*= 2.0\times10^{13}$	1.67-1.85	

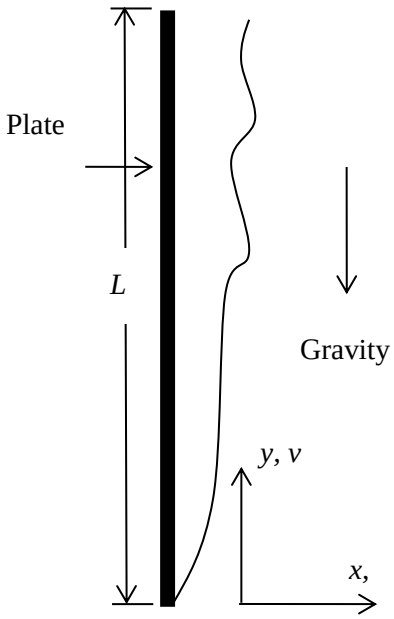

Figure 4. 1 A schematic of the flow geometry with coordinate systems.

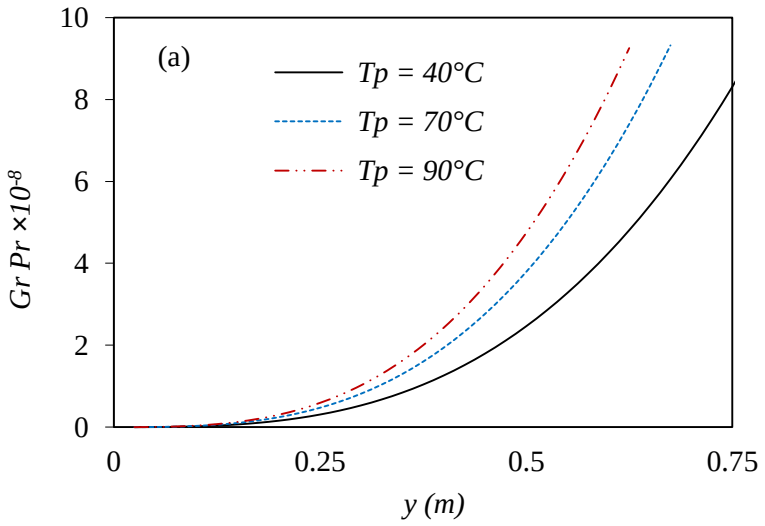

Figure 4. 2 The distribution of the Grashof number at T_a = 25°C.

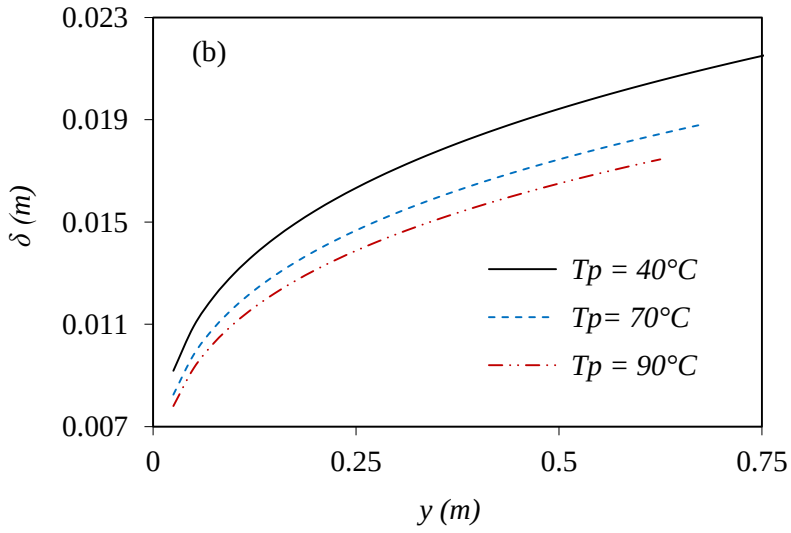

Figure 4. 3 The distribution of the thickness of the boundary layer at T_a = 25°C.

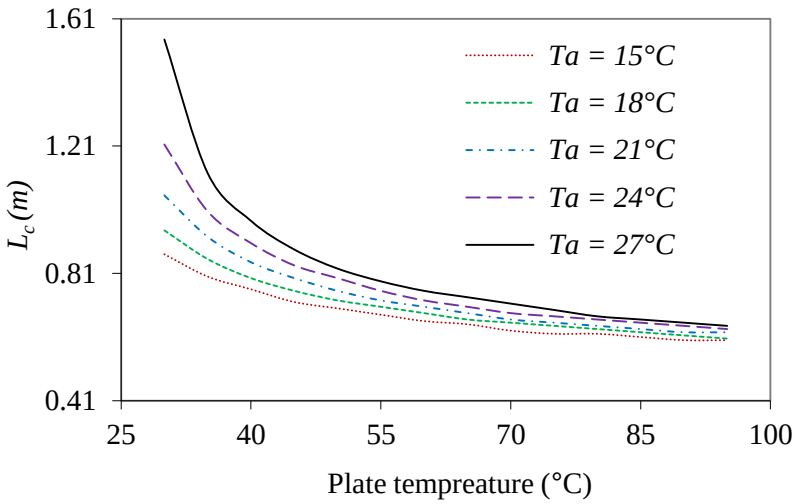

Figure 4. 4 Critical distance for the different plate and air temperatures.

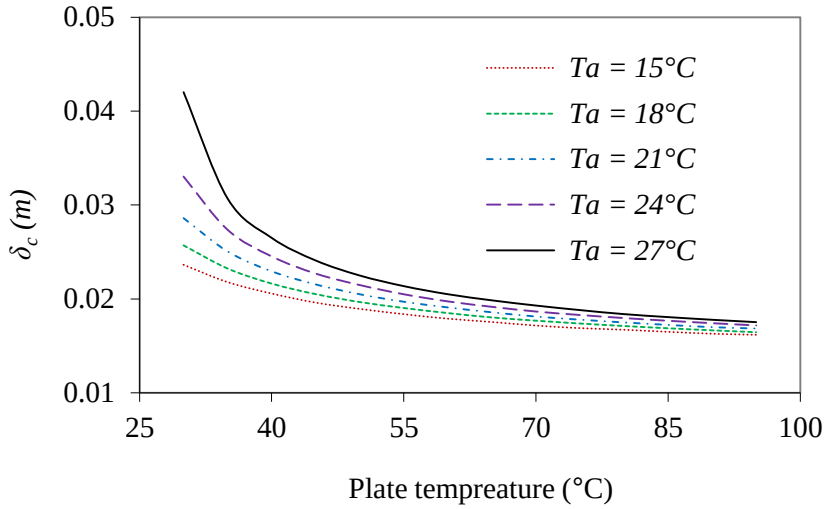

Figure 4. 5 Thickness of the boundary layer for the different plate and air temperatures.

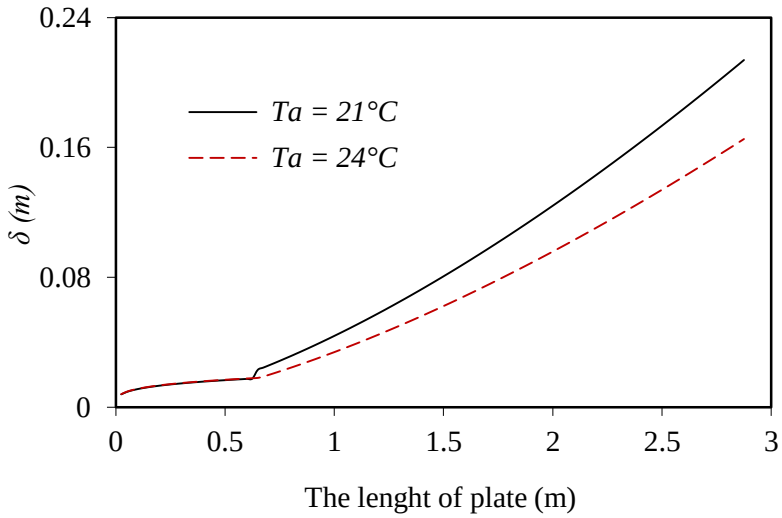

Figure 4. 6 Boundary layer thickness along the heated plate at *Tp* = 90°C.

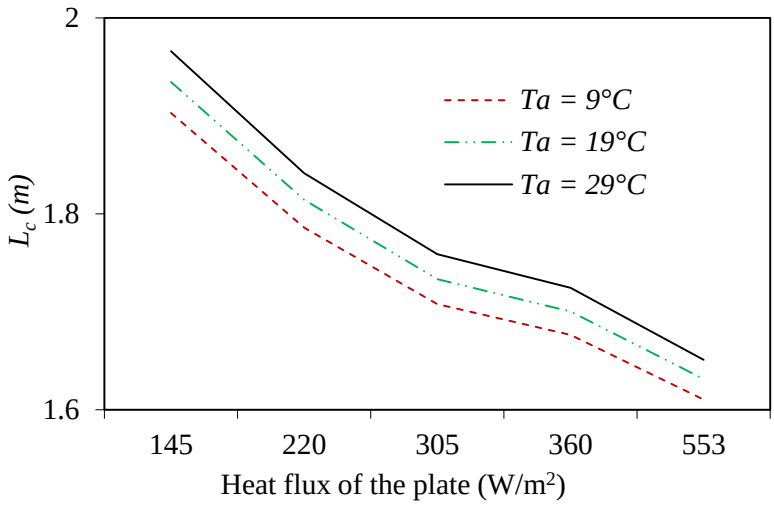

Figure 4. 7 Critical distance of the plate at different heat flux.

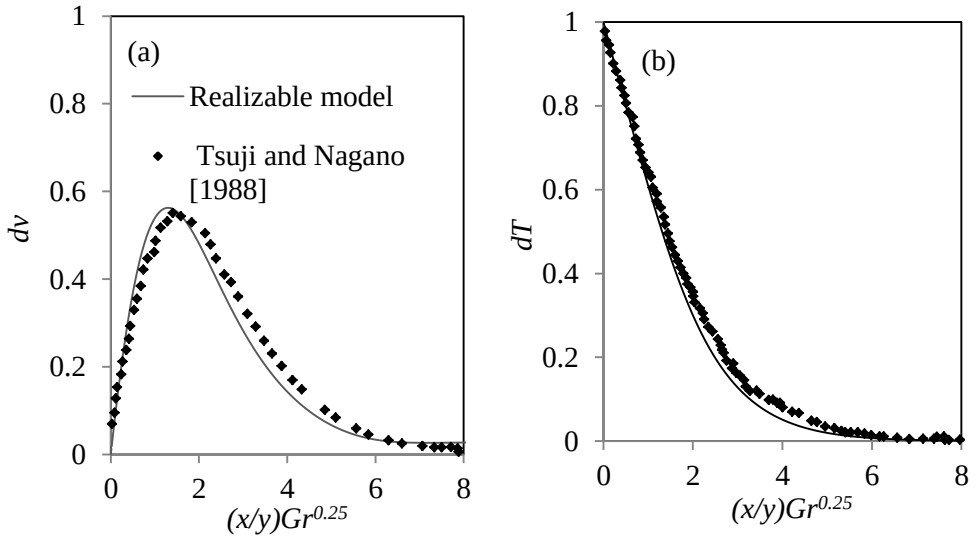

Figure 4. 8 Distribution of the velocity (a) and temperature (b) in the laminar flow.

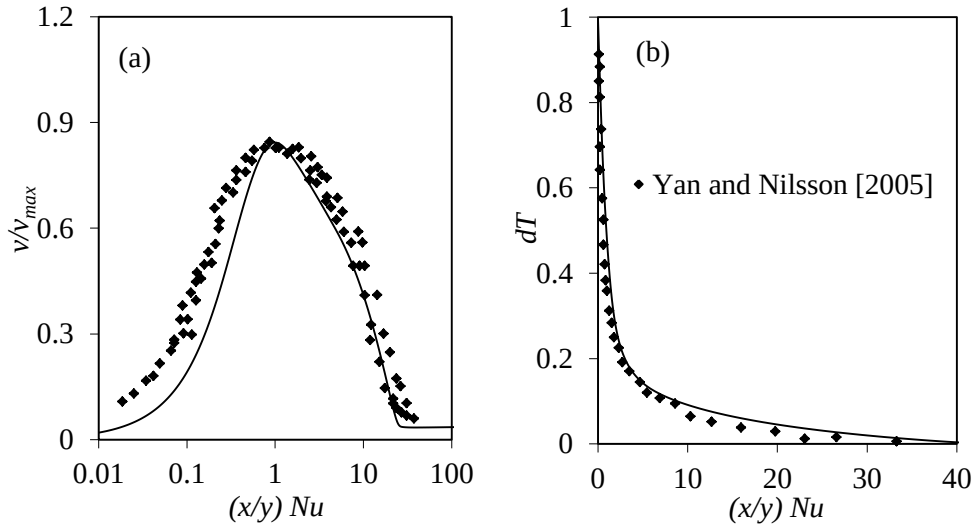

Figure 4. 9 Distribution of the velocity (a) and temperature (b) in the turbulent flow.

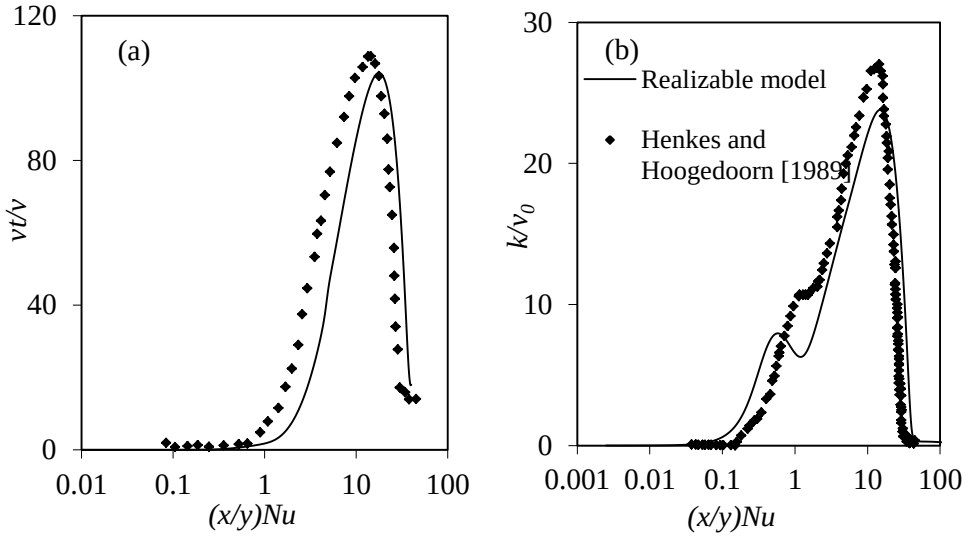

Figure 4. 10 Distribution of the turbulent viscosity and kinetic energy in the turbulent flow.

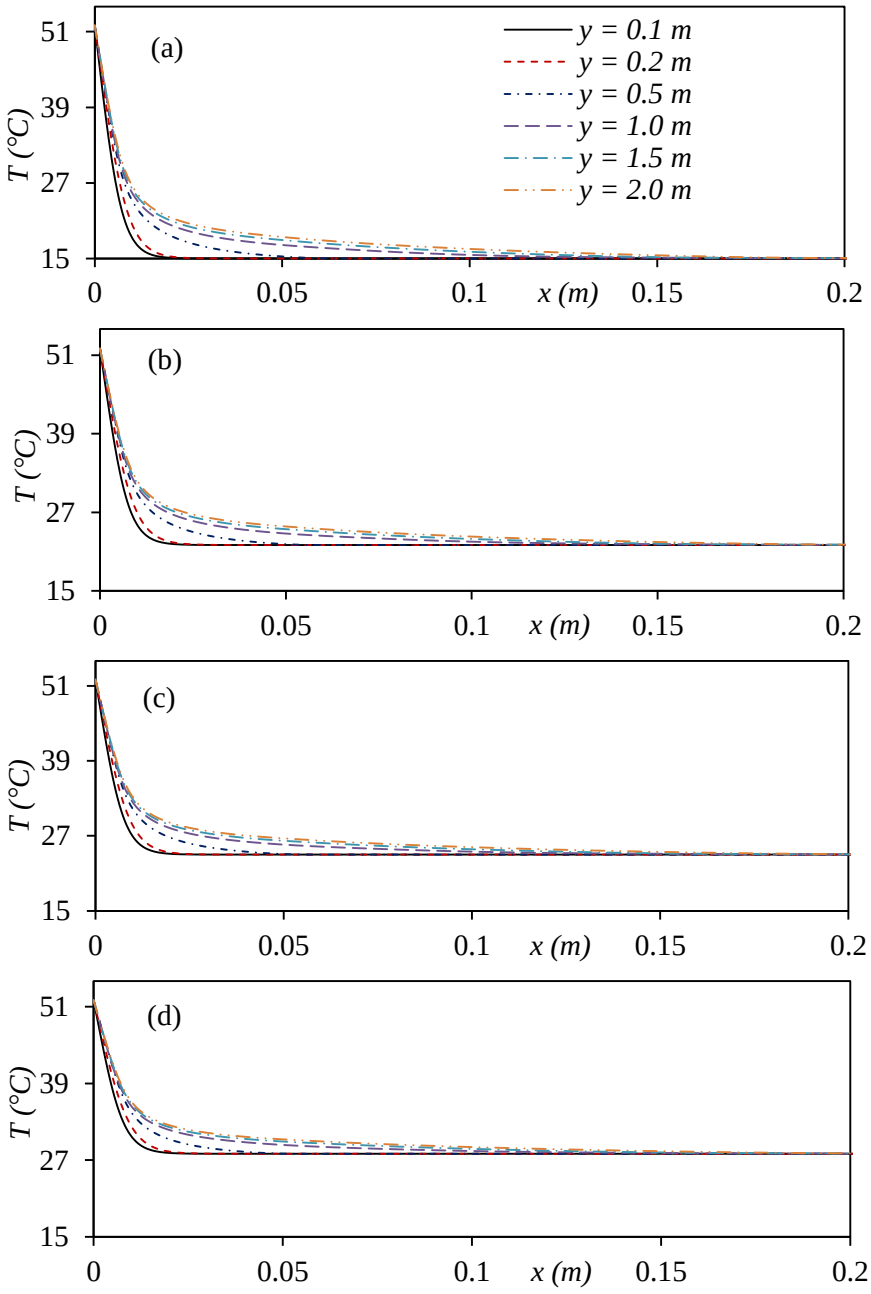

Figure 4. 11 Temperature profiles across the boundary layer for Tp = 54°C where Ta = 15°C (a), Ta = 22°C (b), Ta = 24°C (c), and Ta = 28°C (d)

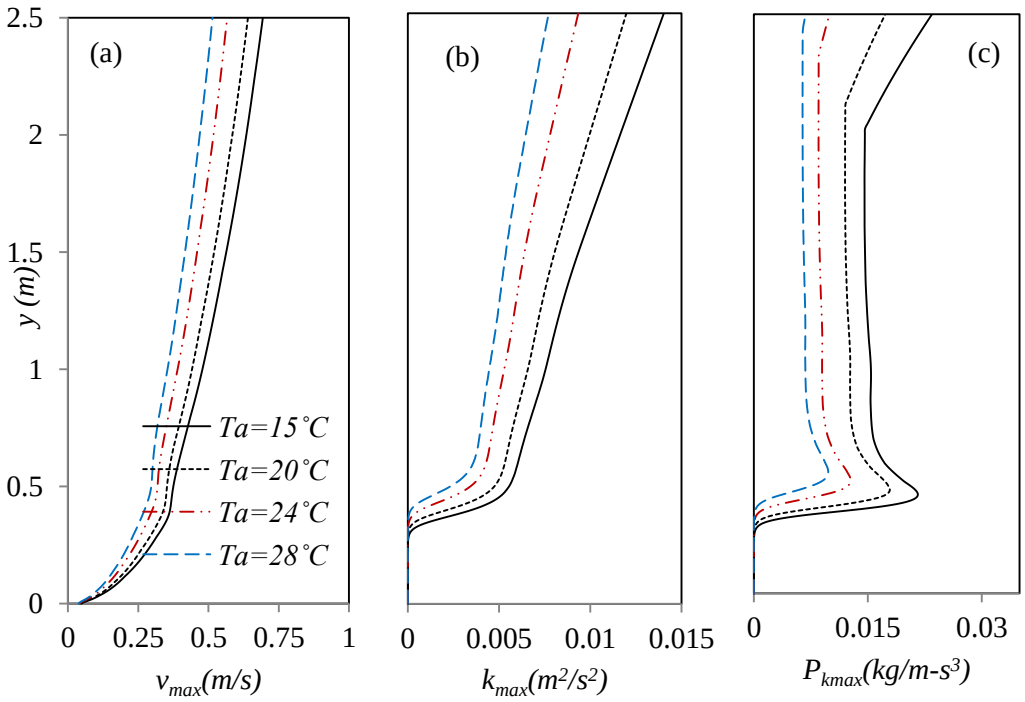

Figure 4. 12 Distribution of the maximum velocity (a), kinetic energy (b) and its production (c).

Chapter 5

Transition of free convection flow in a vertical channel

5.1. Introduction

In this chapter numerical simulations are performed to study the transition of the development of the thermal boundary layer of air along an isothermal heated plate in a large channel which is bounded by an adiabatic plate. In particular, the aim is to investigate the effects of the channel width (b) on the transition of the flow under various plate temperatures. Three different RANS based turbulent k-ε models namely standard, RNG and Realizable with an enhanced wall function are employed in the simulations. The channel width was varied from 0.04 m to 0.45 m and the numerical results of the maximum values of the flow velocity, turbulent kinetic energy were recorded along the vertical axis to examine the critical distance of the developing flow.

5.2. Model geometry

The channel is formed by the two vertical plates with length L, and the distance between the plates is denoted by b. The wall on the left side is isothermal, while the other is adiabatic. The numerical simulations are considered to be two-dimensional free convection and steady state. Air is chosen to be the test fluid. The model geometry along with the Cartesian coordinate system is

shown in Figure 5. 1. For the comparison with the experimental data, the model geometry is studied under the same physical dimensions as the experimental model of Yilmaz and Fraser [2007] where L = 3.0 m and b = 0.1 m.

5.3. Boundary conditions

At the inlet, ambient temperature and pressure conditions are applied so that the air velocity is accelerated from rest to the induced velocity *v*. Moreover, in the case of natural transition, the flow is expected to develop from the laminar state, therefore the turbulent kinetic energy (k) and its dissipation (ε) are set to zero at the inlet.

A uniform temperature is imposed at the heated plate of the channel while the other plate is adiabatic. At the outlet, the static gauge pressure is set to zero and the other flow and turbulent quantities are extrapolated from the interior domain. In the case of any "backflow" occurring through the outlet (which was never the case in these simulations) the temperature and pressure at the outlet of the channel are set to the ambient conditions.

No slip boundary condition is imposed on the velocity components at the walls, where

$u_i = 0$, for $0 \le y \le L$, $x = 0$ and $x = b$.

The thermal boundary conditions for the heated and the adiabatic plate are defined as

$T = Tp$, for $0 \le y \le L$, $x = 0$ and $\frac{\partial T}{\partial x} = 0$, for $0 \le y \le L$, $x = b$.

Moreover, the turbulent kinetic energy vanishes at the wall, so

$k = 0$, for $0 \leq y \leq L$, $x = 0$ and $x = b$.

It is important to note here that when a comparison with the experimental data of Yilmaz and Fraser [2007] is presented, the model is studied under the experimental conditions where the inlet temperature is assumed to be 23°C. The isothermal condition for the heated plate is set at the temperature of 100°C, and the turbulent intensity at the inlet is measured to be 13%. Moreover, the distributions of the characteristics of the flow have large gradients near the wall so standard wall function and an enhanced wall function are used in the boundary layer to present the effect of the viscosity in the inner region.

5.4. Grid resolution test

Mesh dependence study was initially carried out on the Realizable turbulent model to find out a suitable combination of the grid sizes which will be applicable to resolve the flow inside the channel. This mesh dependence study was performed by changing the total number of grid nodes in both the vertical (n_y) and horizontal (n_x) directions by using six different grid resolutions e.g. 22 × 220, 30 × 370, 120 × 370, 200 × 370, 300 × 370 and 200 × 400. Non-uniform structured mesh was generated in the channel with a fine resolution of grid clustered near the inlet and walls by using the mesh-successive ratios of 1.008 and 1.01 respectively.

Figure 5. 2 shows the results of the heated air velocity (v), turbulent kinetic energy (k) and air temperature in three different vertical locations, y = 0.09 m, 1.5 m and 3.0 m. As can be seen both the coarse (especially in the horizontal direction) grids, 22 × 220 and 30 × 370, provide satisfactory results for the velocity and temperature fields, but they severely overestimate the

turbulent kinetic energy production inside the channel. The next four finer grids, 120 × 370, 200 × 370, 300 × 370 and 200 × 400, produce most satisfactory results since the differences found among the results are very small indeed and almost negligible. Therefore, either of these four grids could be used, however to avoid any undesirable discrepancies in the numerical results and at the same time to save the computational time the grid size of 200 × 370 is chosen to perform all the numerical simulations in this Chapter.

5.5. Results and discussions

5.5.1. Assessment of different turbulent models

Three *k-ε* turbulent models are considered in the numerical simulation, standard, RNG and Realizable, to predict the important results such as flow velocity, temperature and kinetic energy. A comparison among the results obtained by the three models is detailed. Note, as reported in Chapter 3, these models differ from each other especially in the way they determine the turbulent viscosity, the turbulent kinetic energy and its dissipations.

Moreover, accuracy of the two wall functions: standard wall function of Launder and Spalding [1972] and enhanced wall function of Kader [1981] is tested and the numerical results are compared with the experiments of Yilmaz and Fraser [2007].

Air temperature

Figure 5. 3 presents the distribution of the air temperature at the outlet of the channel, predicted by the three turbulent models. Frame (a) shows the results with the standard wall function and Frame (b) with the enhanced wall function.

All the numerical results in Figure 5. 3 (a) with the standard wall function show an over prediction compared with the measured data. Only the RNG turbulent model in this case gives slightly better results than the other two turbulent models. However, employing the enhanced wall function with the turbulent models predicts results which are very close to the measurement data. The numerical results also have satisfactory agreement with analytical results reported by Henkes [1990], where without any special treatment close the wall, his analytical results were about 52% higher than the experimental data. While, with the enhanced wall function, the results showed better agreement with the experimental data.

So, it is clear that the numerical simulations of the air temperature are better predicted with an enhanced wall function and the Realizable turbulent model gave the best prediction results compared to the RNG and standard estimations.

Air velocity

The velocity profiles are presented in Figure 5. 4 and Figure 5. 5 at three different vertical locations 0.09, 1.5 and 2.94 m. The velocity simulation at y = 0.09 m shows a symmetric profile as this location is very close to the inlet and the effect of the adiabatic plate is negligible. But this is not true in the experimental data, as they show some asymmetries near the adiabatic plate close to x = 0.09 m, and none of the simulations accurately predicts this behaviour. With an increase in the vertical distance of the heated plate to y = 1.5 m the velocity profiles are affected by the buoyancy force, especially near the heated plate, where the buoyancy force is larger and all the models turbulent fail to predict the peak velocity beside the heated plate. Near the outlet of channel e.g. at y = 2.94 m, Figure 5. 4 (b) and Figure 5. 5 (b), the velocity profile is accelerated more near the heated plate and the opposite

happens beside the adiabatic plate causing a flow deceleration. The vertical velocity profile is approximately smooth and remains flat in the centreline of channel.

Over all, comparing among the three different numerical models, the velocity profile close to the inlet (y = 0.09 m) obtained by the RNG turbulent model with the enhanced wall function model in Figure 5. 5 (a) shows a very good agreement with the experimental data, especially within the range $0 \leq x \leq 0.08$ m. However, with an increase in the channel length, e.g. at y = 1.5 m and near the outlet of the channel, e. g. at y = 2.94 m, the Realizable turbulent model gives numerical results which are close to the experimental data in Figure 5. 5 (c).

Turbulent kinetic energy

The turbulent kinetic energy is recorded in Figure 5. 6 and Figure 5. 7. Figure 5. 6 (a-b) shows that the prediction by the standard wall function with the two turbulent models, standard and RNG, reaches its maximum at the inner layer, which is very close to the heated wall and has disagreement with the experimental data. The experimental data at y = 0.09 m and y = 1.5 m show that the kinetic energy reaches its maximum approximately beside the adiabatic plate, while at y = 2.94 m its peak is approximately at the centreline of the channel. Employing the enhanced wall function with the RNG turbulent model gives better numerical results at y = 0.09 m as can be seen in Figure 5. 7(*b*), however with an increase in the vertical distance, at y =1.5 and 2.94 m, the numerical results of the Realizable turbulent model show slightly better agreement compared with the other models. Although, the numerical prediction of the kinetic energy is lower than the experimental data, the enhanced wall function gives the best results, and at y = 2.94 m the turbulent kinetic energy

reaches its maximum at the centreline of the channel, which also has some agreement with the experimental data. And particularly, the Realizable model predicts numerical results closest to the experiments.

Over all, seeing all the results in Figure 5. 3 - Figure 5. 7 and by employing the enhanced wall function with the three different turbulent models (standard, RNG and Realizable), the percentages of error to calculate the velocity near the outlet are found to be 8.97%, 9.7% and 6.3% respectively. The same comparison can be made for the outlet temperature, which are 1.75%, 1.73% and 1.55% respectively. Therefore, it is clear that the enhanced wall function is capable of predicting the distribution of the outlet temperature with all the models of the turbulent flow. However, comparatively the Realizable turbulent model performed best; therefore it is selected to perform all the other numerical simulations in this Chapter.

By employing the Realizable turbulent model and the enhanced wall function additional results have been presented for the temperature, velocity and turbulent kinetic energy in Figure 5. 3 (a), Figure 5. 5 and Figure 5. 7. These results were obtained by a three-dimensional simulation and the results prove that there is no difference found between the two and three dimensional results. In fact, in the turbulent kinetic energy results there no improvement is seen in the simulation as its magnitude still falls below the experimental data. Furthermore, it is sufficiently proved that the RANS models in both the two- and three-dimensional channel geometries provide the same numerical results, therefore, the choice of a two-dimensional model in the numerical simulations in this and next two Chapters is well justified.

5.5.2. Effect of plate and air temperatures on the transition stage

The transition stage of the developing flow inside the channel is determined by the numerical results of the maximum values of the velocity and turbulent kinetic energy, where the maximum quantities are determined by using $f_{\max}(y) = \underset{x\min \le x \le x\max}{Max} f(x,y)$, where f is a generic function, and plotted along the vertical axis y.

Figure 5. 8 shows the predictions of the maximum velocity, kinetic energy, turbulent intensity and heat flux on heated plate respectively where the channel width is fixed at b = 0.1 m. As can see, with an increase in the plate temperature (Tp) from 50˚C to 100˚C, generally the transition of the flow from the laminar to turbulent stage starts early.

From Frames (*b*) and (*c*), the distribution of the kinetic energy and turbulent intensity in the laminar region can be divided to two stages, the first one where the kinetic energy equal to zero and the second stage where the distribution of the kinetic energy starts to grow on the two sides of the plate channel as can be seen in in Figure 5. 9 where the contour plot of the kinetic energy and turbulent intensity are plotted, the results indicate that, after the transition stage, both the turbulent kinetic energy and turbulent intensity grow sharply in the turbulent region Figure 5. 9 (A-B).

The effect of the air temperature on the transition is presented in Figure 5. 10 by fixing the plate temperature at Tp = 70˚C. The similar behaviour of the development flow can be seen, however, with increasing the air temperature the transition starts later, in Figure 5. 11, the contour plot of the kinetic energy

and turbulent intensity are reported where it reaches its maximum at the outlet section.

Since the peak of the temperature and velocity distributions from the heated plate can be considered to be the transition starting stage, the location of the minimum point of the local heat flux should also correspond to the transition point. In Figure 5. 12 the critical distance on the plate, derived from the maximum velocity and kinetic energy is presented. More specifically, the results show that at a constant air temperature e. g. Ta = 15˚C with an increase in the plate temperature by 100%, e. g. from 50˚C to 100˚C, the critical distance of the plate droops by 16.4%., while at constant plate temperature Tp = 70˚C, with increase air temperature by 100% e. g. 10˚C to 20˚C, the critical distance of the plate increases by 4.13% Figure 5. 13. So it is clear that, the temperature of the plate has more effect on the transition compared to the air temperature.

5.5.3. Effect of channel width on the transition stage

Numerical results of the velocity, turbulent kinetic energy and local heat flux are presented in this section to investigate the effects of the width of the channel on the process of transition occurring inside the channel. The heated plate of the channel is kept as isothermal at 70°C with the inlet air temperature of 15°C, but the width of the channel is varied from 0.04 m to 0.45 m to study the transition effects. To avoid any ambiguity in presenting the numerical results, the profiles are divided into two groups: the first group presents the results of the width from b = 0.04 m to b = 0.1 m; whereas the second one from b = 0.15 m to b = 0.45 m.

Figure 5. 14 (a) shows that the maximum velocity for the width b = 0.04 m to 0.1 m reaches its maximum at the transition point, then it starts to drop slightly and after that the growth becomes approximately constant towards the downstream of the channel. For the turbulent kinetic energy in Figure 5. 14 (b), its value is initially zero at the inlet and within the laminar region of the channel. But the kinetic energy grows rapidly in the region where the transition begins, and the growth remains steady within the whole transition region, followed by a sharp increase in the region of the turbulent flow in most cases. Specifically, for a small width of the channel, e.g. at b = 0.04 m and 0.05 m, the kinetic energy reaches its peak approximately at $y \approx 1.5$ m, while for b = 0.06 m and 0.10 m the location of peaks becomes later at y = 1.8 m and 2.4 m respectively.

In the second group, the results in Figure 5. 14 (c) show that the growth of the velocity profile at b = 0.15 m to 0.45 m is gradual in the laminar flow region, but just after the transition point it drops slightly and then increases again towards the downstream because of the presence of turbulence. The nature of the growth in the kinetic energy is reported in Figure 5. 14 (d) for b = 0.15 m and 0.2 m remains quite similar, e.g. rapid rise at the beginning of the transition and then steady within the transition region, and finally sharp rise at the downstream. However, the transition region found for b = 0.30 m and 0.45 m is relatively small compared to the other cases, and the growth of the kinetic energy becomes similar to that found in the one-heated plate case. As the turbulent intensity is another parameter of turbulence quantities, defined as the ratio of the root of mean square of the velocity fluctuations to the average of the mean velocity of the flow, the turbulent intensity inside the channel is more affected by upstream history at the inlet of channel. So it can be used to estimate the development of the flow, Figure 5. 15.

Figure 5. 16 (A) shows the contour plots of the turbulent kinetic energy inside the channel. As can be seen the turbulent kinetic energy reaches its maximum at the outlet of channel for the width $b \geq 0.08$ m. But for $b \leq 0.06$ m it reaches its maximum in the range 1.5 m $\leq y \leq$ 2.5 m. The distributions of the turbulent intensity are shown in Figure 5. 16 (B), which show some interesting features of the growth of turbulence in the channel. Particularly, when the width is reduced, the intensity also grows on the right side of the channel where the adiabatic plate is located.

Physical dimensional results of the velocity distribution are plotted in Figure 5. 16 (C). As can be seen the maximum velocity field is located approximately on the left side of the channel near the heated plate as a result of the buoyance force. The growth of the thickness of the boundary layer of the flow for width $b \leq 0.15$ m is not clear due to the fact that there is not enough space available to develop the boundary layer. But with an increase in the width of the channel $b \geq 0.2$ m, the thickness of the boundary in turbulent flow becomes very clear. However, as seen in Figure 5. 16, the distribution of the kinetic energy as well as the intensity is complicated, especially in the range of the channel width smaller than 0.20 m, where the kinetic energy grows on the both sides of the channel. So, to understand the growth of the kinetic energy in more details within the channel the results are divided into two regions and presented in Figure 5. 17, where the maximum kinetic energy is first calculated in the range of $0 \leq x \leq b/2$ to look into the growth near the heated plate on the left hand side of the channel and plotted in frames (a) and (c). Whereas the maximum of the same is recorded in the range of $b/2 \leq x \leq b$ to particularly focus on the turbulence production near the adiabatic plate and shown in frames (b) and (d).

As evidenced in Figure 5. 17 (a), the kinetic energy on the heated plate grows early with dropping the width of the channel from b = 0.04 m to b = 0.10 m.

Although the right side plate of the channel is kept as adiabatic, the kinetic energy still grows on it especially for the channel width b = 0.04 m to 0.20 m, see Figure 5. 17 (b) and (d). But, for a large channel width e.g. b = 0.30 m and 0.45 m, in Figure 5. 17 (d), the growth of the kinetic energy on the right side can be ignored since the maximum distribution of the kinetic energy is found inside the channel.

The maximum values of the turbulent intensity in the channel for $0 \leq x \leq b$ are presented in Figure 5. 18 (*a*) and (*b*), as can be seen the turbulent intensity has the same structural of development as the turbulent kinetic energy in Figure 5. 17, but effect of the adiabatic plate is very clear on the left side in the large channel width at b = 0.30 m, where the growth of the turbulent intensity is very large on the adiabatic plate compared to the growth of the kinetic energy. These differences can be seen more clearly in the contour plots of the turbulent kinetic energy and turbulent intensity in Figure 5. 16 (A) and (B).

Since the peak of temperature and velocity distribution from the heated plate can be considered to be a starting point of the transition stage according to Katoh et al. [1991], where the location of a minimum point of the local heat flux should also correspond to the transition point, the three different parameters of the heated air such as the velocity, turbulent kinetic energy and local heat flux are used to predict the transition point inside the channel with different values of the width. The values of the critical distance at the transition point are derived from the velocity, kinetic energy and heat flux plate already presented in Figure 5. 14 and Figure 5. 19 and now summarised in Figure 5. 20.

Figure 5. 20 shows that the transition points predicted by the turbulent kinetic energy are very close to those estimated by the velocity distribution in all the

cases. In addition, for a large channel width $b \geq 0.1$ m the local heat flux also predicts the critical distance that agrees well with other two results.

However, for a small channel width e.g. b = 0.04 m to 0.08 m Figure 5. 20 shows that the local heat flux reaches its minimum further upstream of the channel and does not agree with the predictions of the velocity and the turbulent kinetic energy. The possible reason for that is that both the thermal and the thickness of the boundary layer increase sharply in the turbulent flow compared to the laminar flow due to the effects of the buoyancy force on the heated plate. Additionally, at a small width of the channel there is not enough space for the boundary layer to grow fully which would eventually carry the heat from the heated plate; so as a consequence, the specific heat transfer of the air reaches its maximum temperature early.

Moreover, Figure 5. 20 also shows that the location of the transition point shifts to a higher distance towards the downstream of the channel when the channel width is increased from b = 0.04 m to 0.08 m. And, particularly, at b = 0.08 m the critical distance reaches its maximum of 1.53 m in the middle of the channel, where the Grashof number calculated as a function of this critical distance of the velocity is 2.8×10^{10} (Figure 5. 21). However, as seen, the transition occurs early when the channel width is increased from b = 0.10 m to 0.45 m, and the critical distance at the channel width of 0.45 m becomes similar to that obtained by the one vertical heated plate since the effect from the adiabatic plate at a far distance is negligible. Importantly, the Grashof number (Figure 5. 21) at the critical distance for Ta = 15°C and b = 0.45 m is estimated to be 2.27×10^{9} and 1.17×10^{9} for the one plate case, which has a close agreement to $\approx10^{9}$ obtained by Bejan [1995] in the free convection flow on an isothermal vertical plate.

5.5.4. Effect of width on the thermal boundary layer

To investigate the effects of the width of the channel on the distributions of the thermal boundary layer of the heated air developing inside the channel as well as on its thickness, results of the air temperature, velocity and turbulent kinetic energy are reported in the horizontal direction (x) at different vertical locations; near the entrance (at y = 0.5 m), outlet, middle of the channel (at y = 1.5 m), and the critical location (at $y = Lc$). The width of the channel is varied from b = 0.04 m to b = 0.2 m.

The axial dimensionless temperature profiles which are plotted in Figure 5. 22 at different heights show a general trend i.e. the temperature besides the isothermal plate is maximum which then drops to the adiabatic plate on the right. The profiles also show a gradual increase in the air temperature from the inlet towards the downstream of the channel in all the cases due to the growth of the thermal boundary layer along the channel. But the boundary layer growth is affected by the channel width. Particularly, as can be seen in frames (a-e), when b is reduced from 0.2 m to 0.04 m, the outlet temperature at the adiabatic plate increases.

The variation of the turbulent mean velocity across the channel is plotted in Figure 5. 23 for the same channel width. As can be seen the velocity at the inlet increases gradually when the channel width b is reduced. Moreover, in all the cases the peak of the velocity profile appears beside the heated plate (on the left side) as expected; but when b is increased, the velocity peaks become sharp and move towards the heated plated, indicating a rapid acceleration of the air flow near the heated plate. However, the magnitude of the velocity drops first

slowly from their peaks and then rapidly towards the adiabatic surface on the right side, clearly seen in Figure 5. 23 (a–d) for b = 0.04 m to 0.10 m. In contrast, the velocity profiles for b = 0.15 m and 0.20 m, and particularly at the outlet, show a sharp drop to the adiabatic plate and remain almost flat at the critical distance within a wide range of the channel section. This characteristic behaviour of the velocity profiles predicted inside the channel has also a good agreement with the experimental data of Katoh et al. [1991].

Additionally, the peak velocity at the transition point for the width of 0.04 m to 0.10 m is higher than that at the outlet section, in Figure 5. 23 (a–d); this is possibly due to the enhanced turbulent mixing within the relatively small width of the channel. Whereas, for b = 0.15 m and 0.20 m, in Figure 5. 23 (e–f), the peak velocity at the outlet becomes higher than the transition section; and these issues are further explored in more details in Figure 5. 24 where the peak velocity at the transition point and at the outlet section of the channel is compared. The results show that with an increase in the width of the channel from 0.04 m the peak velocity at the outlet section of the channel initially drops and becomes less than that of the critical distance. However, after about 0.1 m the peak velocity at the outlet increases slightly and becomes larger than the transition stage when $b > 0.12$ m.

The distributions of the turbulent kinetic energy are presented in Figure 5. 25. The results show that the prediction profile of the turbulent kinetic energy for the channel width b = 0.04 m to 0.08 m is larger at the middle of the channel (y = 1.5 m) than that of the outlet section especially near the heated plate. Moreover, the kinetic energy for b = 0.04 m and 0.06 m reaches its peak near the adiabatic plate as shown in Figure 5. 25 (a–b). Whilst in the rest of channels, when width $b \geq 0.08$ m, the turbulent kinetic energy at the outlet

section reaches its peak approximately at the middle of the channel, i.e. at $x = b/2$.

5.5.5. Effect of width on the outlet parameters

To present the effects of the channel width on some outlet parameters, different cases are presented with various ranges of air temperature 15˚C, 25˚C and 30˚C while the plate temperature is kept as 70˚C. The outlet parameters such as the air velocity, the rate of mass and the percentage of added temperature are reported here.

The result shows that for the inlet temperature 15˚C and 30˚C with an increase in the channel width from 0.04 m to 0.10 m, the average outlet velocity in Figure 5. 26 (a) decreases by 24% and 30% respectively. While for increasing channel width from 0.10 m to 0.45 m the average outlet velocity drops of ~60% remains approximately constant. In general, with an increase in the channel width, the difference in the outlet velocity between the three values of the air temperature becomes small.

As the rate of mass flow $\dot{m}$ becomes a function of the channel width, the results in Figure 5. 26 (b) show that the rate of mass flow increases with the channel width. However, the added temperature of the flow rate drops as can be seen in Figure 5. 26 (c), where the effect of the thermal properties of air is more clear. In terms of percentage, the added temperature for b = 0.04 m and b = 0.45 m with the air temperature of 15˚C and 30˚C drops by 2.19% and 0.72% respectively.

5.6. Conclusion

Numerical results of the transition inside a channel have been presented here giving a particular attention to the effects of the channel width on the distributions of the velocity, kinetic energy, temperature and plate heat flux. The results in the turbulent flow have been compared satisfactorily with the experimental data among with the three different turbulent models namely the standard, RNG and Realizable k-ε. Importantly, an enhanced wall function has been applied to the surfaces to account the developing boundary layers, and the results showed that the Realizable turbulent model gave the least error compared to the other two models. To present the effects of the thermal conditions on the transition stage, initially fixed the width at b = 0.10 m but varied the plate temperature. The results showed an increase in the plate temperature caused an early transition of the flow since the critical distance dropped. The critical distance estimated from the distributions of the velocity and the turbulent kinetic energy along the vertical channel agree very well.

Additionally, I have found that the width of the channel has a major effect on the transition. For example, with an increase in the channel width from b = 0.04m to 0.08m the transition delays, and particularly the critical distance reaches its maximum at b = 0.08 m with the Grashof number of 2.8×10^{10}. On the other hand, the transition occurs early when the channel width is increased from 0.08m, and the critical distance at b = 0.45m becomes similar to that of the single plate case. Moreover, for $b \geq 0.10$ m the values of the critical distance, which are a function in the local heat flux, are very close to the distribution of the velocity and kinetic energy; but for the small width e.g. when $b \leq 0.08$ m, the local heat flux reaches its minimum in a location which is far away from the critical distance obtained by the velocity and kinetic energy.

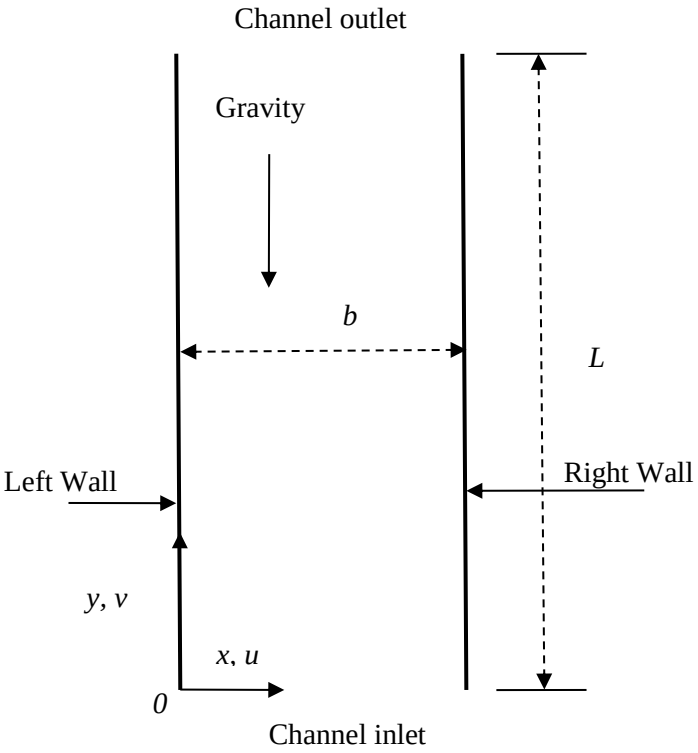

Figure 5. 1 The vertical parallel plate channel.

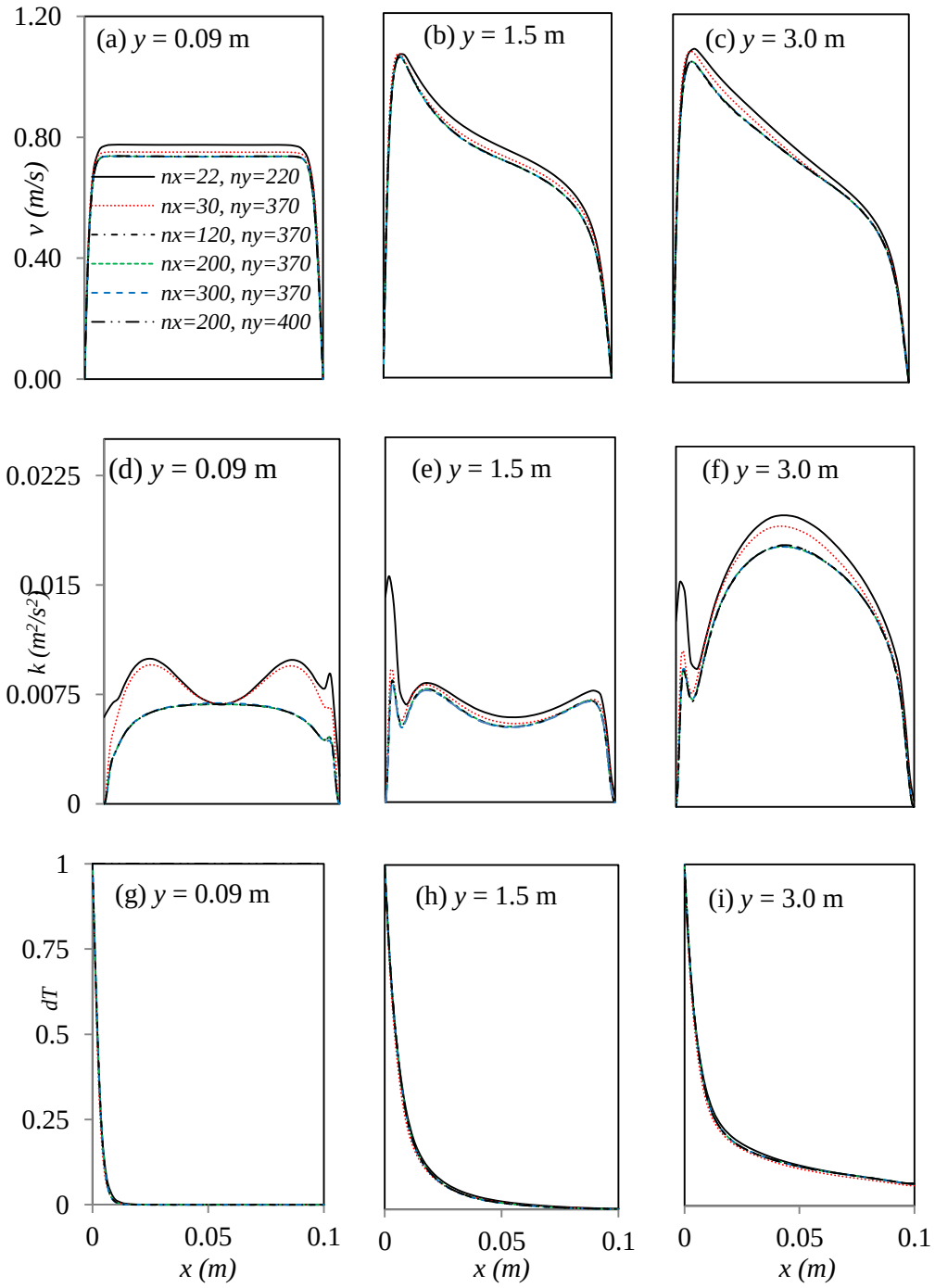

Figure 5. 2 Mesh dependence test showing the results of velocity, turbulent kinetic energy and air temperature.

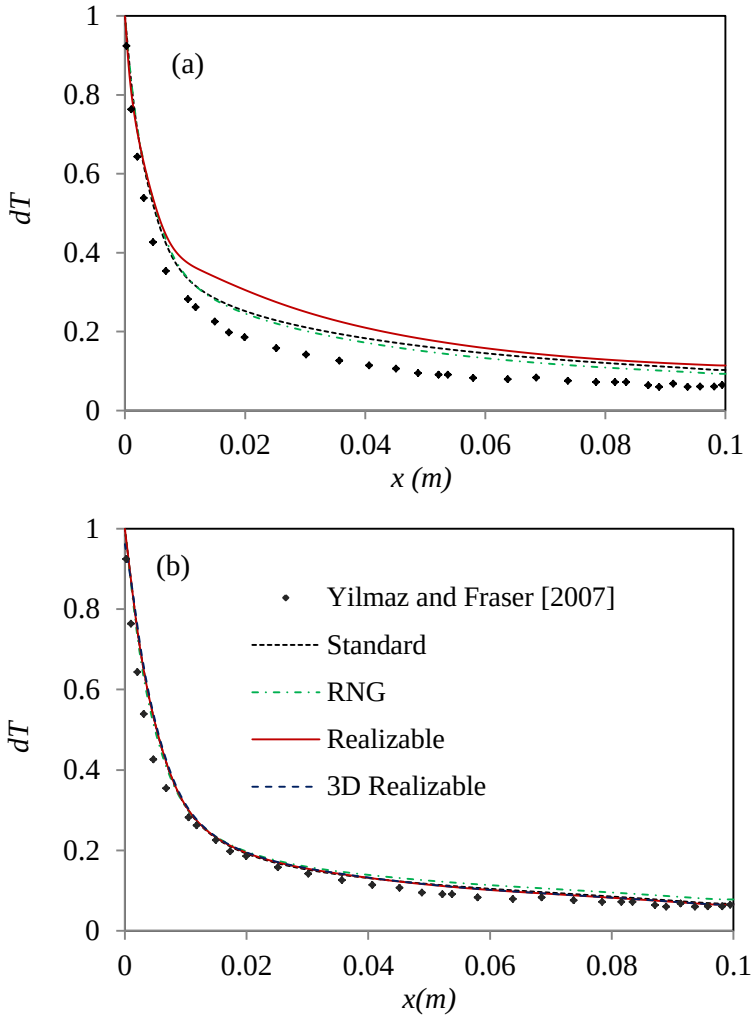

Figure 5. 3 The distribution of outlet temperature at y = 3.0 m, with standard wall function (a) and with enhanced wall function (b)

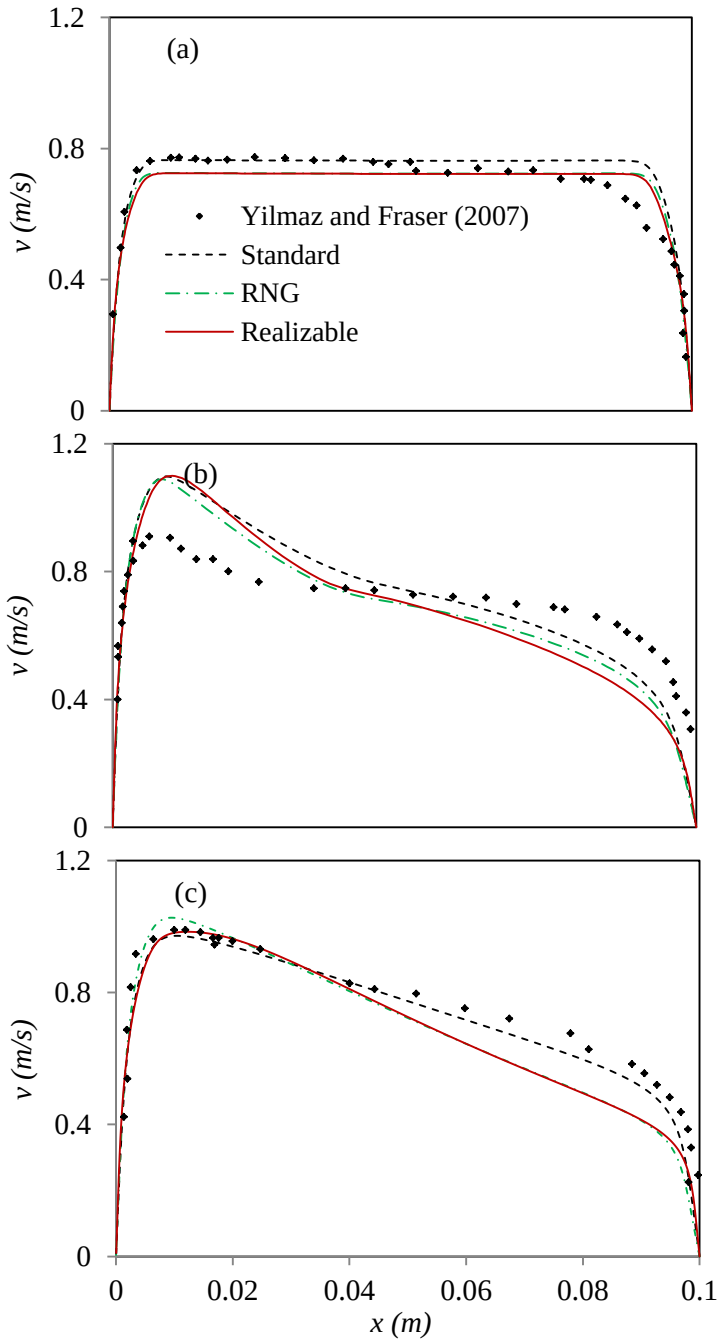

Figure 5. 4 The velocity distribution at y = 0.09 m (a), y = 1.5 m (b) and y = 2.94 m (c) with standard wall function.

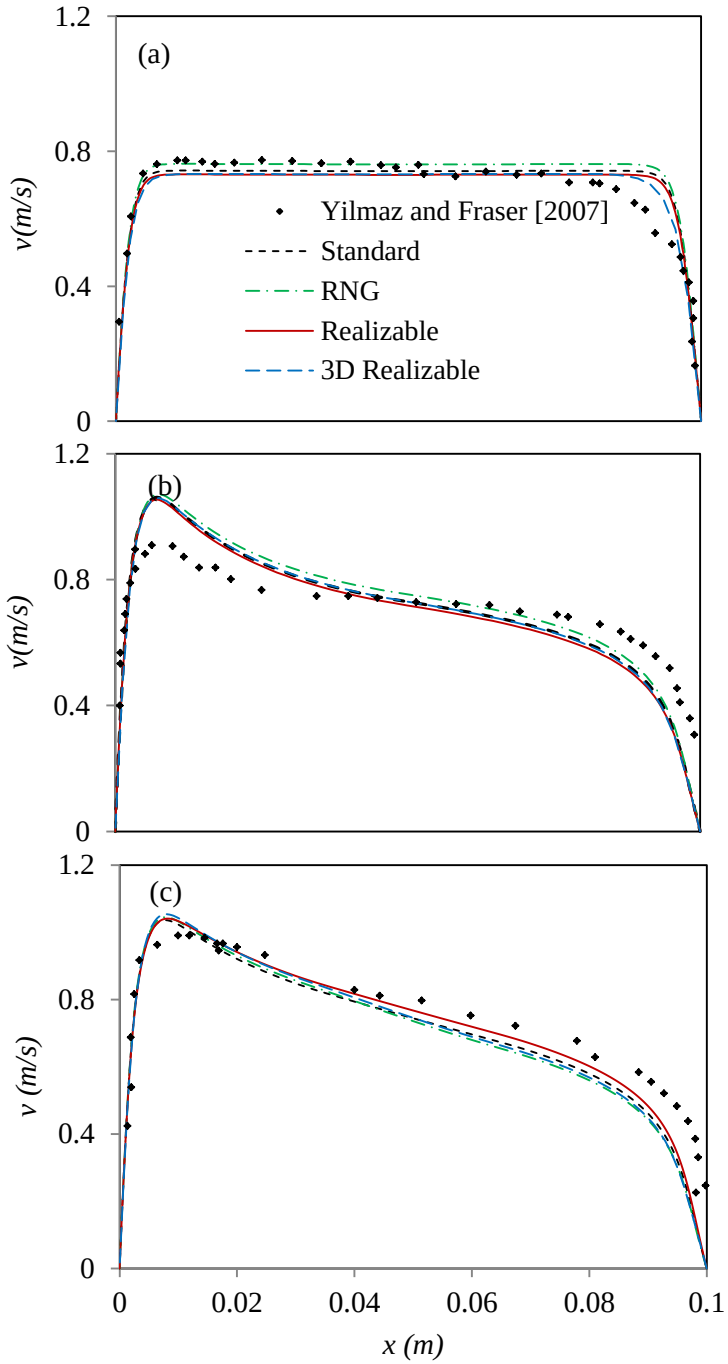

Figure 5. 5 The velocity distribution at y = 0.09 m (a), y = 1.5 m (b) and y = 2.94 m (c) with enhanced wall function.

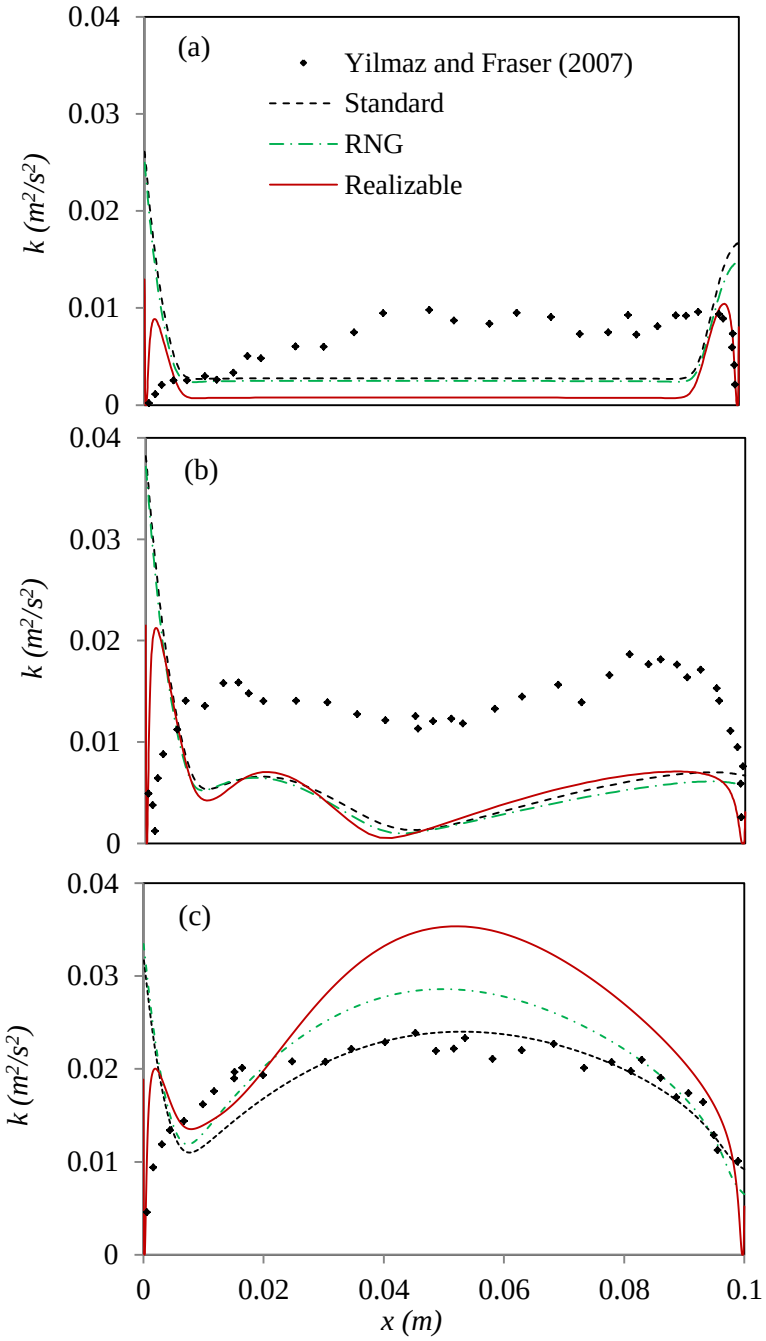

Figure 5. 6 The kinetic energy distribution at y = 0.09 m (a), y = 1.5 m (b) and y = 2.94 m (c) with standard wall function.

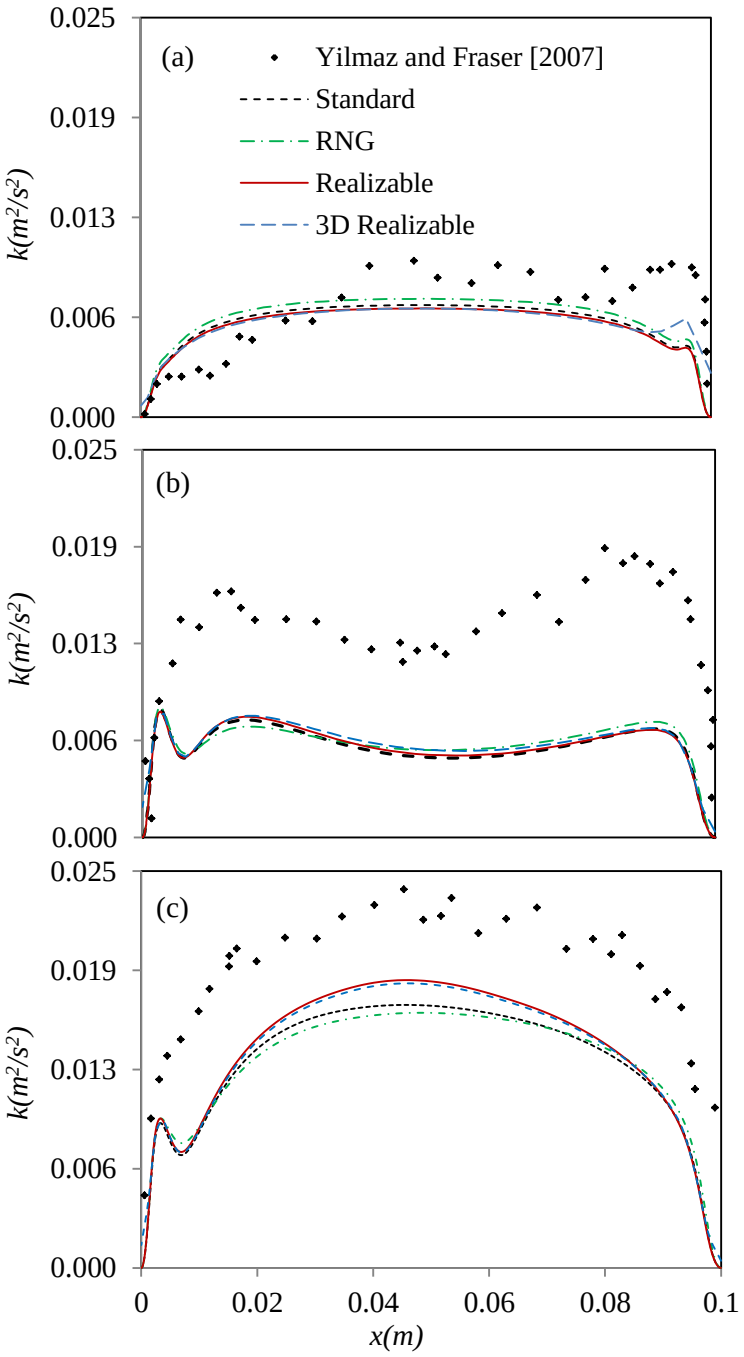

Figure 5. 7 The kinetic energy distribution at y = 0.09 m (a), y = 1.5 m (b) and y = 2.94 m (c) with enhanced wall function.

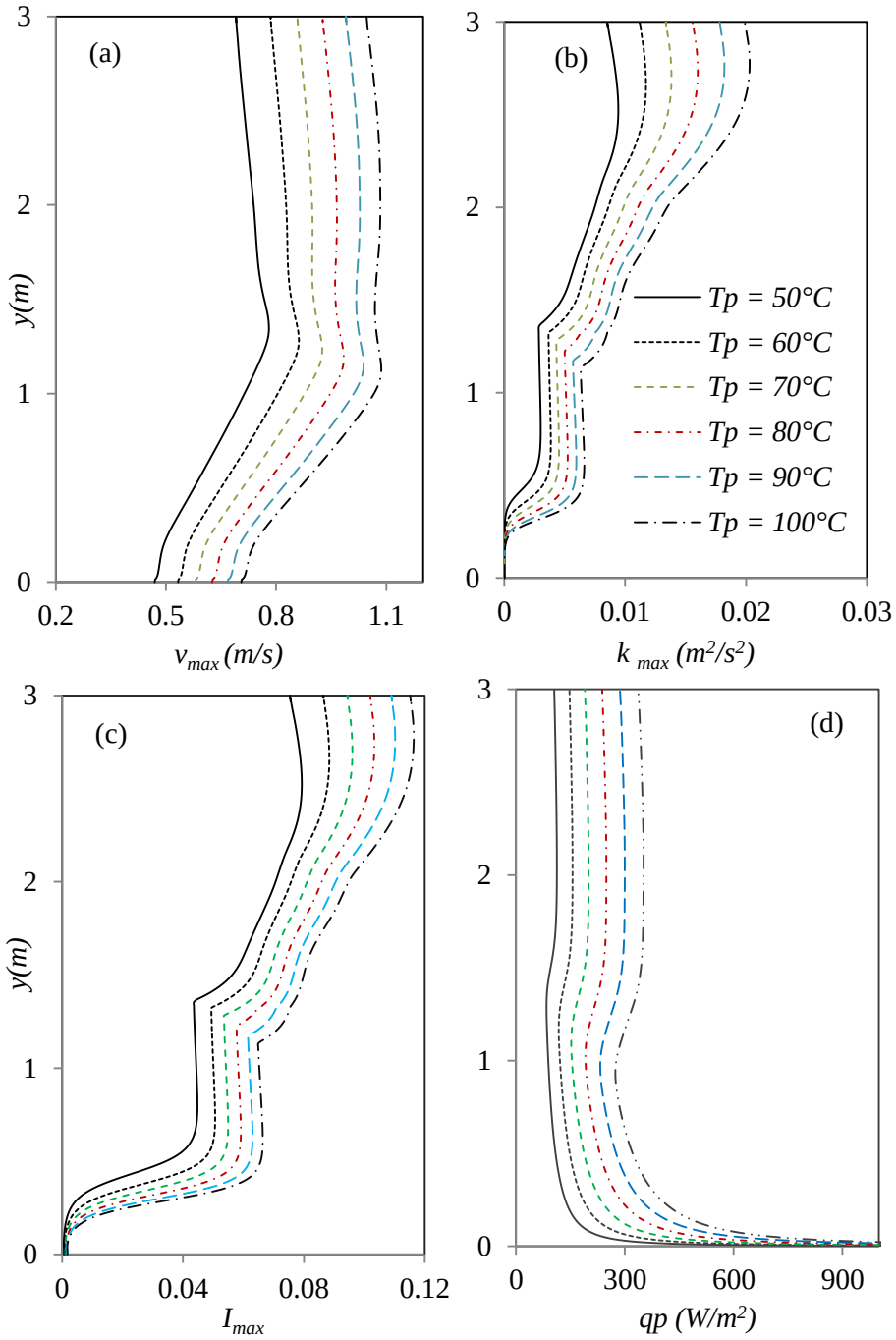

Figure 5. 8 Distribution of the maximum velocity (a), kinetic energy (b), turbulent intensity (c) and heat flux (d) at b = 0.1 m and Ta =15°C.

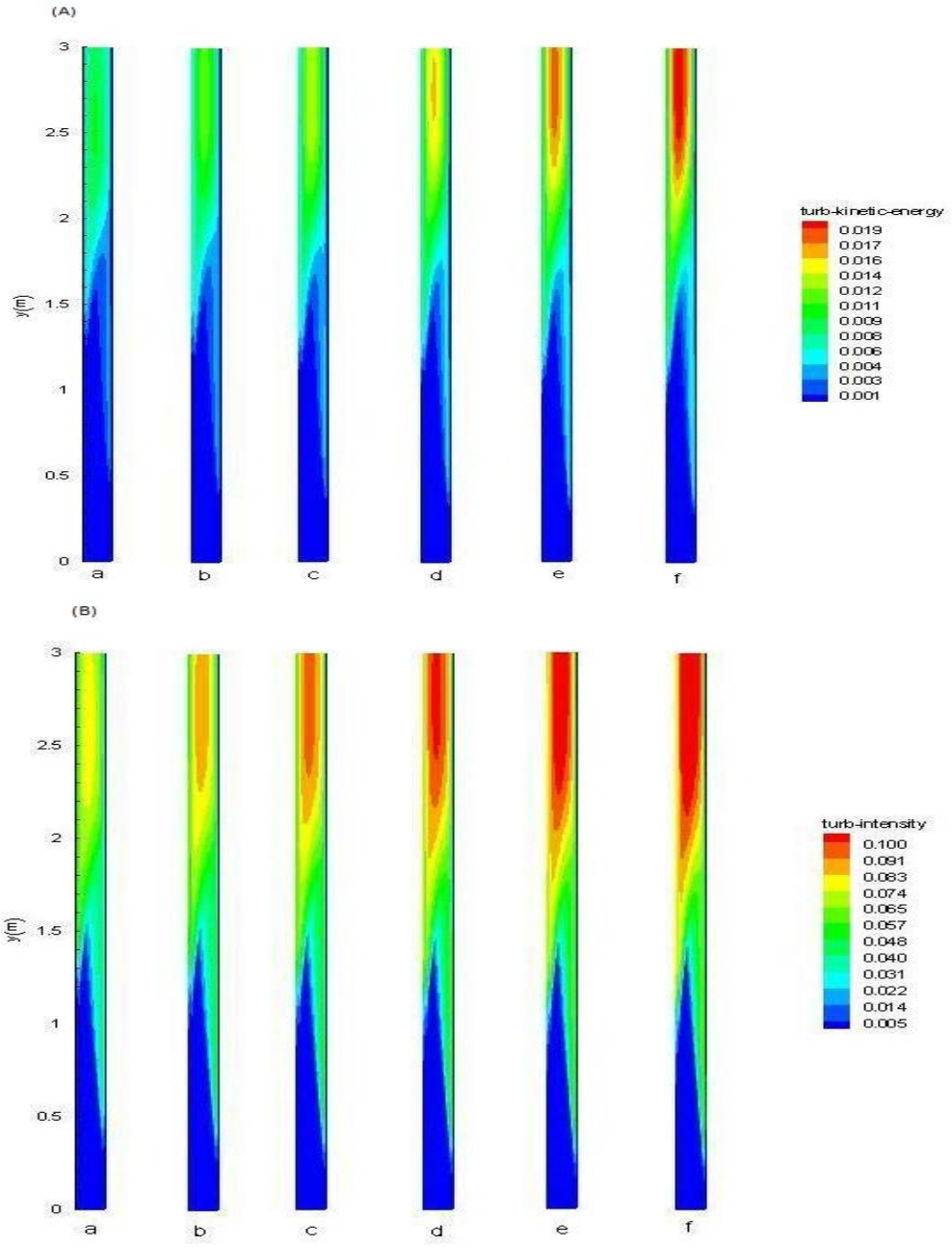

Figure 5. 9 Contours of the turbulent kinetic energy (A) and turbulent intensity (B) for *Ta* = 15°C and *b* = 0.10 m with *Tp* (*a*) 50°C, (*b)* 60°C, (*c*) 70°C, (*d*) 80°C, (*e*) 90°C and (*f*) 100°C

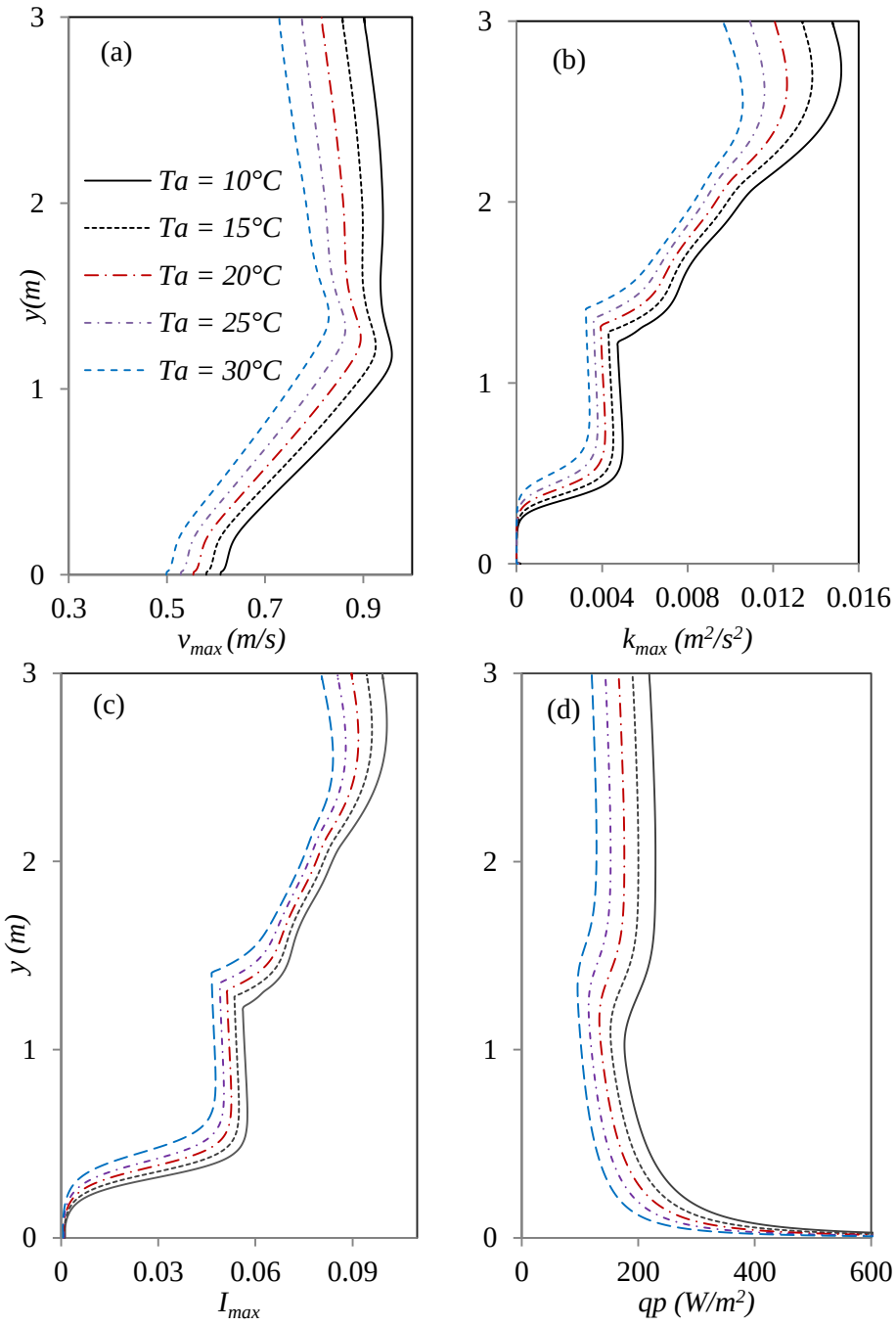

Figure 5. 10 Distribution of the maximum velocity (a), kinetic energy (b), turbulent intensity (c) and heat flux (d) at b= 0.1 m and Tp=70°C.

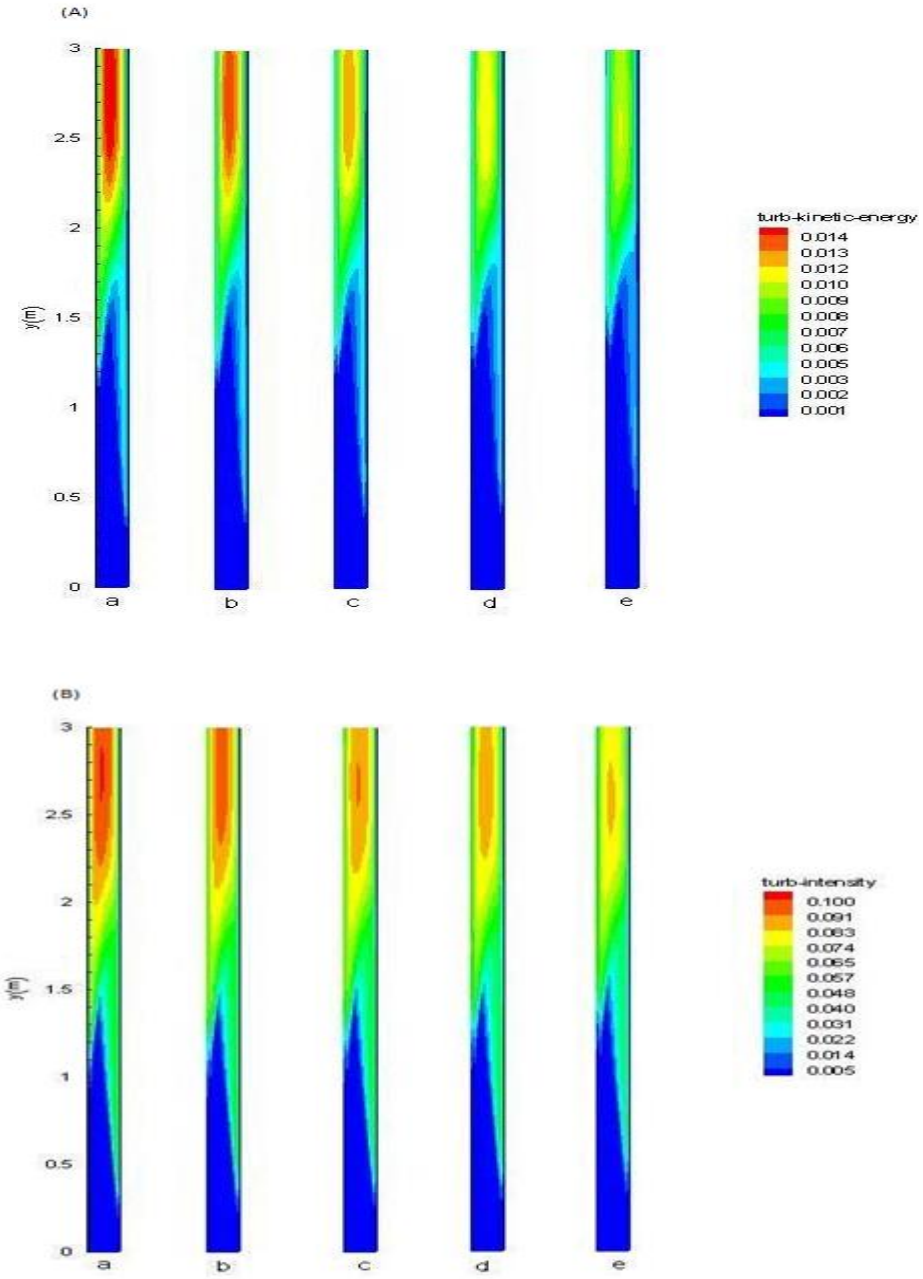

Figure 5. 11 Contours of the turbulent kinetic energy (A) and turbulent intensity (B) for *Tp* = 70°C and *b* = 0.10 m with *Ta* (a)10°C, (b) 15°C, (c) 20°C, (d) 25°C and (e) 30°C.

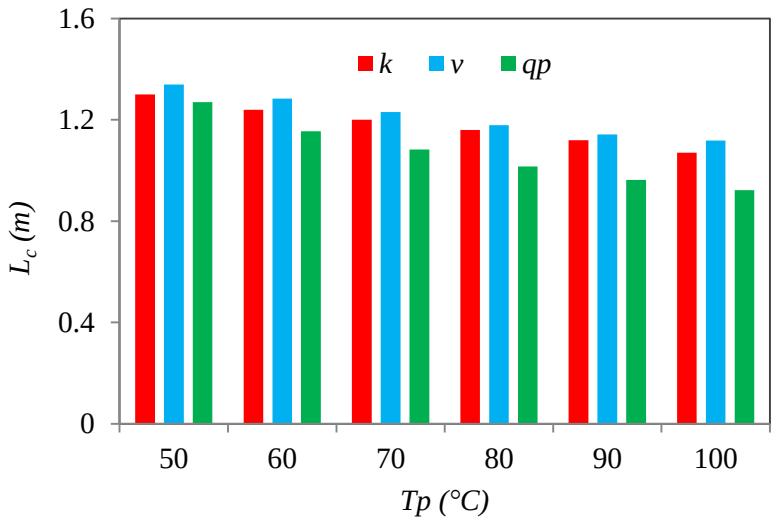

Figure 5. 12 The critical distance derived from the velocity and kinetic energy at b = 0.1 m and Ta =15°C.

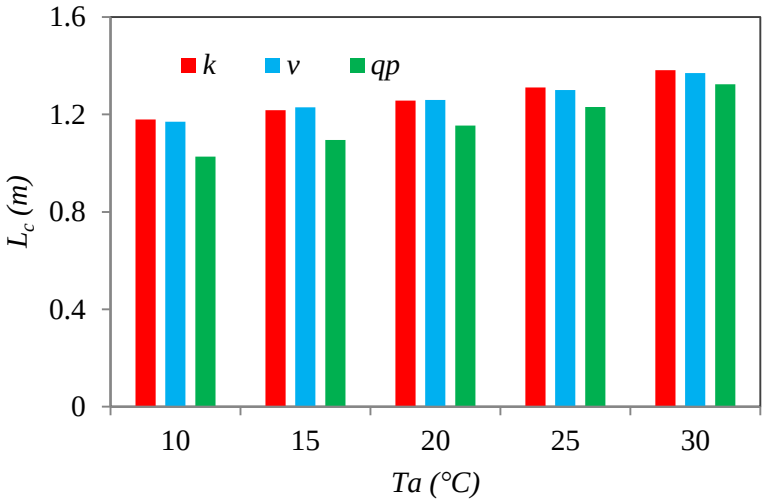

Figure 5. 13 The critical distance derived from the velocity and kinetic energy at b = 0.1 m and Ta = 70°C.

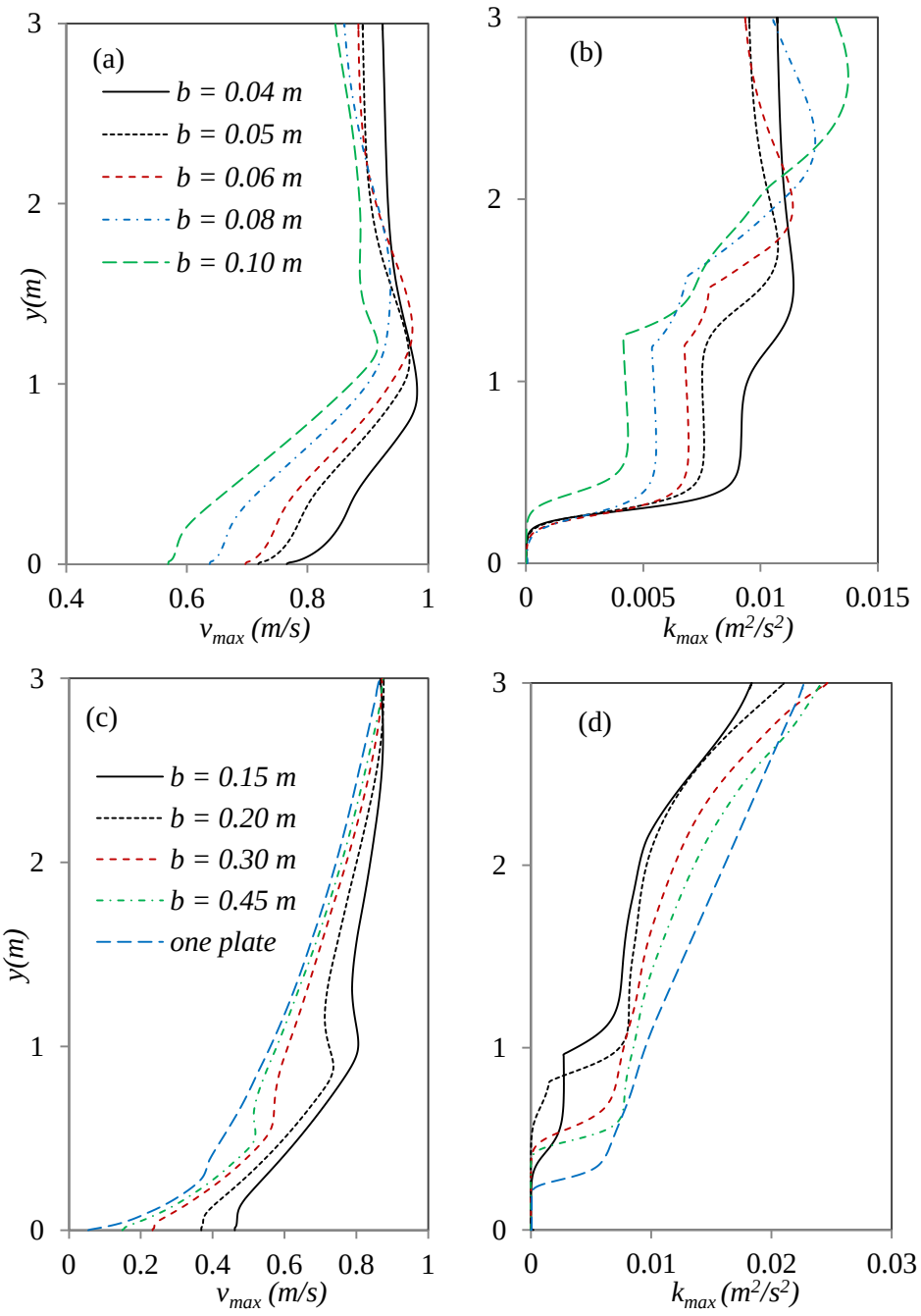

Figure 5. 14 The distribution of the velocity (a, c), turbulent kinetic energy (b, d) and inside the channel at *Ta* = 15°C and *Tp* =70°C.

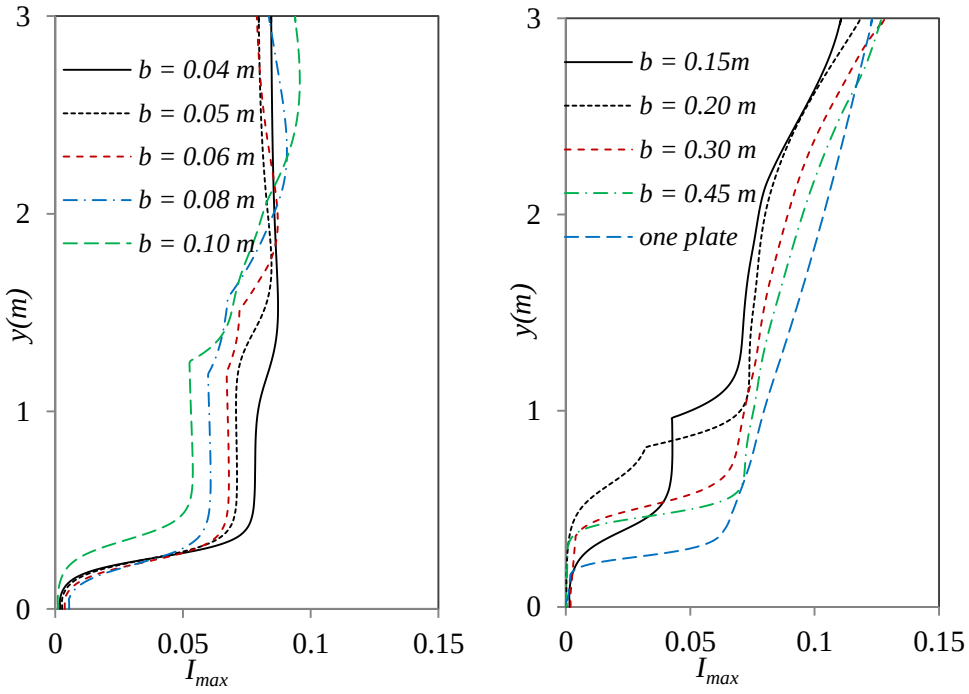

Figure 5. 15 The distribution of the turbulent intensity inside the channel at *Ta* = 15°C and *Tp* =70°C.

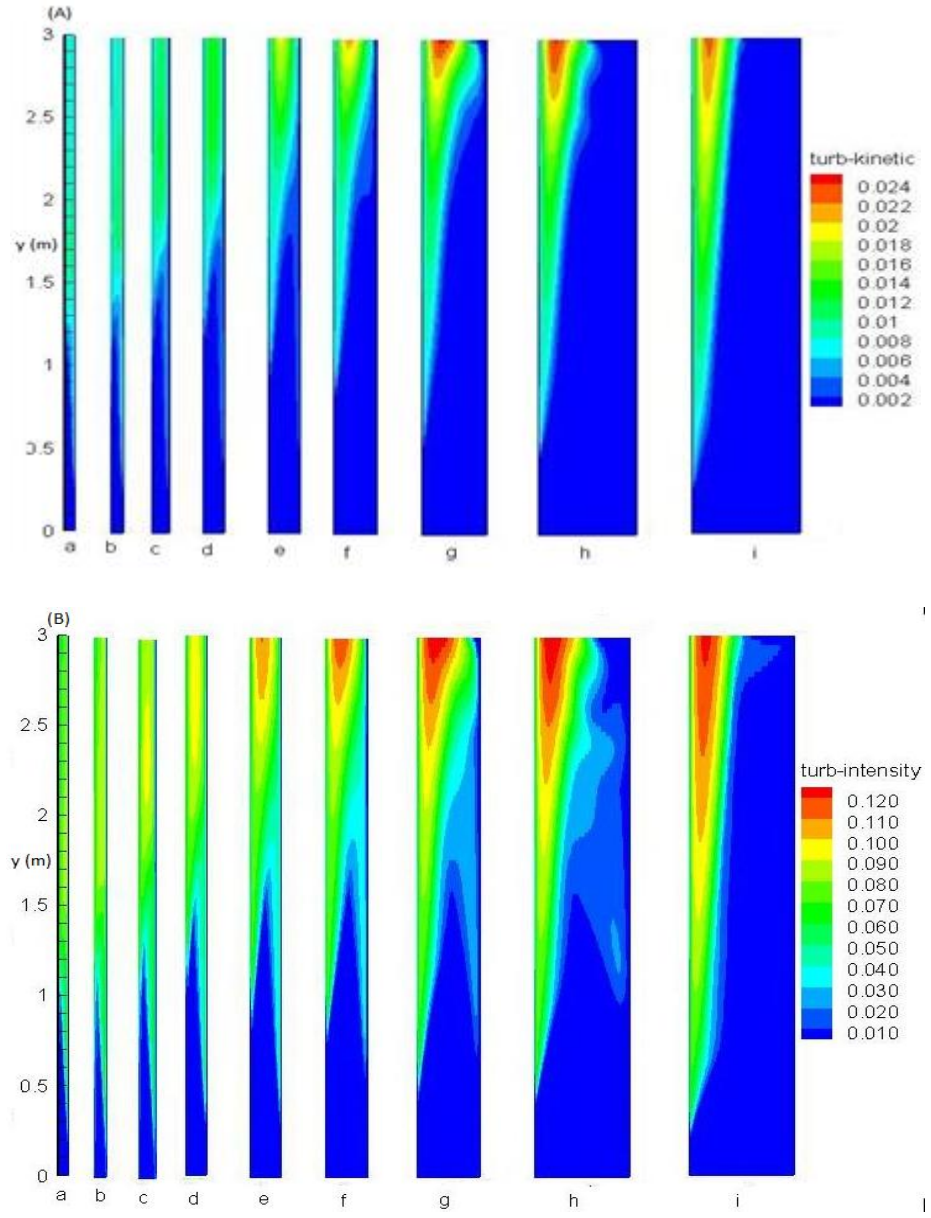

Figure 5. 16 Contours of the turbulent kinetic energy (A), turbulent intensity (B) and velocity (C) for Tp = 70°C and Ta = 15°C, where the width of the channel is (a) 0.05 m, (b) 0.06 m, (c) 0.08 m, (d) 0.10 m, (e) 0.15 m, (f) 0.20 m, (g) 0.30 m and (h) 0.45 m. Note frame (i) is the one plate case.

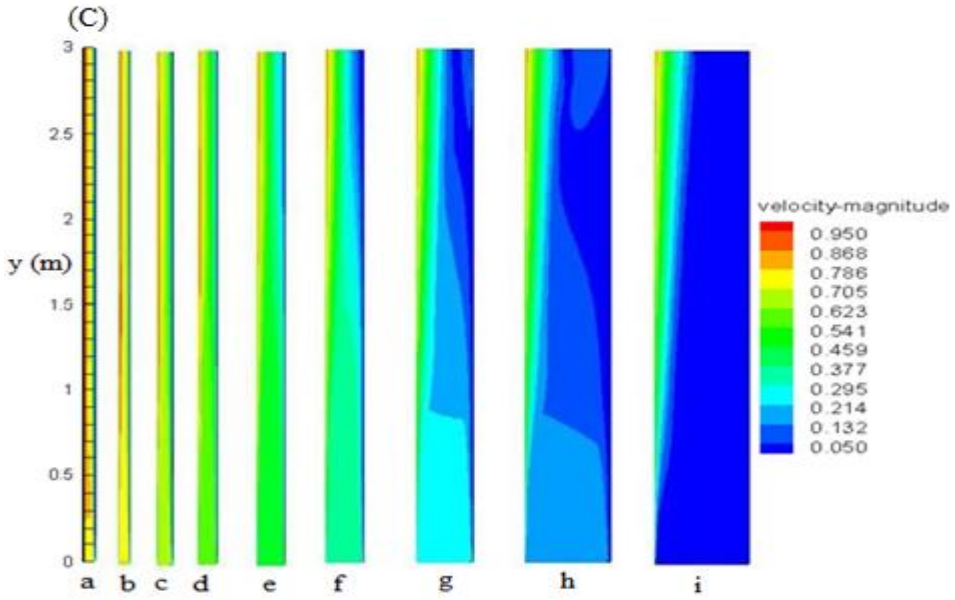

Figure 5. 16 Caption continued.

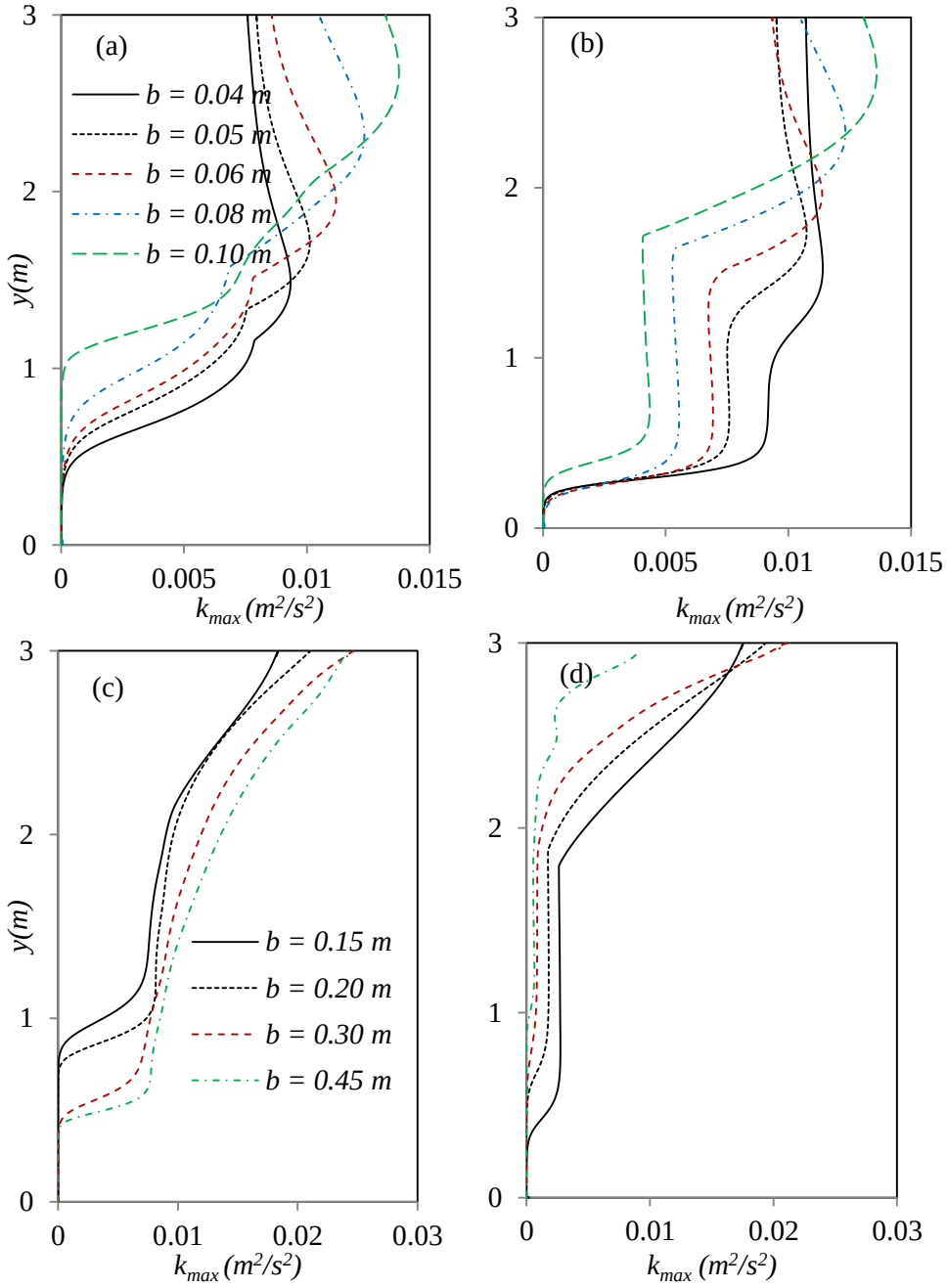

Figure 5. 17 The distribution of the turbulent kinetic energy inside the channel at Ta = 15°C and Tp =70°C where (a, c) the left side and (b, d) the right side of the channel.

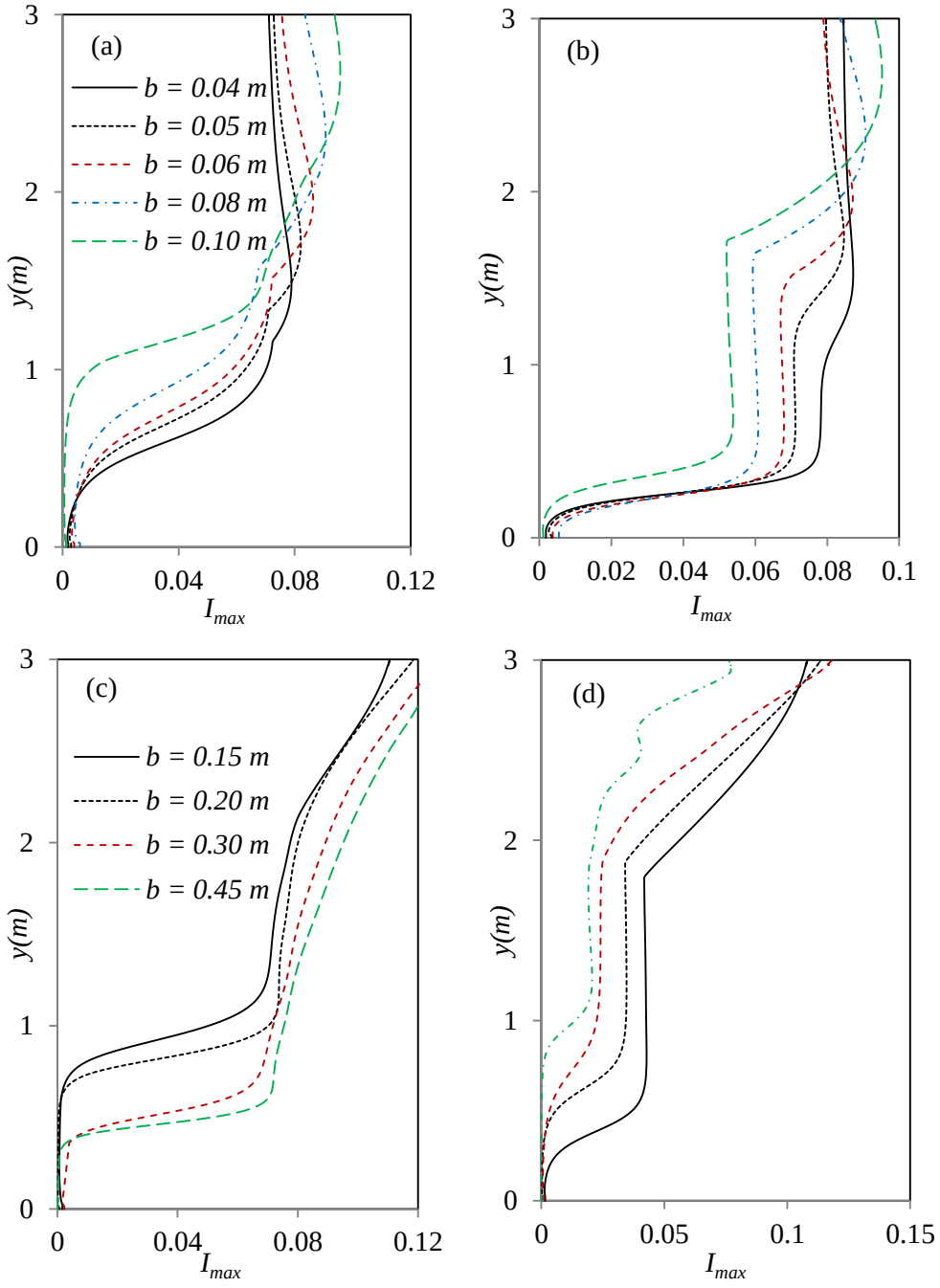

Figure 5. 18 The distribution of the turbulent intensity inside the channel at *Ta* = 15°C and *Tp* = 70°C where (a, c) the left side and (b, d) the right side of the channel.

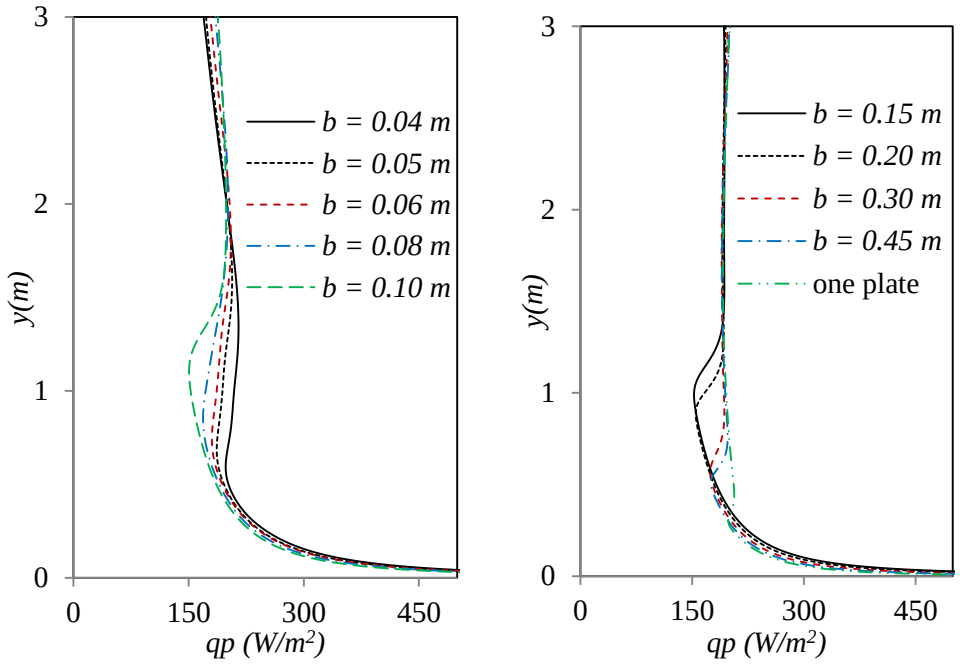

Figure 5. 19 The distribution of local flux on heated channel at *Ta* = 15°C and *Tp* =70°C .

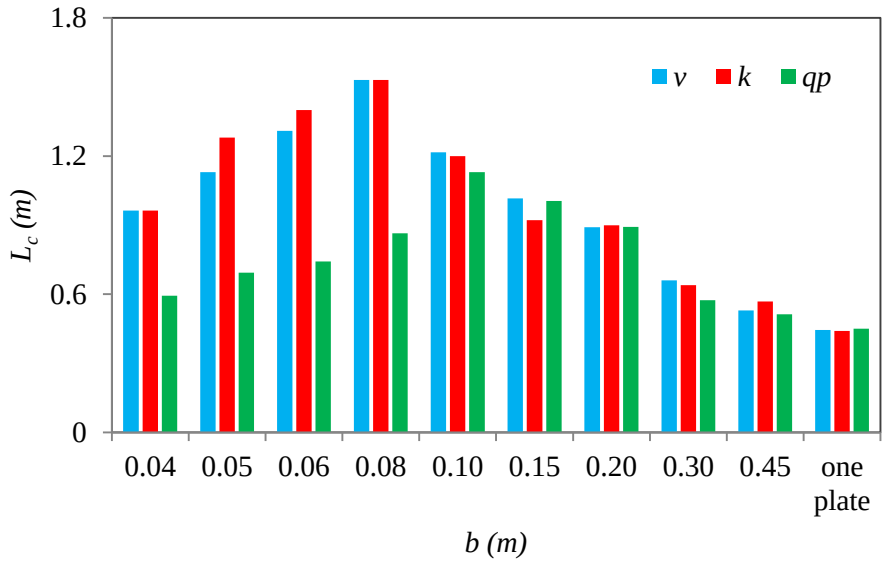

Figure 5. 20 The critical distance inside the channel at *Ta* = 15°C and *Tp* =70°C.

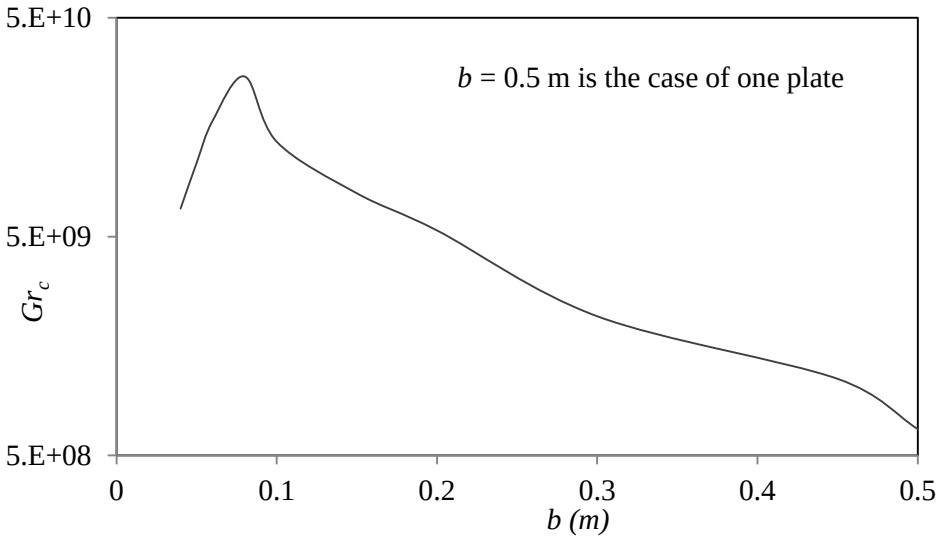

Figure 5. 21 The Grashof number at the critical distance for *Ta* = 15°C and *Tp* = 70°C.

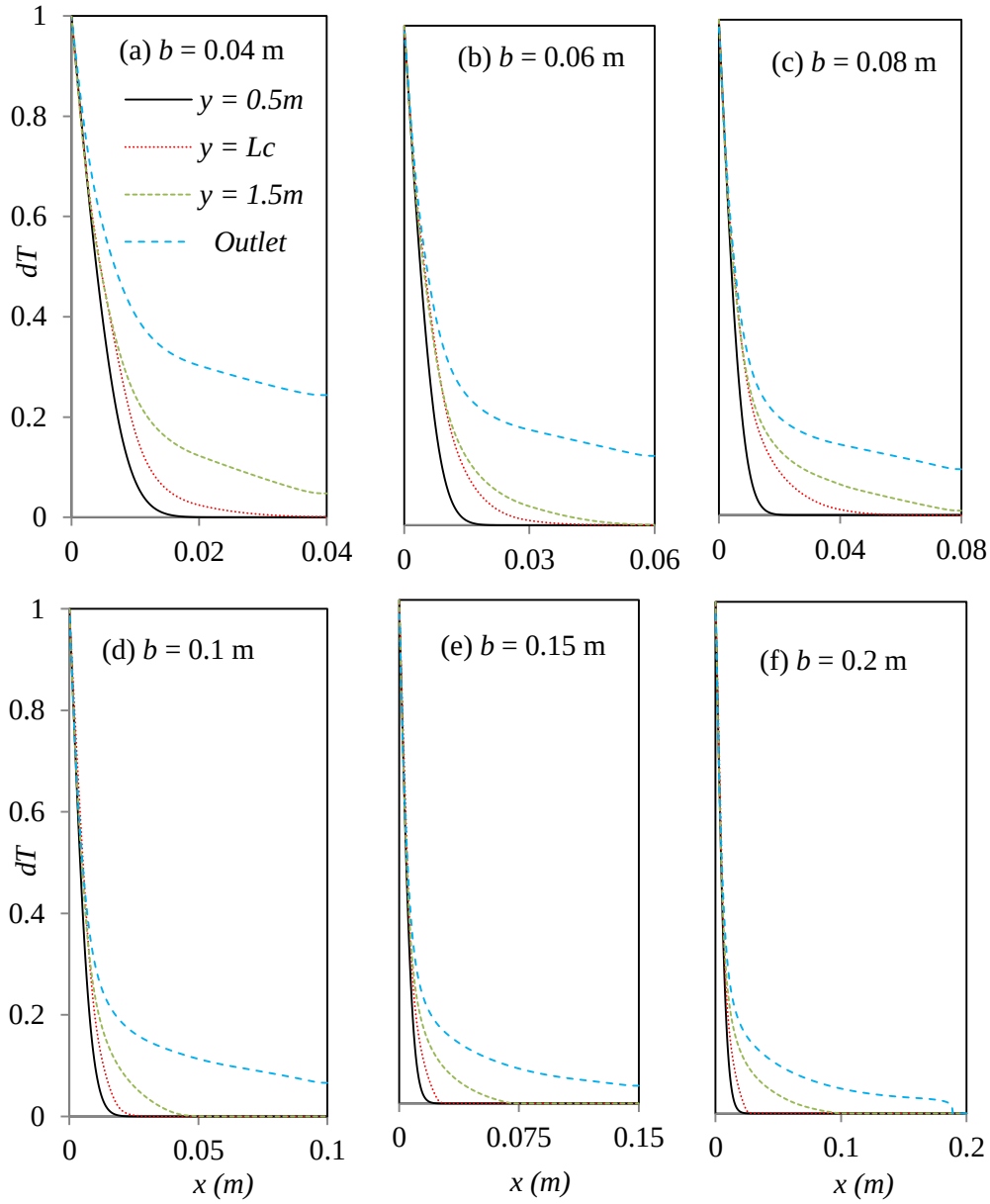

Figure 5. 22 Distributions of the air temperature inside the channel at *Ta* = 15°C and *Tp* =70°C.

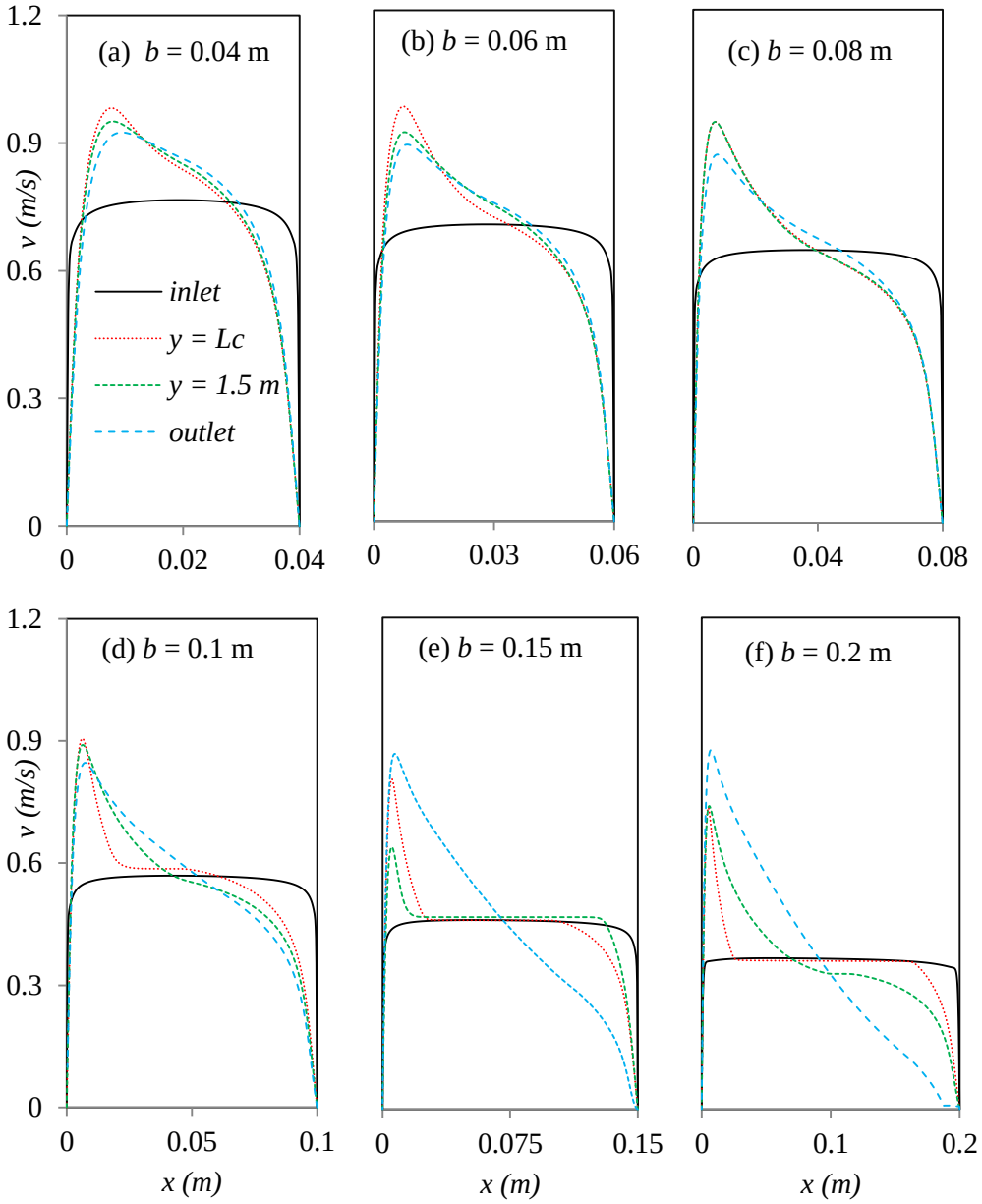

Figure 5. 23 Distributions of the air velocity inside the channel at Ta = 15°C and Tp =70°C.

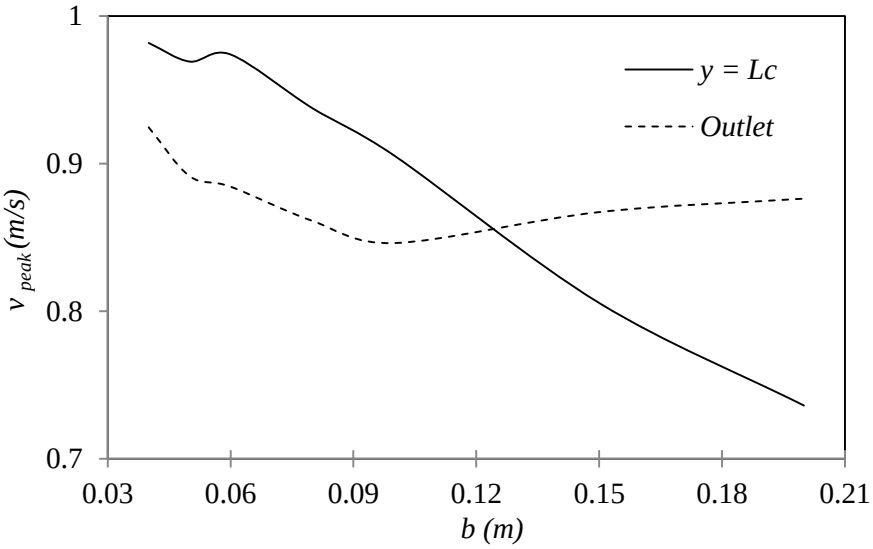

Figure 5. 24 Comparison between the velocity peaks at the critical distance and outlet.

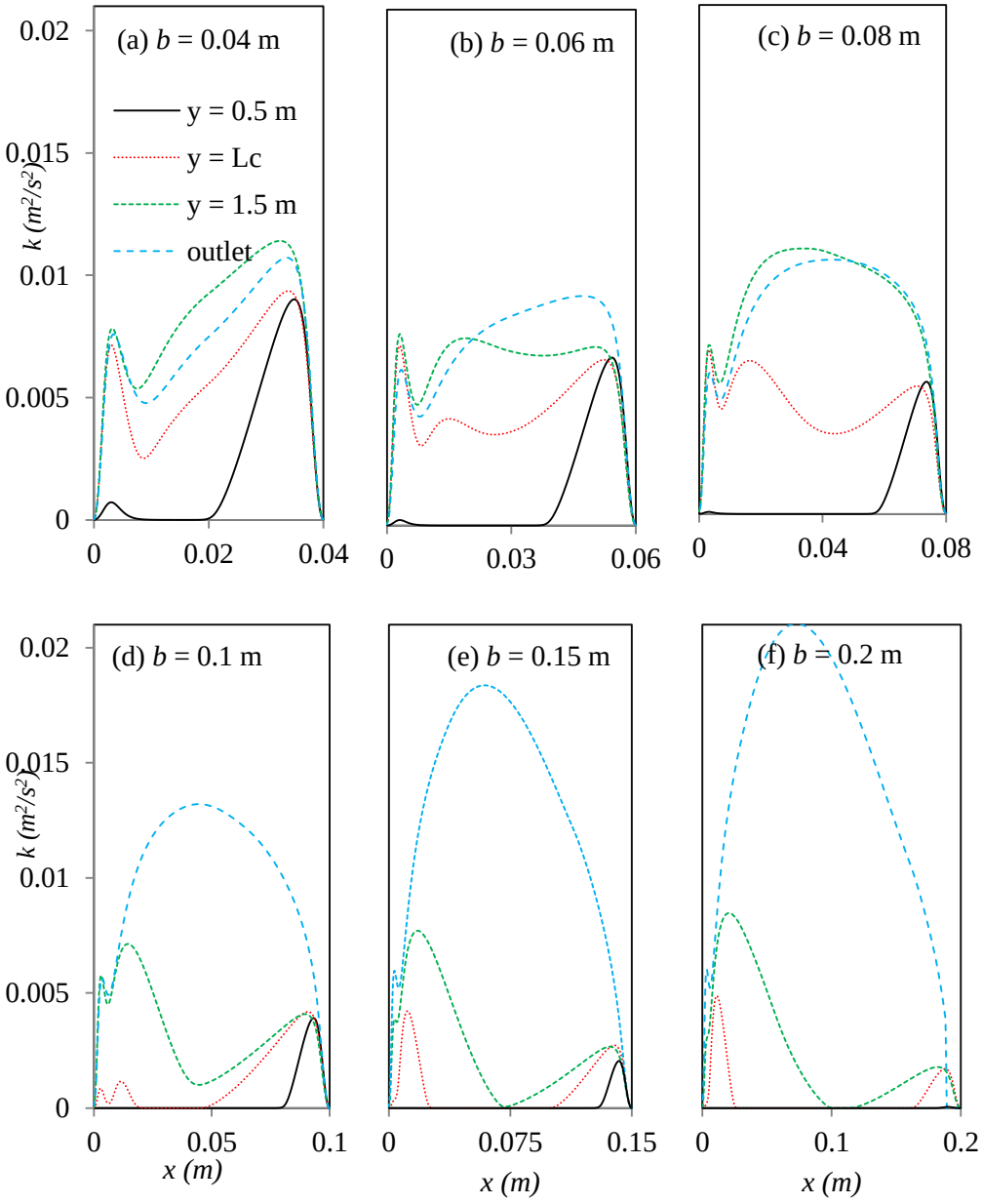

Figure 5. 25 Distributions of the turbulent kinetic energy inside the channel at *Ta* = 15°C and *Tp* =70°C.

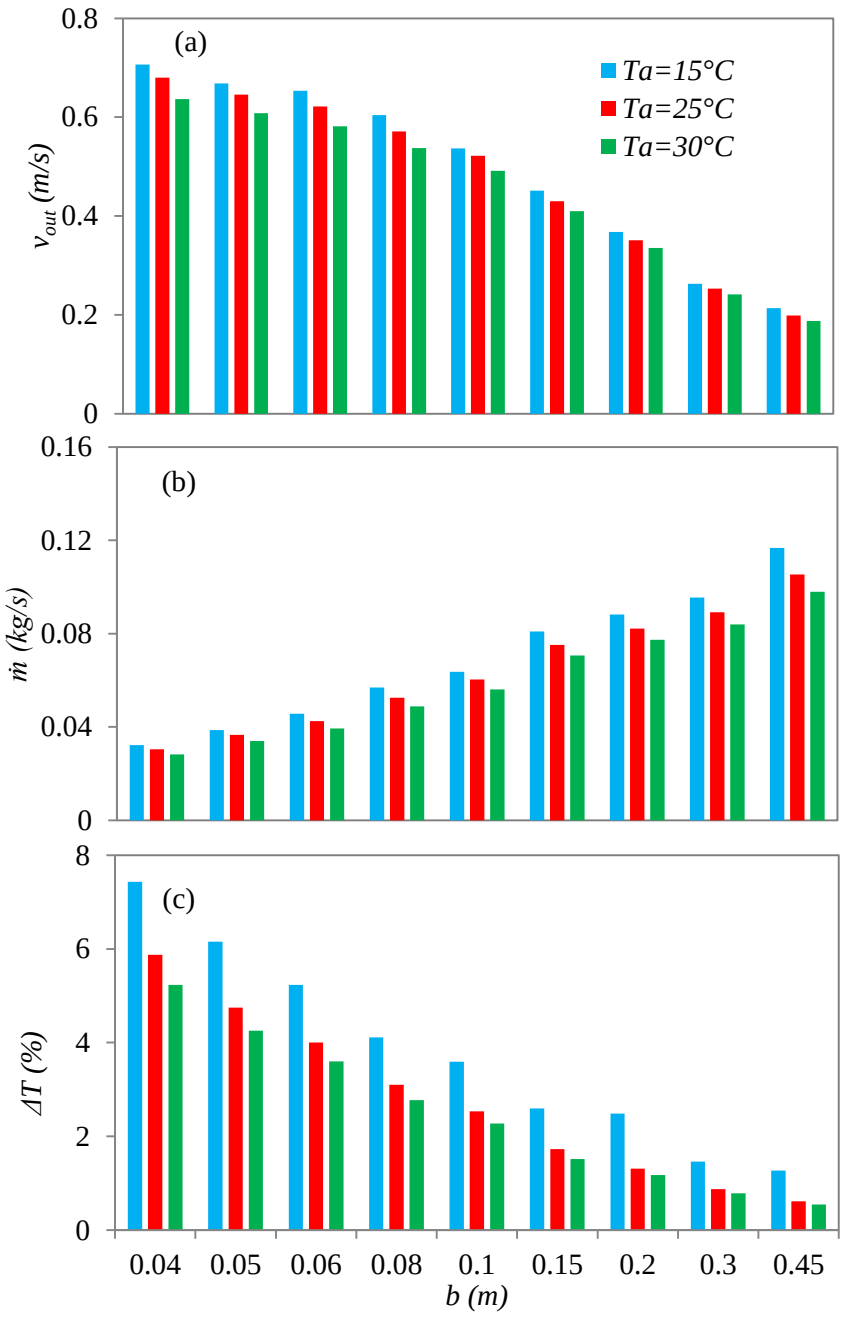

Figure 5. 26 Average outlet velocity (*a*), mass flow (*b*) and percentage of added temperature (c).

Chapter 6

Transition of free convection between two isothermal vertical plates

6.1. Introduction

Numerical results of the free convection flow inside a channel were reported in Chapter 5 where one of the heated plates in the channel was kept isothermal and the other one, placed opposite to it, was adiabatic. In this Chapter, development of natural convection flow between two isothermal plates is investigated with a particular focus on the flow transition. A comparison between the results obtained by the two flow conditions is given.

6.2. Model geometry and boundary conditions

The model geometry, which was described in Figure 5.1 in Chapter 5, is used in this Chapter. The numerical simulations remain to be two-dimensional free-convection and steady state, and air is chosen to be the test fluid. The same boundary conditions, which were reported in § 5.3 in Chapter 5, are employed at both the inlet and outlet sections. But the isothermal conditions for the plates of the channel are defined in Equations (6. 1, 6. 2) below. In this Chapter, the temperature (*Tp)* of the heated plate situated on the left hand side of the

channel will be fixed to 70°C, while the temperature of the plate opposite to it will be varied according to the boundary condition described in Equation(6. 2). Moreover, the air / ambient temperature (*Ta*) will also be fixed to 15°C.

$$T = Tp, \quad \text{for} \quad 0 \le y \le L, \qquad x = 0 \tag{6. 1}$$

$$T = Tp^*, \quad \text{for} \quad 0 \le y \le L, \qquad x = b \tag{6. 2}$$

6.3. Results and discussions

6.3.1. Flow feature: an overview

In order to determine the influence of the channel width on the development of the boundary layers of flow, variation of the axial profiles of temperature, turbulent kinetic energy and velocity across the channel width are presented in this section. The results are reported at different vertical locations: y = 0.5 m, 1.5 m, inlet and outlet, while the width (b) of the channel is varied from 0.04 m to 0.3 m.

In the first case the plate located at the right hand side of the channel is kept at a temperature Tp^* = 40°C and the inlet temperature is fixed at 15°C. Variation of the heated air temperature, determined by $dT = (T-Ta)/(Tp-Ta))$ and presented in Figure 6. 1, shows an increase in the temperature due to the air heated up by the heat transfer and convected downstream the channel. However, the outlet temperature of the channel drops as the width of the channel is increased due to the fact that the thermal boundary layer grows in a wider space available inside the channel. And the temperature difference between the outlet and the inlet becomes very small with an increase in the channel width as shown in Figure 6. 1 (e, f). However, when $b \ge 0.08$ m, the

temperature around the channel centreline (e.g. at $x = b/2$) and at the middle of the channel ($y = 1.5$ m) becomes equal to the ambient temperature as a result of the more space available for the development of flow.

Distribution of the turbulent kinetic energy is reported in Figure 6. 2. The magnitude of the turbulent kinetic energy at $b = 0.04$ m is larger compared to that found in the other cases except at the outlet section for $b = 0.3$ m, which is a result of the strong interaction of the two boundary layers developed in a relatively small space inside the channel. In all the cases, the peak of the turbulent kinetic energy near the right wall of the channel at $y = 0.5$ m is larger than that occurring at the left wall. The phenomena are explained by the fact that the magnitude of the velocity (shown in Figure 6. 3) adjacent to the right plate drops, which causes a flow deceleration and results in an increase in the turbulent kinetic energy near the right wall. But with an increase in the width of the channel, e. g. when $b \geq 0.1$ m, the effect of the buoyancy force on the left wall becomes more evident, where the turbulent kinetic energy reaches its peak near the left wall of the channel.

The variation of the velocity across the channel is shown in Figure 6. 3. As can be seen, with an increase in the channel width the mean velocity of air drops across the channel. The velocity profiles at the inlet section are more affected by the high viscous force compared to the buoyancy force near the heated plate, and the velocity profiles at the downstream ($0.5 \text{ m} \leq y \leq 1.5$ m) become flat in the middle of the channel.

Further to note in Figure 6. 3 (a-d) that the peak of the outlet velocity in a small width of the channel, e.g. when $0.04 \text{ m} \leq b \leq 0.1$ m, is found to be slightly lower than that at the middle of the channel (at $y = 1.5$ m). This is occurring due to the fact that the flow starts to development in the middle of the channel

and the buoyancy force accelerates the fluid inside the channel with an increase in the thickness of the two boundary layers in a small space, which leads to decrease the velocity at the outlet section.

6.3.2. Effect of boundary conditions

In the previous section typical results of the flow velocity and temperature have been presented and discussed, where the effect of the channel width has been investigated for a particularly chosen plate temperature, Tp^* = 40°C. This temperature will be changed to 70°C and the results will be compared with those obtained by Tp^* = 40°C as well as by the adiabatic case in Chapter 5. As already seen in Figure 6. 3, the velocity profile has been mostly affected by the buoyancy force, with a peak appeared near each heated plate.

In this section I will focus on the examination of the velocity peak at y = 1.5 m and 3 m. Only the velocity peak near the left heated wall is used, as in the adiabatic case we obtained a single velocity peak (e.g. see Figure 5. 24 in § 5.5 in Chapter 5). I also note that the value of the two velocity peaks on the two channel side in the isothermal case of Tp^* = 70°C is equal.

Figure 6. 4 shows the value of the peak velocity profiles and its location obtained by the three different boundary conditions: Tp^* = 40°C, Tp^* = 70°C and adiabatic. Figure 6. 4 (a) generally shows larger variation in the peak velocity at y = 1.5 m than that at the outlet section due to the flow developing in the middle of the channel. In the channel outlet, Figure 6. 4 (b) shows that the variation only appears for the small channel width when $b \leq 0.1$ m. In addition, the velocity peaks for the two isothermal cases are same because the flow becomes fully developed at the outlet section, but they are still larger than those for the adiabatic case in the range of channel width $b \geq 0.15$ m due to the

buoyancy force which is higher in the isothermal cases than that in the adiabatic case.

The location of the velocity peak is presented in Figure 6. 4 (c, d). It is clearly seen that the peak velocity of the flow appears to move towards the heated plate when the channel width is increased. In addition, the peak velocity in the adiabatic case becomes very close to the heated wall compared to that in the isothermal cases. However, the velocity peaks at y = 3.0, Figure 6. 4 (d), moves nearer the heated plate compared to y = 1.5 m in Figure 6. 4 (c) since the flow is fully developed at the outlet of the channel.

The air velocity and temperature at the outlet are summarised in Figure 6. 5. In order to make a direct comparison of these with those obtained by the adiabatic case (§ 5.5 in Chapter 5), a percentage of increment is calculated by using $dv_{inc} = (v_{out\ iso} - v_{out\ adi})/(v_{out\ adi})*100$ for the velocity magnitude. The same approach is used for the determination of temperature increment. As can now be seen in Figure 6. 5 (a) that the outlet velocity grows with the channel width for the isothermal cases as a result of an increase in the buoyancy force in the convection flow. But, after reaching a peak at around b = 0.3 m, the velocity drops for the large width of the channel. The air velocity has an impact on the flow temperature and the results plotted in Figure 6. 5 (b) show an opposite effect, i.e. the added heated temperature drops with the channel width to a minimum followed by an increase for the large width.

6.3.3. Boundary layer growth: isothermal vs. adiabatic cases

Effect of the width of the channel on the growth of the boundary layers along the flow is summarised here with the distributions of the maximum velocity, turbulent kinetic energy and turbulent intensity determined by using $f_{\max}(y) = \underset{x\min \le x \le x\max}{Max} f(x,y)$, where f is a generic variable, and plotted in Figure 6. 6.Comparison is made between the results of the adiabatic and isothermal cases, and the temperature of the plate on the right hand side of the channel for the isothermal case is kept at $Tp_* = 40°C$.

The results presented in Figure 6. 6 indicate that the velocity magnitude in the isothermal case is generally higher than that of the adiabatic case due to the increase in the buoyancy force mentioned earlier. And, particularly, in the isothermal cases for b = 0.04 m to 0.10 m, the velocity distribution approximately becomes constant as shown in Figure 6. 6 (a) when $y \leq 1.5$ m. While, in the adiabatic cases the distribution of the velocity show a magnitude drop from the peak towards the downward. However, for the rest of channel width e.g. b = 0.15 m to 0.45 m, in Figure 6. 6 (b), both the cases show a similar behaviour with a shift in the velocity profile towards the downstream for the isothermal cases. In both the cases the maximum velocity at the outlet section has an approximately same magnitude which is ≈ 0.8 m/s.

Figure 6. 6 (c-d) presents the maximum turbulent kinetic energy inside the channel. For a small width of the channel, e.g. when b = 0.04 m and 0.06 m, the kinetic energy in the isothermal case is larger than that of the adiabatic case, which is expected as in the isothermal case there is a strong interaction occurring between the two boundary layers within a relatively small distance.

However for $b \geq 0.10$ m, the distribution of the kinetic energy in the adiabatic case is larger than that of the isothermal case due to the fact that a single boundary layer which grows in the adiabatic case gets enough space in the channel to develop fully, whereas in the isothermal case an interaction between the two boundary layers occurs.

The distribution of the turbulent intensity presented in Figure 6. 6 (e, f) has a similar profile as the turbulent kinetic energy. When $b \geq 0.1$ m, the turbulent intensity in the isothermal case is smaller than that of the adiabatic case. The turbulent intensity also increases sharply towards the downstream, especially at the outlet of the channel, due to the turbulent nature of the flow occurring at the downstream regime.

Contours of the turbulent kinetic energy, turbulent intensity and velocity inside the channel are shown in Figure 6. 7 (A), (B) and (C) respectively for the different channel width: 0.05 m, 0.1 m, 0.15 m, 0.2 m, 0.3 m and 0.45 m. To make a direct comparison between the adiabatic and isothermal cases the contours are plotted pairwise in frames (a, c, e, g, i, k) for the adiabatic case and in (b, d, f, h, j, l) for the isothermal case. In general, the contour plots show that the maximum turbulent kinetic energy and its turbulent intensity in the isothermal cases dropped by 41% and 20% respectively compared to the adiabatic cases. This is related to the interaction occurring between the two boundary layers in the isothermal case, clearly seen in frames (h, j and l) when $b \geq 0.2$ m. While in the adiabatic case only one boundary layer grows on the left hand side with an ample space to fully develop as seen in frames (i) and (k).

6.3.4. Flow transition

As seen in Figure 6. 7 (A), (B) and (C) the boundary layer in the isothermal cases grows on the both sides of the channel and a separation / transition occurs from the laminar to turbulent stage towards the channel downstream. In this section the transition behaviour will be examined by taking into account of the distribution of the maximum velocity on the left ($0 \leq x \leq b/2$) and right ($b/2 \leq x \leq b$) hand sides of the channel.

Figure 6. 8 (a) and (b) show the maximum velocity field obtained in the left and right side domains, where the temperature of the heated plates is kept as 70°C and 40°C respectively. The maximum velocity on both sides of the channel is same at the upstream near the inlet where the effect of the buoyancy force on the velocity field is expected to be similar.

As the distribution of the peak velocity is considered to be a starting point of the flow transition, Figure 6. 8 (a) shows that the transition point of the flow developing in the left side wall for the cases $b \leq 0.10$ m appears to be within the range $1.0 \leq L_c \leq 1.8$ m. However, the distribution of the velocity on the right side has a different behaviour, which continues to drop after a slight increase near the inlet when $b \leq 0.1$ m due to the strong interaction occurred between the two boundary layers, already explained in Figure 6. 7 (b-d). These results are unable to determine the transition point on the right side and it is still more affected by the left side.

However, Figure 6. 8 (b) shows that the velocity in the right wall increases to a peak at the transition point when $b \geq 0.15$ m because there is enough space available for the development the flow. However, the location of the flow transition point on the right side is higher than that on the left side,

as the thickness of the boundary layer on the right side is small and the flow becomes more stable and causes a delay in the transition process.

Finally, the transition of the flow boundary layers on the left and right sides of the channel are summarised in Figure 6. 9 in terms of their critical distance obtained from the velocity results shown in Figure 6. 8. Comparison of the two isothermal and the adiabatic cases is also given.

As can be noticed in Figure 6. 8 (a) that it is very difficult to estimate the transition point on the right side for the channel with a small width e.g. when $b \leq 0.08$ m due to the strong interaction between the two boundary layers (Figure 6. 7 (b)). However, with an increase in the channel width, e.g. when $b \geq 0.1$ m, the transition on the right side appears late compared to that in the left side; this is expected as the temperature in the right side is lower than that of the left side. Also, when $Tp^* = 70°C$ both the sides of the channel are kept at under the same isothermal condition, and that is why only the results obtained from the right side of the channel are reported in the comparison. With an increase in the channel temperature the flow inside the channel becomes unstable early as the critical distance drops and therefore an early transition occurs. Particularly, for a relatively small channel width, e.g. when $b = 0.04$ m, the transition of the flow appears to be very quick.

6.4. Conclusion

Effects of temperature of the parallel-plate channel and its width on the developing free-convection flow have been investigated numerically under various operating and geometrical conditions. The two vertical plates of the channel are kept under the isothermal conditions, and the distance separating

the two parallel plates is systematically reduced from 0. 45 m to 0.04 m. Comparison is made with the adiabatic results presented in the previous Chapter.

The results indicated that with an increase in the channel width, the location of the velocity peaks moved very close to the heated plate. This was particularly noticeable for the cases with relatively small channel width.

At the transition stage, the results show that flow transition in the adiabatic case occurs early compared to the isothermal cases due to the single boundary layer developed along the heated plate. On the other hand, late transition occurs when the two heated plates are kept under the isothermal condition. Moreover, with an increase in the average channel temperature in the isothermal cases, the boundary layer on each side of the channel grows early and the flow becomes unstable due to the consequences of the shorter laminar region and the turbulent flow which develops early.

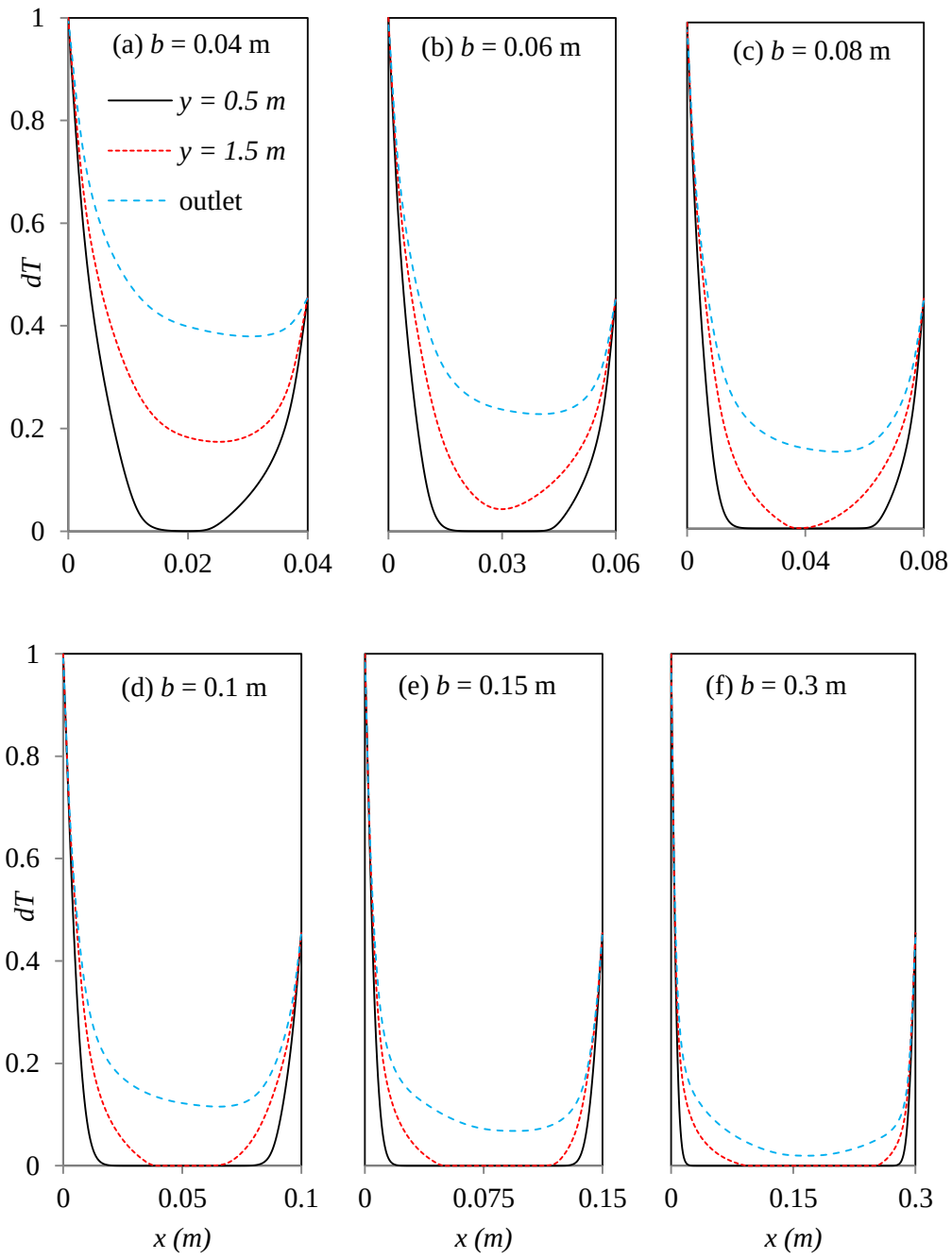

Figure 6. 1 Effects of the width on the temperature at Tp^* = 40°C.

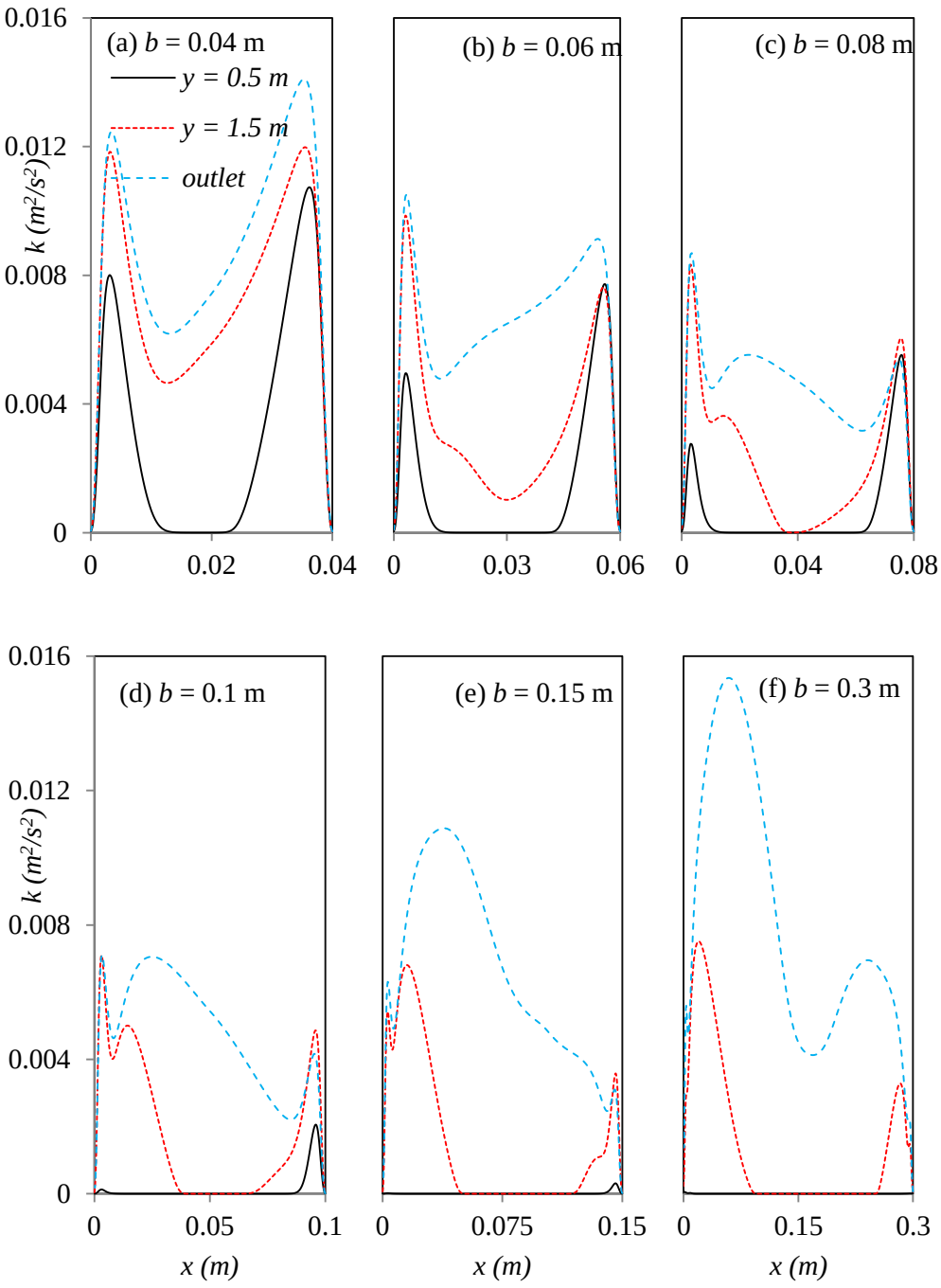

Figure 6. 2 Effects of the width on the turbulent kinetic energy at Tp^* = 40°C.

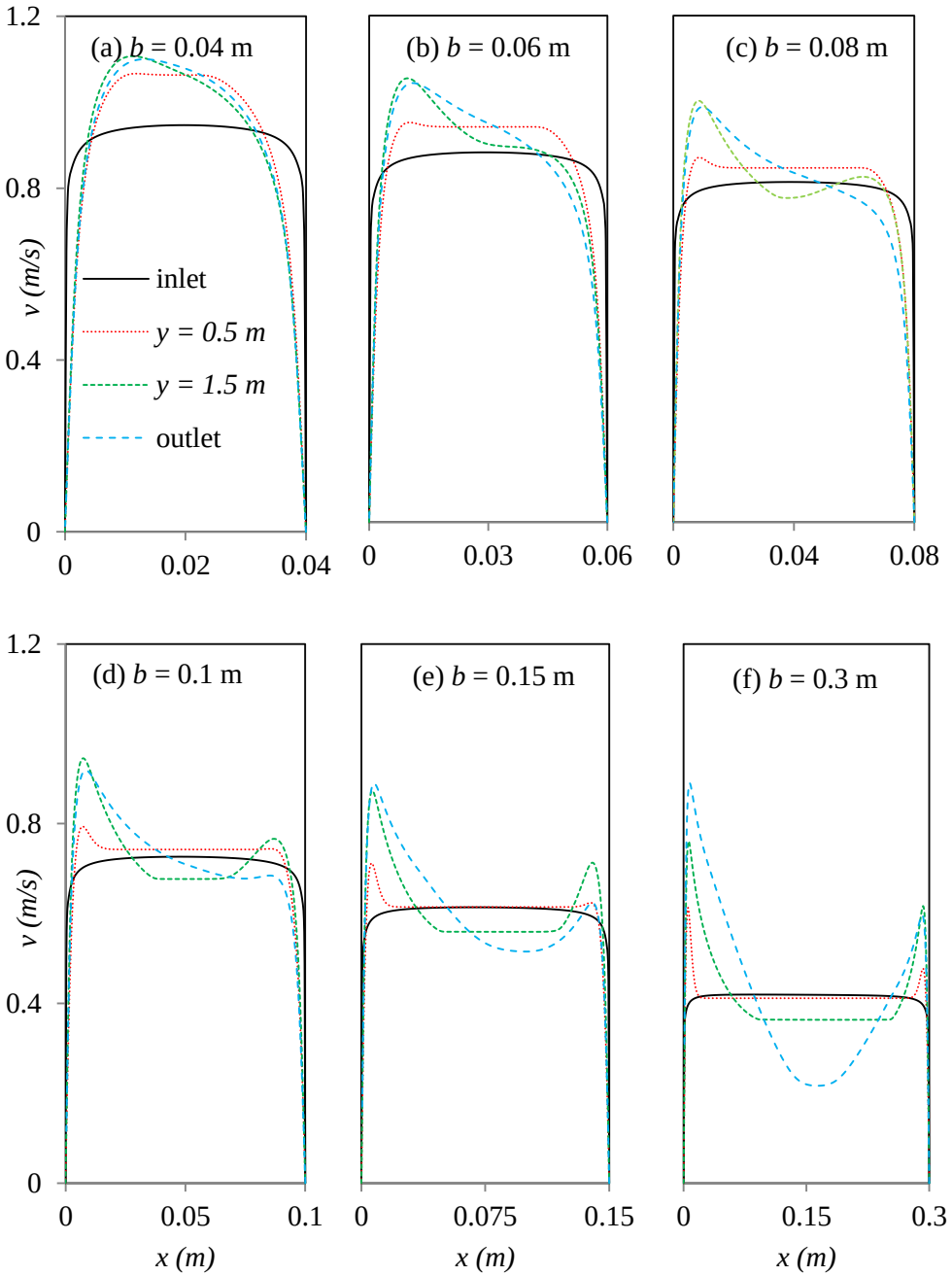

Figure 6. 3 Effects of the width on the velocity of air at Tp^* = 40°C.

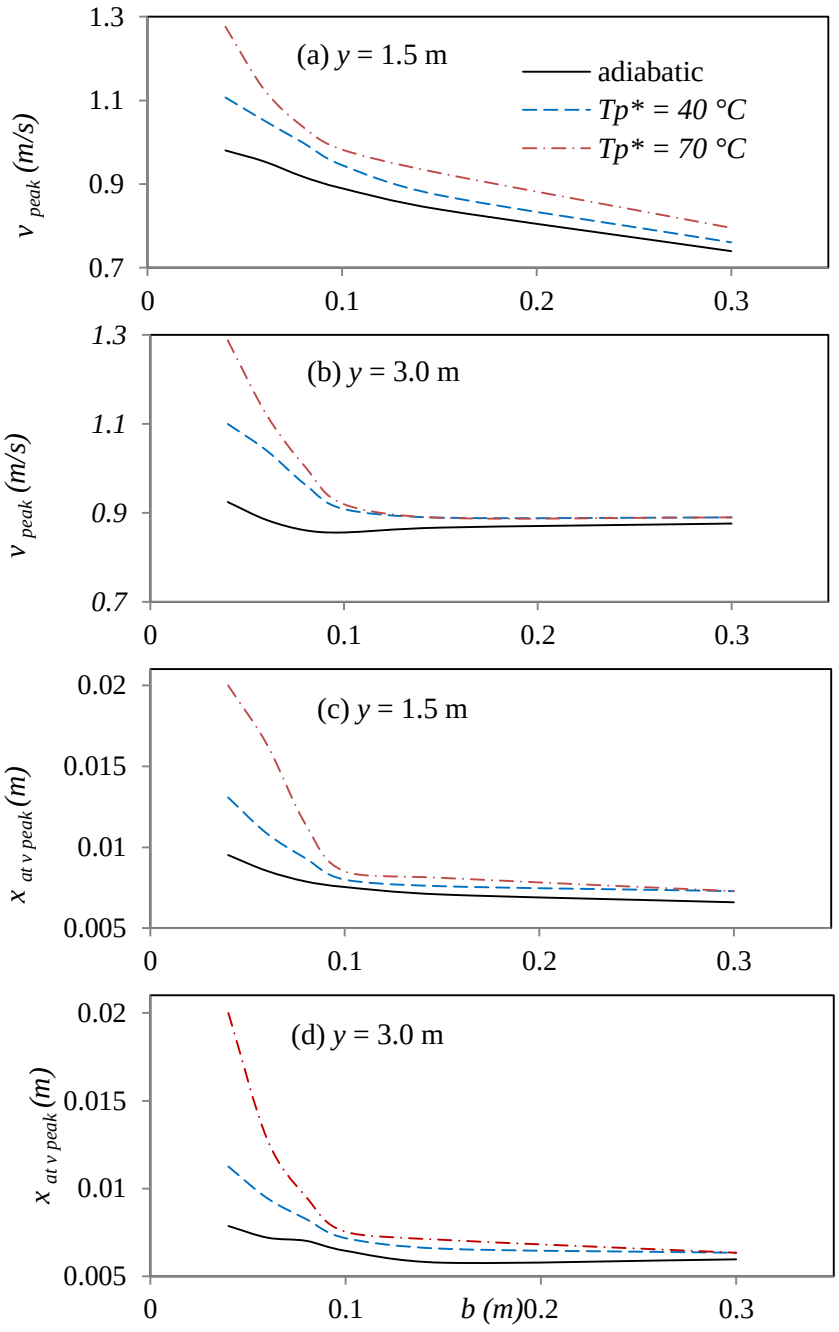

Figure 6. 4 The peak velocity (a, b) and its location (c, d).

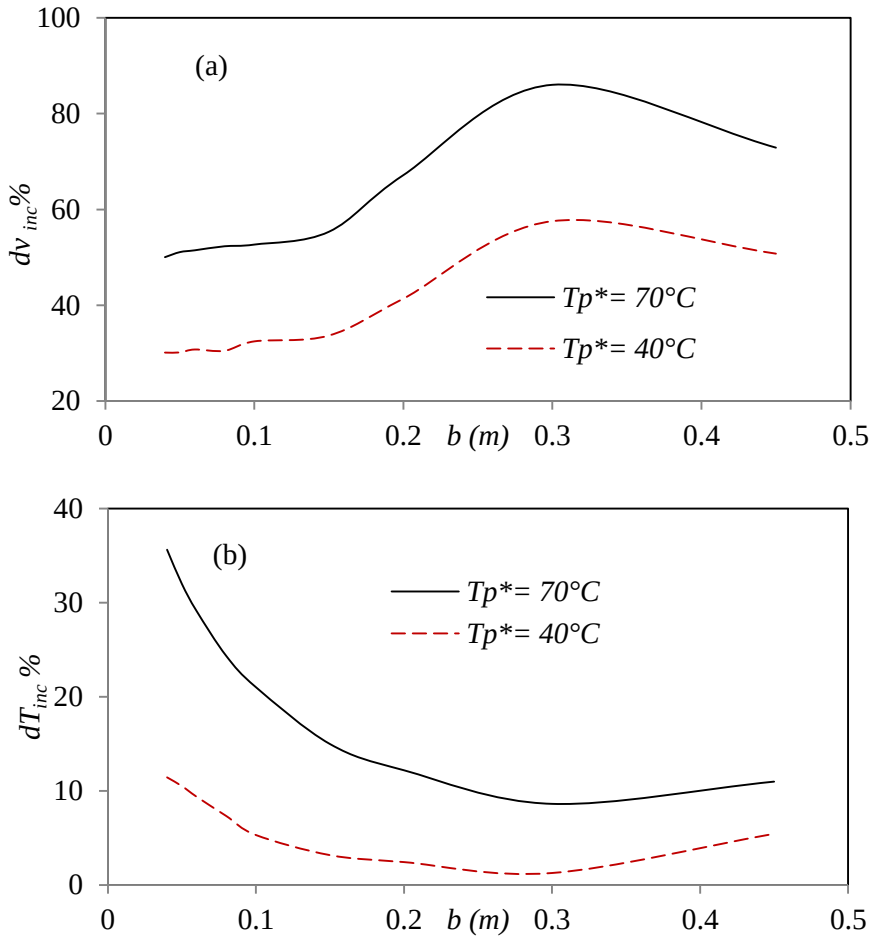

Figure 6. 5 Increment of velocity (a) and temperature (b) at the outlet.

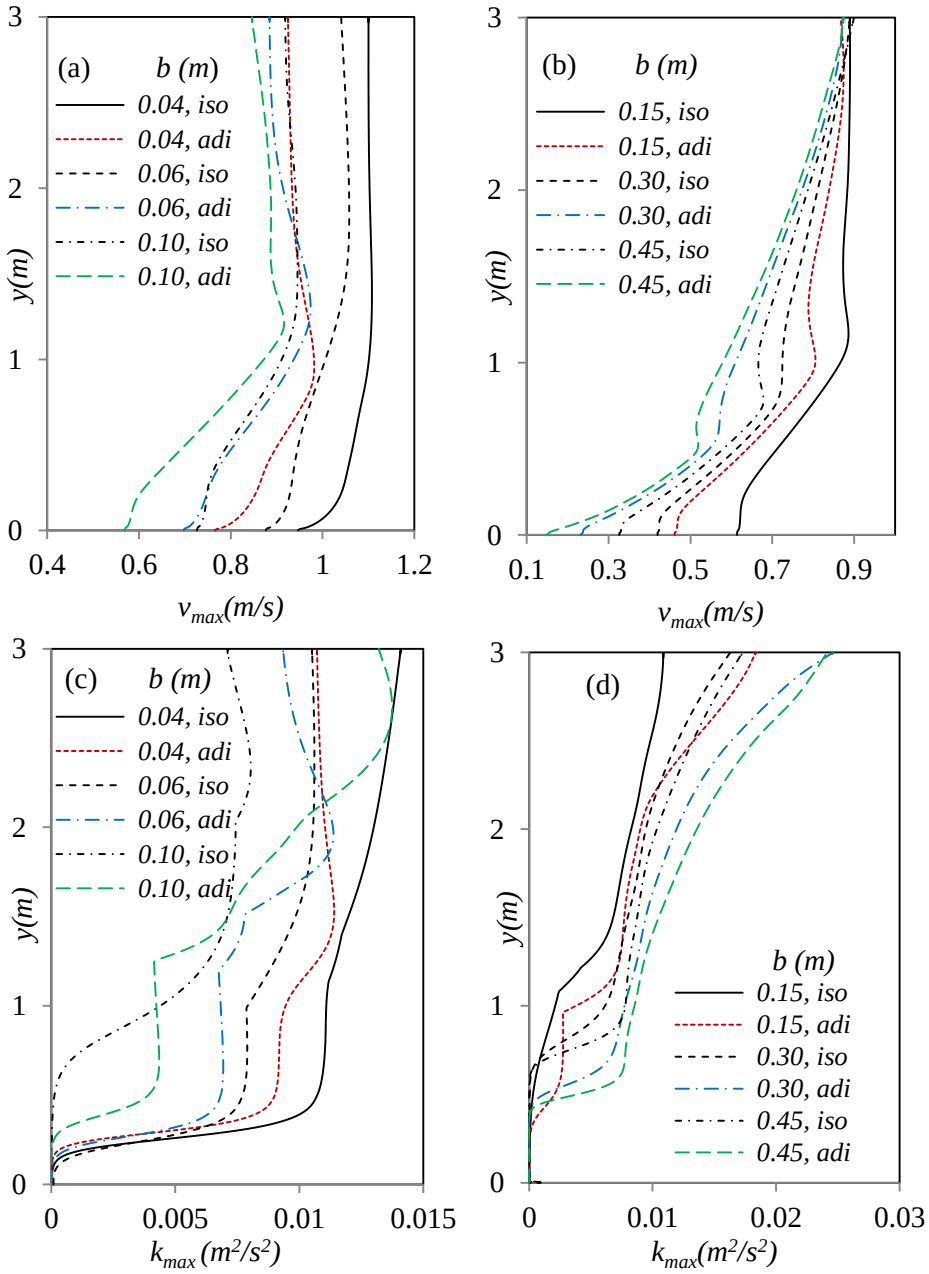

Figure 6. 6 Comparison of the maximum velocity (a, b), kinetic energy (c, d) and turbulent intensity (e, f) between the isothermal (iso) and adiabatic (adi) cases.

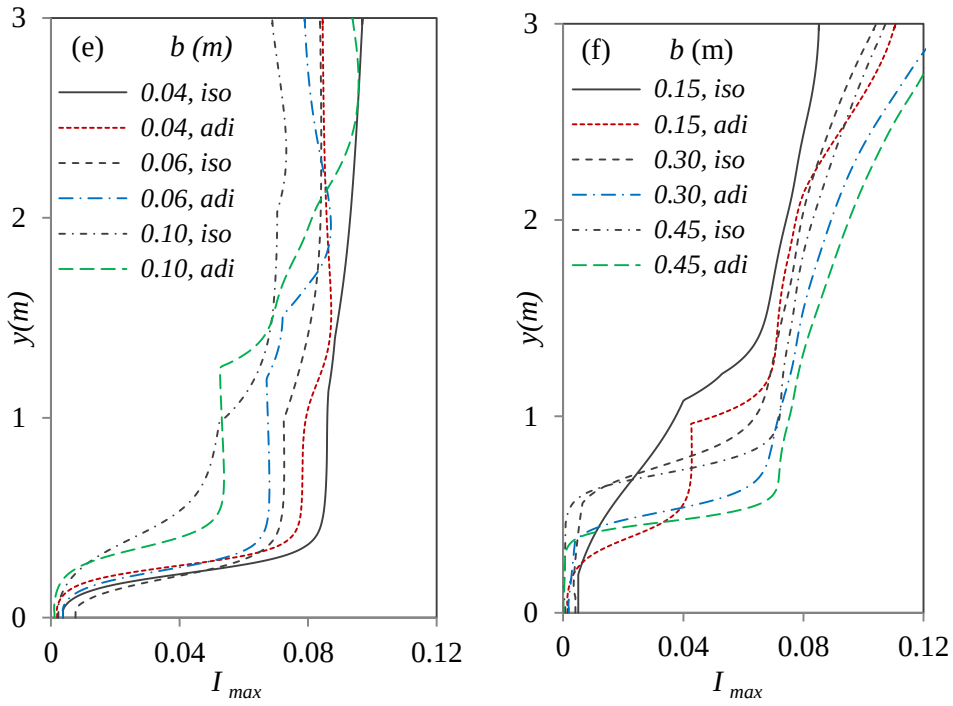

Figure 6.6 Caption continued.

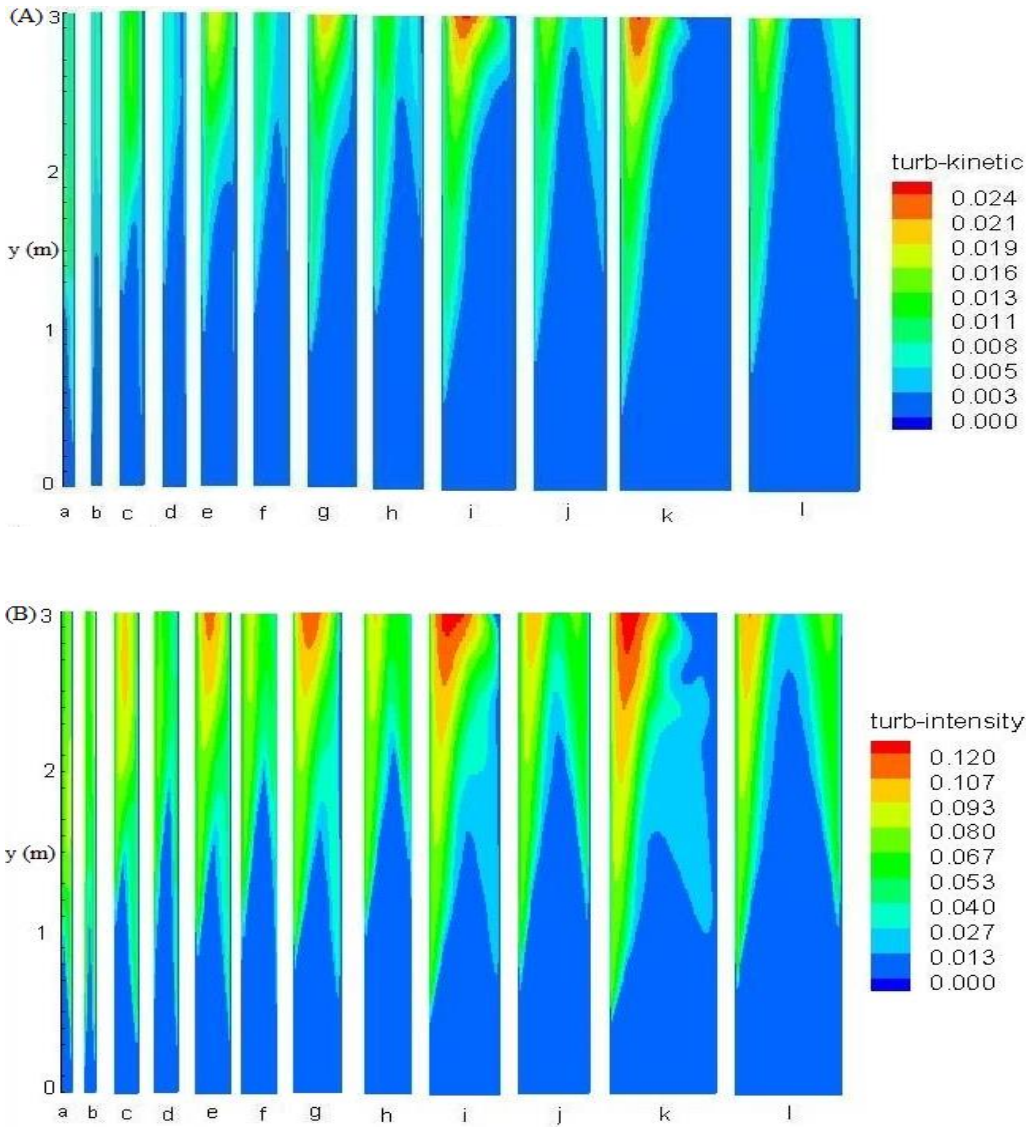

Figure 6. 7 Contours of the turbulent kinetic energy (A), turbulent intensity (B) and velocity (C) at various channel width. Note the adiabatic results are in frames (a, c, e, g, i, k) while the isothermal are in (b, d, f, h, j, l).

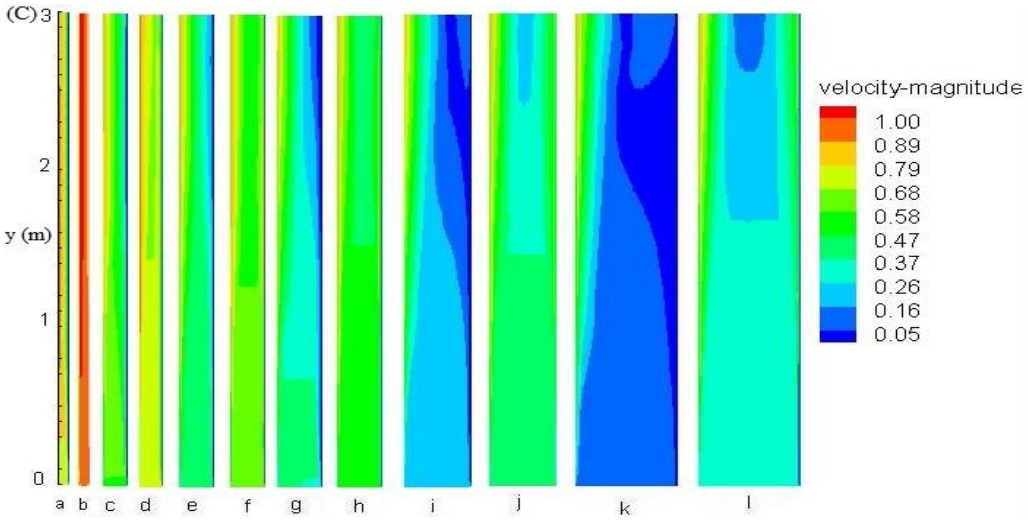

Figure 6.7 Caption continued.

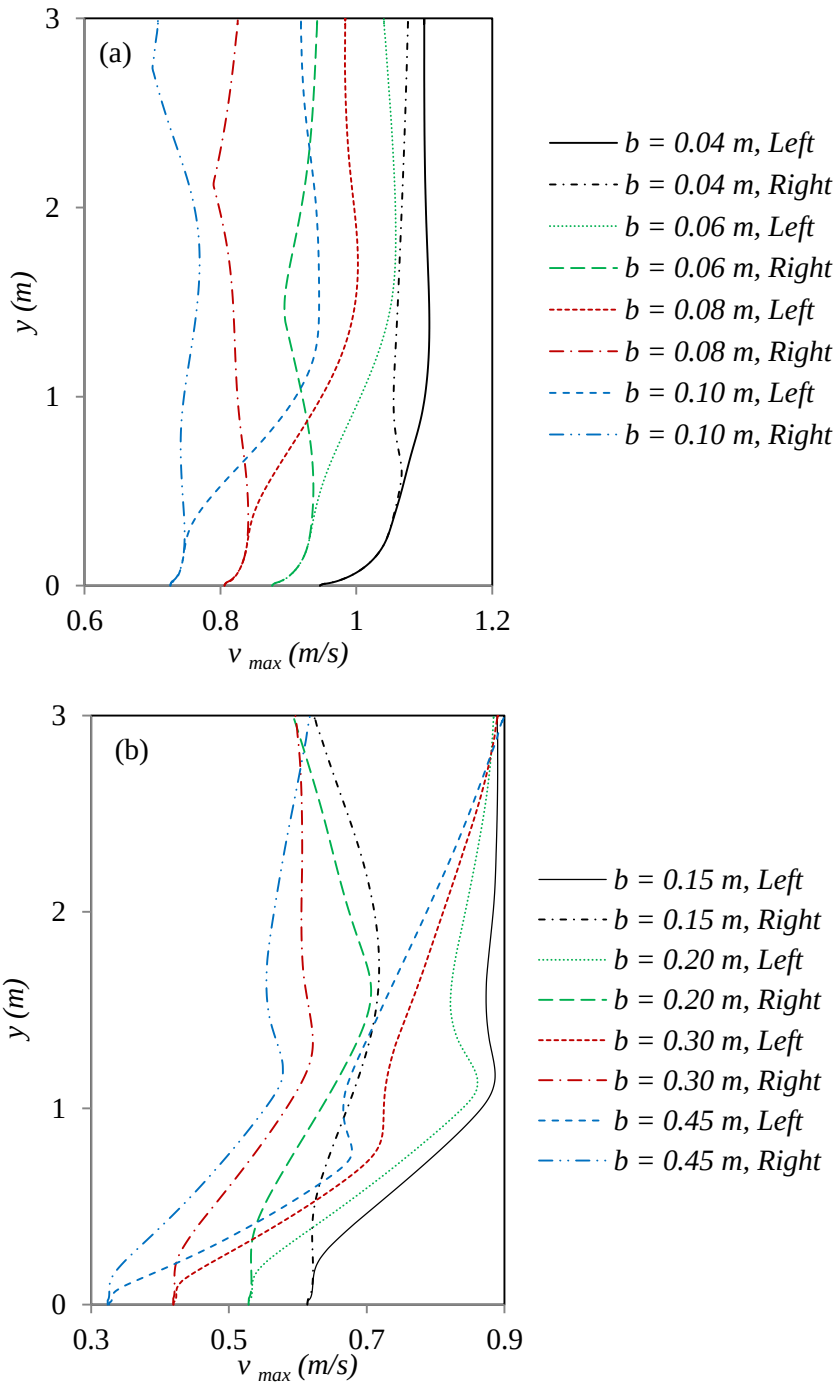

Figure 6. 8 Comparison of the velocity predicted on the left and right sides of the channel at Tp_{*} = 40°C.

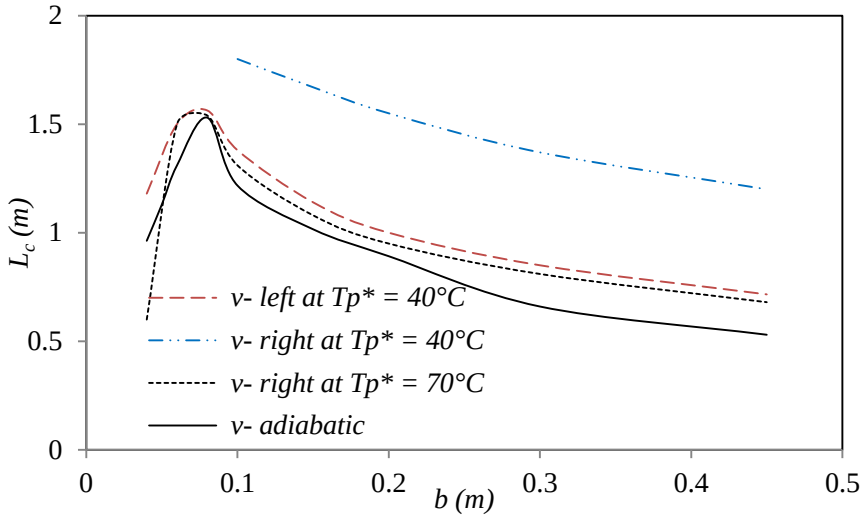

Figure 6. 9 Critical distance of the flow transtion inside the channel.

Chapter 7

Transition of free convection flow inside an inclined heated channel facing downward

7.1. Introduction

Transition of free convection flow in an inclined parallel walled channel has been investigated numerically by employing Realizable k-ε turbulent model. Particular attention is paid on how the inclination angle and width of the channel affect the transition process of the flow developing in the channel. The upper plate of the channel is heated isothermally and facing downward, while the lower one is kept under the adiabatic condition. The inclination angle of the channel is varied from 0° to 85° with respect to its vertical position while the distance separating the two plates is systematically reduced from 0.45 m to 0.06 m. Distributions of velocity, turbulent kinetic energy and local heat flux are presented to examine the critical distance and the results obtained show good agreement with experimental data available in the literature.

7.2. Model geometry and boundary conditions

The channel is formed by two inclined plates each with length L, and the distance between the plates is denoted by b. The wall on the top side is isothermal and heated below, while the other one is adiabatic. The numerical simulation is considered to be two-dimensional free convection and steady state. Air is chosen to be the test fluid.

The model geometry along with the Cartesian coordinate system is shown in Figure 7. 1, where the conservation equations of mass, momentum and energy for a two-dimensional incompressible fluid flow are solved.

A no slip boundary condition is imposed on the velocity components at each wall for which set $u_i = 0$. The thermal boundary conditions for the heated and the adiabatic plate are defined as $T = Tp$ at $x = 0$ and $\partial T/\partial x = 0$ at $x = b$ respectively. Moreover, the turbulent kinetic energy vanishes at the walls so that set $k = 0$. Since distributions of the characteristics of the flow have large gradient near the walls, an enhanced wall function is also used in the wall boundary. The inlet boundary is subject to the ambient conditions, while at the outlet the static gauge pressure is set to zero.

7.3. Grid resolution test

The numerical methods used to solve the governing equations have already been described in § 5.5.1 in Chapter 5 and validated with suitable experimental data in a vertical heated channel. Moreover, an in-depth investigation on the grid resolution has also been carried out by using six different grids (22 × 220, 30 × 370, 120 × 370, 200 × 370, 300 × 370 and 200 × 400) with a fine

resolution of mesh clustered near the inlet and the channel walls. The variation seen in the simulation results predicted by the last four grids is very small and almost negligible. The same agreement is received when I have tested these in the channel at an orientation angle of 45° shown in Figure 7. 2. Therefore, as in the previous study, the grid size of 200 × 370 is chosen to avoid any undesirable discrepancies in the numerical results and at the same time to save the computational time to perform all the numerical simulations.

7.4. Results and discussions

7.4.1. Effect of width and angle of the channel on the outlet parameters

Outlet velocity, temperature and average heat transfer are presented in this section to investigate the effects of the width and inclination angle of the channel on these parameters. The upper plate is kept isothermal at 70°C when the lower one is adiabatic, and the temperature of air is 15°C. The effect of the channel width (b) and its inclination (θ) is first shown in Figure 7. 3 on the normalised outlet temperature derived as $dT_{inc} = (T_{out}-T_{in})/T_{in} \times 100$. In general, the results show that the outlet temperature increases when the width of the channel is gradually reduced.

But, the effect of the inclination angle is not straightforward and the temperature seems to be more influenced by the small width length of the channel (e.g. when $b \leq 0.15$ m) when it is particularly positioned at an angle greater than 60°. The gradual drop in the outlet temperature for the one-plate case with the angle indicates the effects of the free boundary which is subject to the ambient conditions. While, for the channel flow cases the adiabatic wall influences the development of the thermal boundary layers inside the channels.

The outlet velocity in Figure 7. 4 also shows a general trend i.e. it increases as b is reduced. But, in contrast to the temperature, the flow velocity is reduced when the channel is moved from its vertical position due to an increase in the velocity component (u) acting in the horizontal direction (x) of the channel which in turn causes a drawback to the flow travelling downstream of the channel. In terms of quantifying the magnitude of the velocity drop, the channel with b = 0.10 m is selected, and we find that the velocity drops by about 20% from 10° to 50°, while it is about 50% from 50° to 80°. Therefore, the effect on the velocity is pronounced when the channel orientation is close to the horizontal position due to strong diffusion caused by the other velocity component as highlighted above.

Average heat transfer can be defined as $h = qp/(Tp - Ta)$ where the qp is heat flux of the plate, the results are presented in Figure 7. 5 in a bid to characterise the effects on the process of heat transfer occurring in the channels with varying both the width and orientation angle. Heat transfer in the vertical position is highest in magnitude compared to that in other inclined positions, and the effect at higher inclination angles appears to be strong. This phenomenon is explained by the fact that when the channel is inclined at an angle to the vertical position, the buoyancy component exists in the direction into the heated surface as $g\rho\Delta V sin\theta$ where ΔV is the volume of the fluid displaced. The buoyancy component causes the pressure at the heated plate to be higher than that in the fluid which further causes an outward flow away from the heated surface.

The thermal boundary layer growth is then affected by this process, and as a result the heat transfer between the plates and fluid falls. While in the vertical case the buoyancy component acts only in the flow direction (as given by $g\rho\Delta V$), and the heat transfer is therefore predicted to be maximum. However,

an interesting but rather complex effect is found while varying the width *b*. Starting from the single plate case, when the width of the channel is reduced to 0.3 m, the average heat transfer increases moderately. But, a sudden drop is predicted for $b = 0.2$ m and the heat transfer increases again when the width is reduced to 0.15m followed by a systematic growth as *b* is reduced further. This variation is clearly seen in Figure 7. 6 where the same results are plotted but against the channel width.

All the curves show a sudden deep near at $b = 0.2$ m. It is understood from this phenomenon that when the width of the channel $b \leq 0.2$ m, the heat transfer coefficient is affected mainly by the conduction than the convection due to the constraint on the flow developing inside the channel. Therefore, the average heat transfer decreases to a minimum point at $b = 0.2$. On the other hand, when the channel width is increased, the heat transfer coefficient is more affected by the free convection and increases with the width of the channel until the effect of the presence of the adiabatic plate disappears slowly.

We also note that the behaviour reported in the heat transfer coefficient shows a very good agreement qualitatively with the experimental data of Onur et al. [1997] and Baskaya et al. [1999] for a different geometry. Onur et al. [1997] explained that the fluid largely remains motionless due to frictional forces retarding the development of natural convection when the plate spacing is relative small. Heat transfer decreases with the plate spacing to a minimum until the frictional losses is minimised. However, a further increase in the spacing causes acceleration in fluid motion and, as a result of this the rate of heat transfer increases.

7.4.2. Effect of orientation angle on the transition stage

In this section, transition behaviour of the air flow is presented with the channel inclination for the width of b = 0.08 m and 0.10 m. The first set of results pertains to present the distributions of the maximum velocity and kinetic energy in Figure 7. 7 determined by using $f_{\max}(y) = \underset{x\min \le x \le x\max}{Max} f(x,y)$, where f is a generic function, and plotted along the vertical axis y. Figure 7. 7 (a-c) show typical results of the velocity profiles along the channel, e.g. the velocity gradually grows from the inlet and reaches its maximum at the point where the flow transition occurs. However, the velocity magnitude drops slightly after the transition and becomes almost steady towards the outlet. Particularly, when $\theta \geq 30°$ the velocity profiles increase slightly in the region close to the outlet which has a good agreement with the results of Said et al. (2005b).

The turbulent kinetic energy (Figure 7. 7(b-d)), on the other hand, has zero values within the laminar region of the flow, which then grows rapidly from a location where the process of transition begins with a steady growth within the whole transition region. A sharp increase is followed in the most cases within the region of the turbulent flow. In case of b = 0.08 m and when $\theta \leq 50°$ the kinetic turbulence energy grows slightly after the transition point and then increases sharply in the rest of the region as seen in Figure 7. 7(b). This is further clarified in the contour plots, Figure 7. 8 (A-B), where the growth of the turbulent kinetic energy inside the channel is presented. As seen, the turbulent kinetic energy grows early on the adiabatic plate, particularly when the channel width is reduced. The reason of this phenomenon is that, as the velocity is accelerated near the heated plate, the velocity near the adiabatic plate should be

decelerated which causes increase in the turbulent kinetic energy near the adiabatic surface, as shown in Figure 7. 9. However as the width of the channel is increased, the turbulent kinetic energy near the adiabatic plate is attenuated because the deceleration of the velocity is not so distinguished as it is becomes in wide range of the channel. These numerical results are in agreement with the experimental data of Katoh et al. (1991) and Yilmaz and Fraser [2007].

The second set of result pertains to the distribution of local heat flux along the heated plate for all the inclination angles and b = 0.08 and 0.10 m. Figure 7. 10 generally shows that the local heat transfer is much higher at the edge of the channel near the inlet than the downstream due to a larger temperature difference between the heated plate and the air flow with a thinner thermal boundary layer developing upstream than that at the downstream. However, the thermal boundary layer thickens along the heated plate which causes a rapid decrease in the local heat transfer until it again starts to grow slowly after the transition stage. In particularly, the growth of the local heat transfer after the transition becomes less sharp at b = 0.80 m compared to b = 0.10 m due to the possible fact that there is not enough space available for the thermal boundary layer to fully develop in the channel.

Moreover, a systematic increase in the tilting angle causes the transition point to move further downstream; as a result the turbulent region at a particularly higher orientation angle becomes relatively short. In addition, the local heat transfer just prior to the outlet section increases slightly for $\theta \geq 30°$ due to increase seen in the velocity near the outlet (Figure 7. 7).

Since the peak of the velocity distributions from the heated plate can be considered to be a starting point of the transition stage and according to Katoh et al. [1991] the location of a minimum point of the local heat flux should also

correspond to the transition point, theses parameters are used to predict the critical distance (L_c) of the flow in the channel and are summarised in Figure 7. 11 (a-b) respectively, for b = 0.08 m and 0.10 m.

In general, as the inclination of the channel is increased, the critical distance predicted by all the three parameters increases, indicating a late transition due to the stable convection flow inside the channel. Notably, further the channel from the vertical position, the predicted critical distances by the velocity and turbulent kinetic energy are very close to each other with a small width e.g. b = 0.08 m Figure 7. 11 (a), the critical distance predicted by the heat flux is less than the other two parameters when $\theta \leq 50°$, and it is approximately half when $\theta \leq 10°$. But, when the angle is increased the critical distance increases sharply and shows an over prediction with those obtained by the velocity and turbulent kinetic energy when $\theta \leq 70°$.

The structure of the flow within the boundary layer and the behaviour of the flow near the surface are very important factors affecting the transport of the energy and mass in the transition stage. That is why, the critical distance indicating the transition of the flow was estimated by the velocity, kinetic energy and heat flux plate Figure 7. 11 . In order to understand the effect of the angle of the plate on the distribution of the velocity and the temperature of air flow in Figure 7. 12 and Figure 7. 13, both of them are presented against x at y = 0.5 m, 1.5 m and 3.0 m. The velocity magnitude generally drops with an increase in the angle in all the cases and the peak moving far away from the heated plate. Likewise, the thickness of the thermal boundary layer also drops with the angle, especially when $b \geq 70°$. But, an increase in the air temperature beside the heated wall is caused by the buoyancy force component acting normal to the surface.

This buoyancy force also affects the transition process with a delay in the separation of the sub-layers from the heated surface, causing a much higher velocity gradient close to the adiabatic wall with an occurrence of backflow predicted at the far downstream besides the adiabatic wall (see Figure 7. 12 - Figure 7. 13 frames c and f) when $\theta \geq 70°$.

7.4.3. Evaluation of the transition stage

In this section, comparison of the numerical predicted results with various experimental data is made on the critical Grashof number derived from $Gr_c = g\beta(T_p - T_\infty)L_c^3/\nu^2$ at the critical distance (L_c). Comparison in Figure 7. 14 shows that our numerical results for the one heated plate case have very good agreement with the experimental data of Lloyd and Sparrow [1970] at θ = 0° and 10°. While the result of Hassan and Mohamed [1970] clearly under-predicted the critical Grashof number compared to Lloyd and Sparrow [1970]. AL-Arabi and Sakr [1988] reported the results at the start and end of transition (filled circle and square respectively), and our results show good agreement with the former data while under-predict against the latter data. Tritton [1963], on the other hand, paid particular attention to the vertical and inclined (≤ 50°) plates heated both above and below. He found $Gr_c = 9.26 \times 10^6$ on the vertical plate (not shown in this figure), which clearly falls very much compared to the other experimental data presented in Figure 7. 14. This under-prediction occurred due to the effects of the strong disturbances in the laboratory room and the uncertainty into the evaluation of the vertical critical distance, as mentioned by Tritton himself. We also note here that no other suitable data are available for the other orientation angles; therefore it is not possible for us to compare the results at higher angles**.**

Moreover, in the case of channel with the heated surface facing downward, very little information is available in the literature and the transition data are unavailable to make any comparison against the simulated critical Grashof numbers for various *b*. But the results, already presented in Figure 7. 11 for b = 0.08 m and 0.10 m, show satisfactory agreement in the critical distance estimated by using the three different physical quantities. Critical Grashof numbers for other values of the channel width from b = 0.06 m to 0.30 m are also shown in Figure 7. 14. With a small increase in the width from b = 0.06 m to 0.08 m, the critical Grashof number increases which again suggests a late transition of the flow. Variation in the transition point appears to be almost steady until the channel is nearly horizontal. But, further increase in the width from 0.08 m to 0.30 m causes an early transition and, as a result the critical Grashof number increases gradually first with the inclination angle and then rapidly when $\theta \geq 50°$. In fact, for the single heated plate case facing downward a ten-fold increase in the critical Grashof number is predicted when it is inclined at $\theta = 85°$ from the vertical position.

7.4.4. Effect of temperature of air and plate on the transition stage

In this section, the following variations in the temperature of air and heated plate have been examined 15°C, 25°C, 30°C and 70°C, 90°C, 100°C respectively, for b = 0.10 m and 0.20 m. The main objective here is to investigate the effects of the buoyancy force, which is generated by the difference of the flow density as a result of the air and plate temperatures, on the transition stage. Numerical results will be summarised for dimensional critical distance and non-dimensional Grashof number.

Figure 7. 15 shows the critical distance on the heated plate for b = 0.10 m (frames a and b) and b = 0.20 m (frames c and d). Note that when the air temperature (Ta) was varied, the plate temperature fixed at Tp = 70°C, while the air temperature was fixed at Ta = 15°C for the variation of the plate temperature. It can be seen in Figure 7. 15 that the critical distance generally increases with the orientation angle irrespective of the variations in the temperature and the channel width. Therefore, the transition occurs later when the channel is moved from its vertical position. Effect of the air temperature is noticeable in Figure 7. 15 (a-c), where an increase in the air temperature increases the critical distance, again resulting a late transition with more stable flow. However, the effect of increasing the plate temperature, as seen in Figure 7. 15 (b, d), is totally opposite, where the critical distance drops due to the flow becoming unstable and therefore the transition stage is predicted to start early.

Numerical results are summarised in terms of the critical Grashof number $Gr_c = g\beta(T_P - T_a){L_c}^3/\nu^2$, determined from the critical distance (L_c) and presented in Figure 7. 16. Note that when the air temperature (Ta) was varied we kept the plate temperature fixed at Tp = 70°C, while the air temperature was fixed at Ta = 15°C for the variation of the plate temperature. It can be seen in this figure that the critical Grashof number generally increases with the orientation angle irrespective to the variation in the temperature and the channel width. In fact, I find about a ten-fold increase in the magnitude of the critical Grashof number when the channel is rotated from its vertical to a nearly horizontal position. Therefore, it can be concluded again that the transition is delayed when the channel is moved from the vertical position.

In terms of the variation of both the plate and air temperatures, a very little effect is found on the critical Grashof number when $\theta \leq 50°$. While at a relatively large angle (e.g. when $\theta > 50°$) the effect found is more pronounced

for b = 0.10 m (frame a) than b = 0.20 m (frame b). Specifically, the results in frame (a) show that the critical Grashof number for the cases with $\theta > 50°$ drops when the air temperature is increased from 15°C by fixing the plate temperature to 70°C. This behaviour further illustrates the flow becoming unstable at the early stage of the transition process. However, increasing the plate temperature shows an opposite effect, again resulting a late transition with more stable flow at a higher orientation angle. In the case of higher channel width (frame b), as already mentioned, variation on the air temperature seems to have a moderate effect on the critical Grashof number than the plate temperature when $\theta > 50°$.

7.5. Conclusion

Effects of inclination angle of the parallel-plate channel and its width on the developing free-convection flow have been investigated numerically under various thermal and geometrical conditions. For example, the inclination angle was varied from 0° to 85° from the vertical position when the distance separating the two parallel plates was systematically reduced from 0.45 m to 0.06 m.

Results presented show that the average value of heat transfer coefficient depends on both the width and angle of the channel. Fixing the channel inclination and increasing the channel width from 0.06 m, we find that the heat transfer coefficient initially drops to a minimum value, followed by increment at a large width. This effect becomes very small when the adiabatic plate is located relatively at a far distance apart. However, when the angle of the channel is over 70°, the thickness of both the thermal and velocity boundary layers drop sharply due to the flow intensity increased especially around the middle of the channel, resulting an increased outlet temperature. At the

transition stage, the results also show that both the width and inclination of the channel have major effects. For example, as the inclination angle is increased, the transition stage moves further downstream of the channel. The critical distance predicted by both the velocity and turbulent kinetic energy agree very well, while it is slightly over-predicted by the local heat flux as a result of the buoyancy force increasing to the normal of the heated plate. Good agreement is obtained while compared the critical Grashof number with various experimental data. Moreover, different values of the air and plate temperature are used to examine the transition stage in the channel.

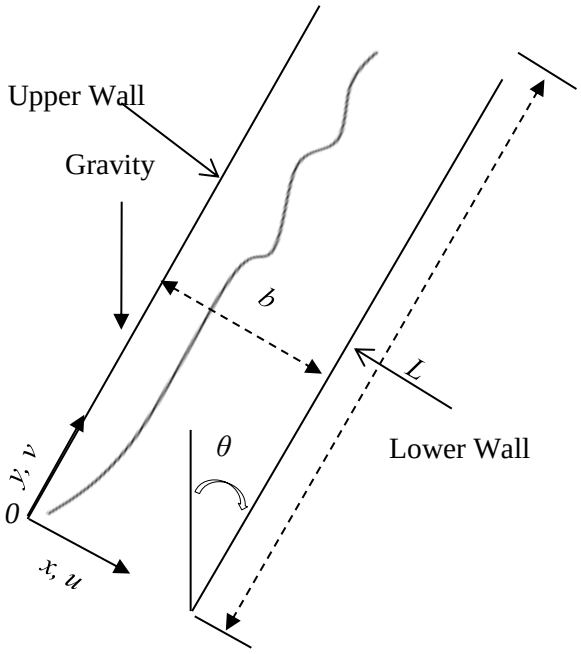

Figure 7. 1 Flow geometry with coordinate directions.

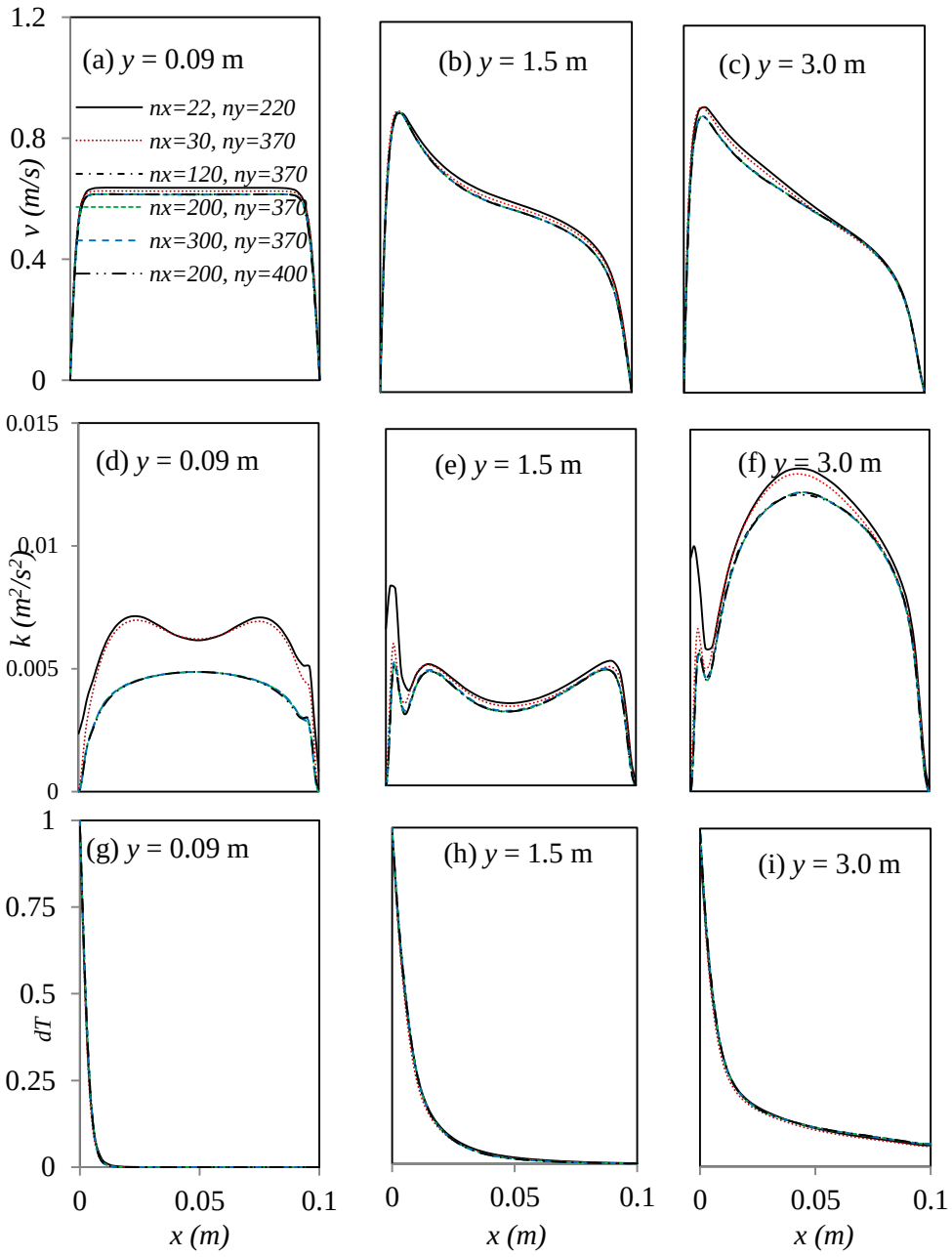

Figure 7. 2 Mesh dependence test showing on the results of the velocity, turbulent kinetic energy and air temperature at different locations along the channel at $\theta = 45°$.

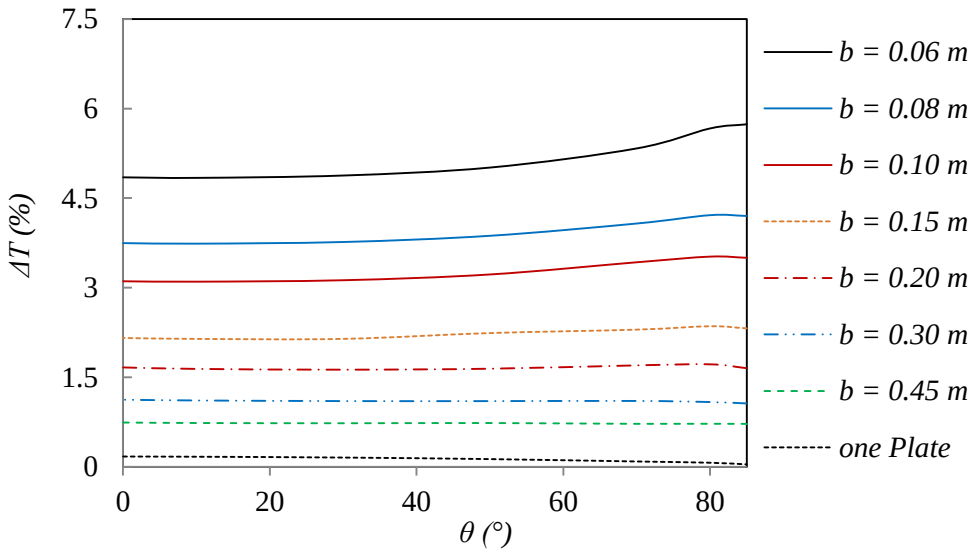

Figure 7. 3 The average outlet tempreature at *Ta* = 15°C and *Tp* =70°C.

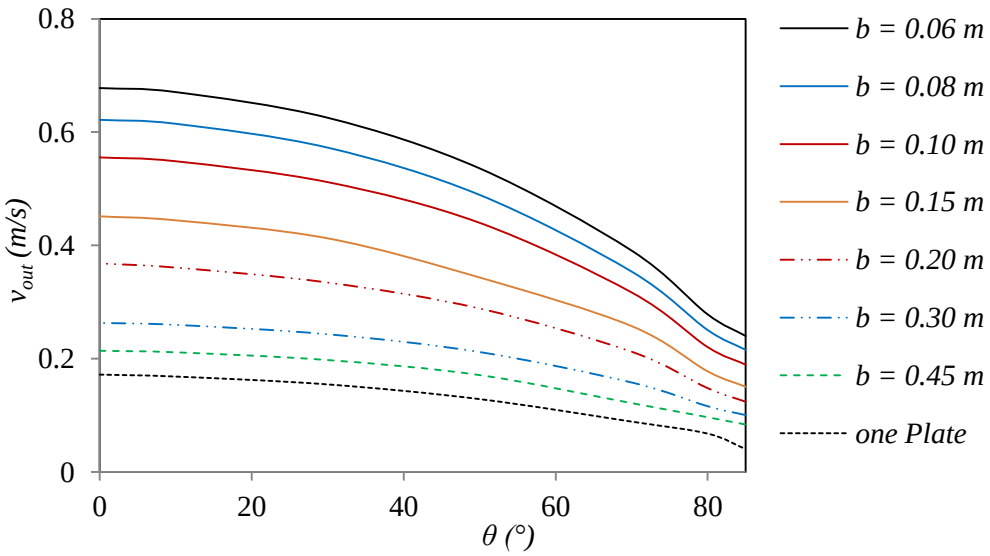

Figure 7. 4 The average outlet velocity at *Ta* = 15°C and *Tp* =70°C.

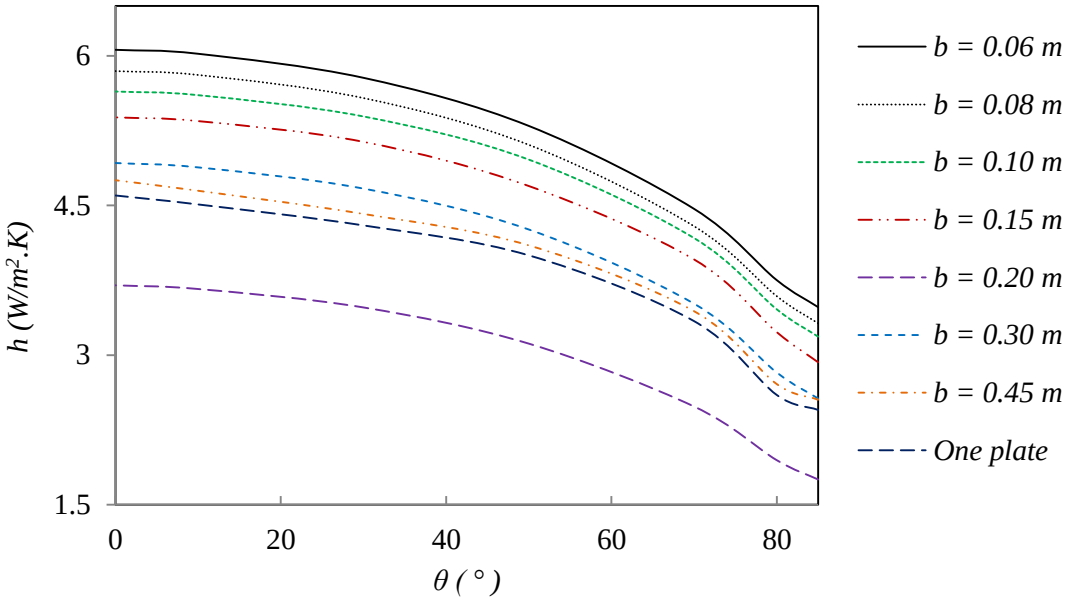

Figure 7. 5 Effect of the channel width on the average heat transfer at *Ta* = 15°C and *Tp* =70°C.

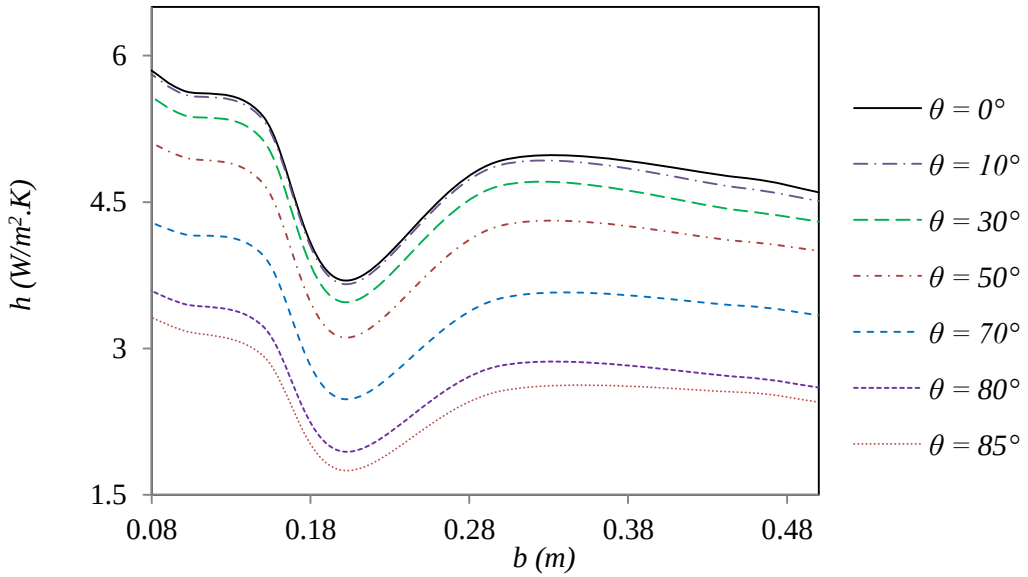

Figure 7. 6 Effect of the inclination angle on the average heat transfer at *Ta* = 15°C and *Tp* =70°C.

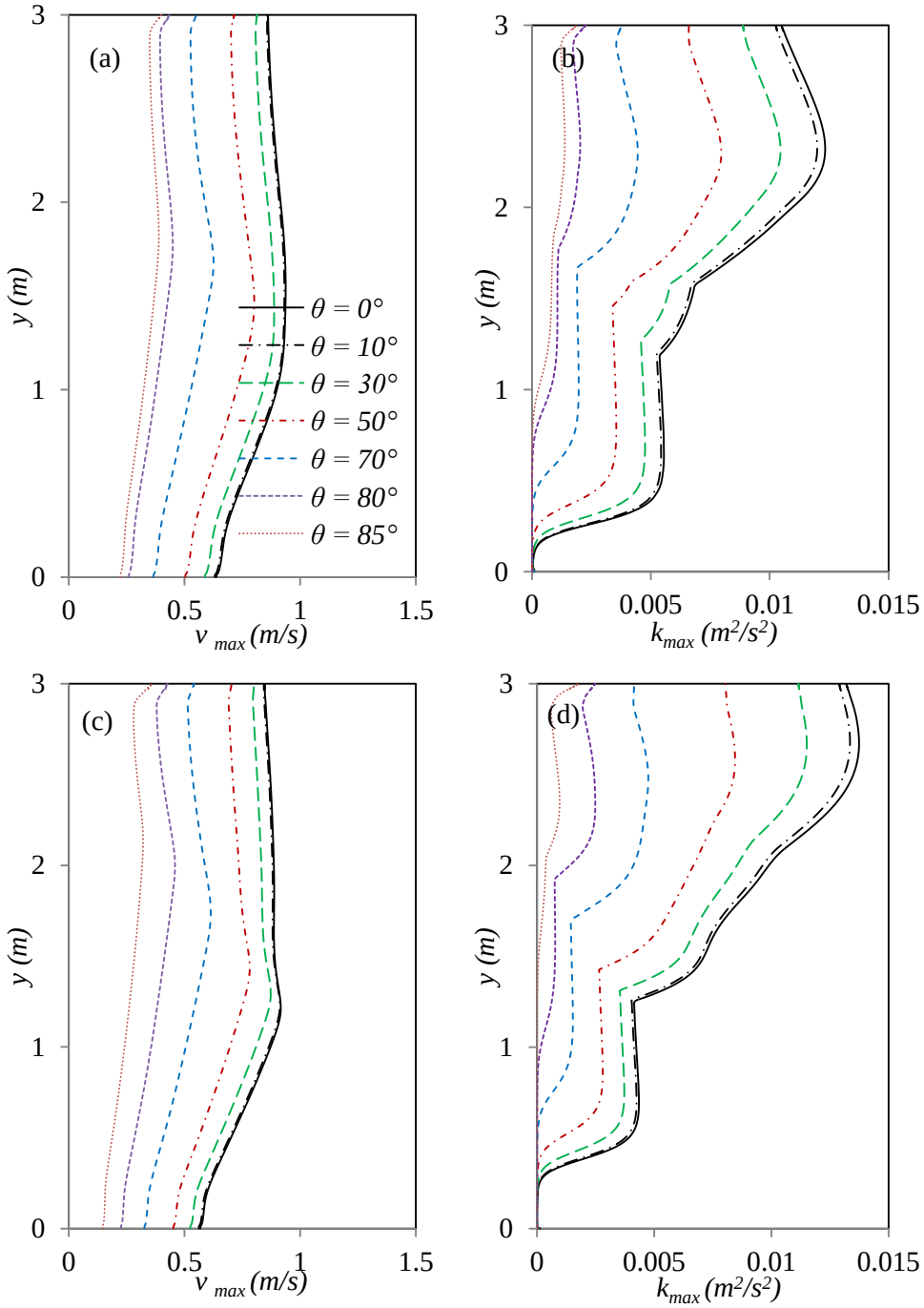

Figure 7. 7 Distributions of the maximum velocity and turbulent kinetic energy for b = 0.08 m (a, b) and b = 0 .10 m (c, d) at Ta = 15°C and Tp =70°C.

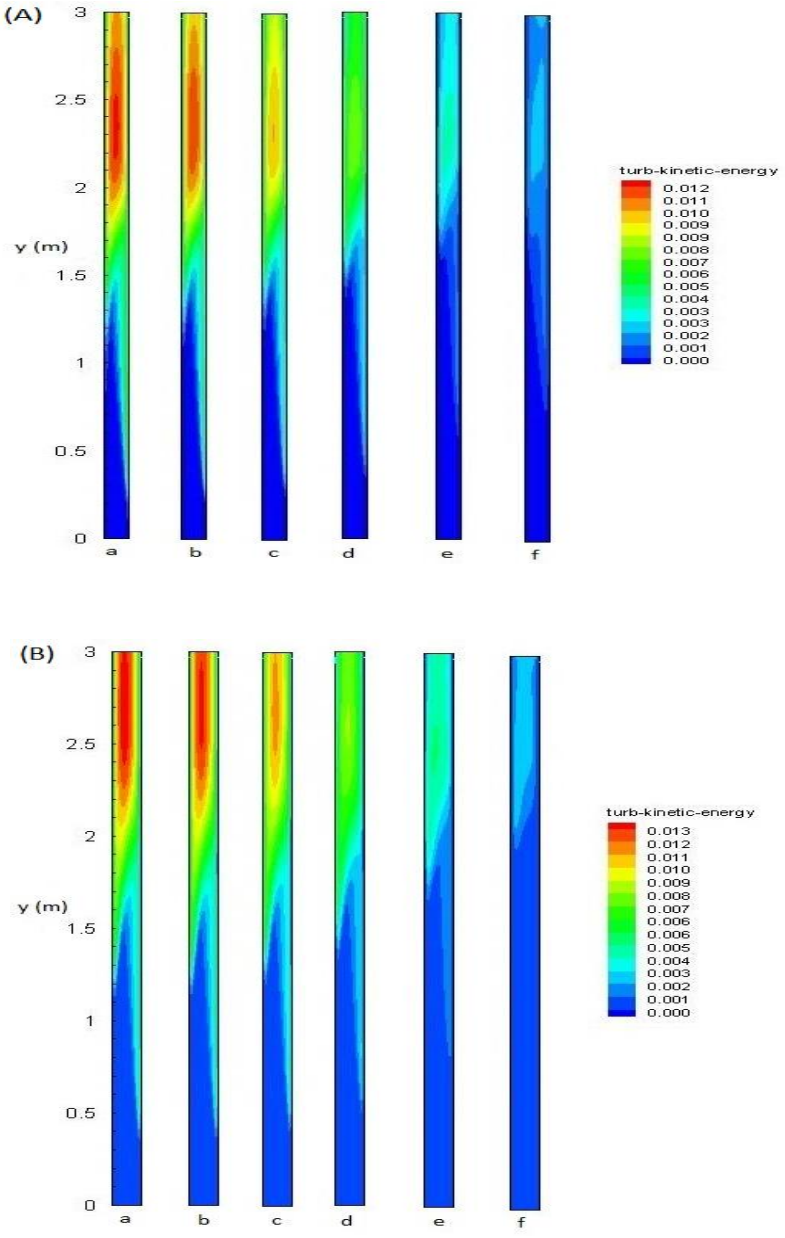

Figure 7. 8 Contours of the turbulent kinetic energy, where the width of the channel is (A) 0.08 m and (B) 0.10 m and the angle θ is (a) 0°, (b) 10°, (c) 30°, (d) 50°, (e) 70° and (f) 85°.

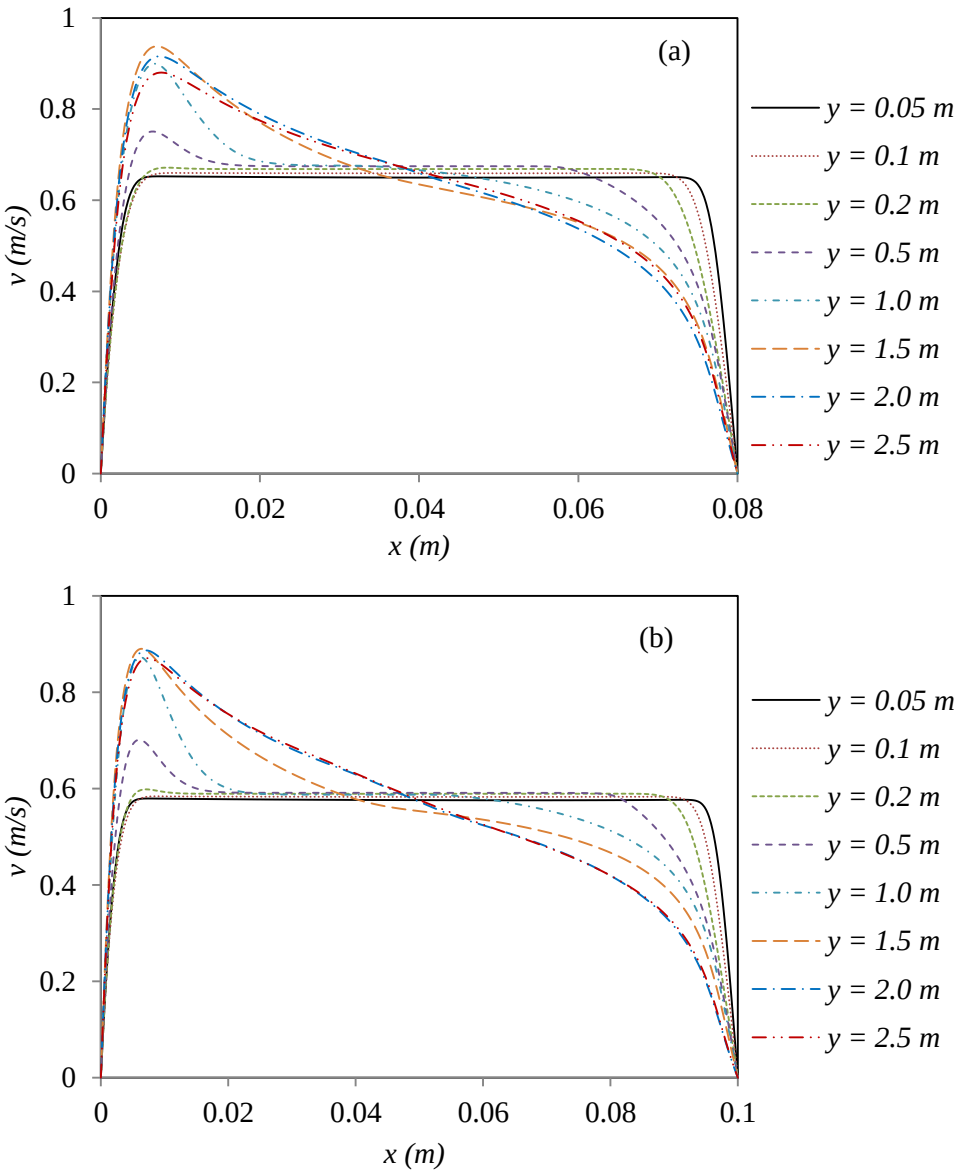

Figure 7. 9 The distribution of the velocity inside the channel where b = 0.08 m (a) and b = 0.1 m (b)

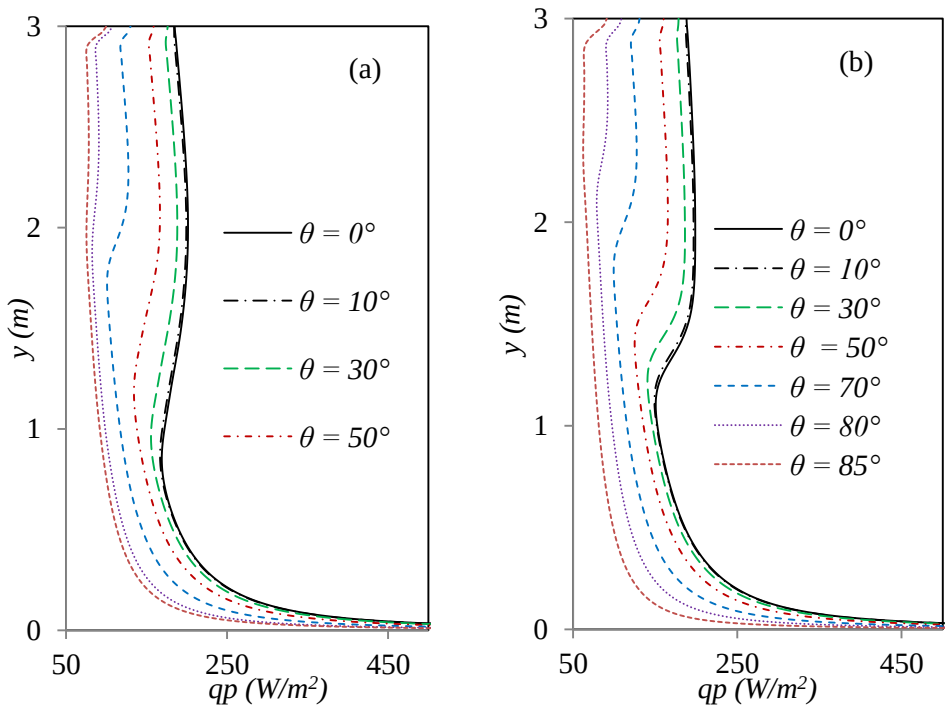

Figure 7. 10 The distribution of the local heat transfer for (a) b = 0.08 m and (b) b = 0.10 m.

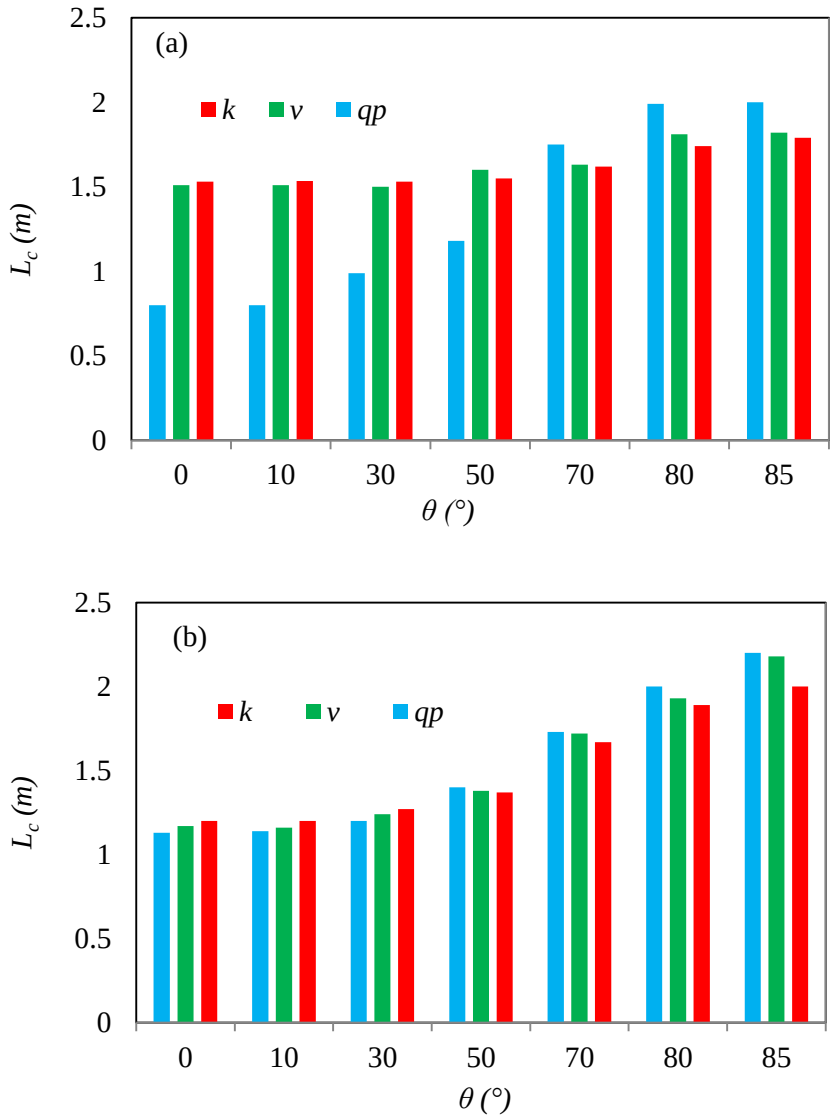

Figure 7. 11 The critical distance derived from the velocity, turbulent kinetic energy and plate heat flux for (a) b = 0.08 m and (b) b = 0.10 m.

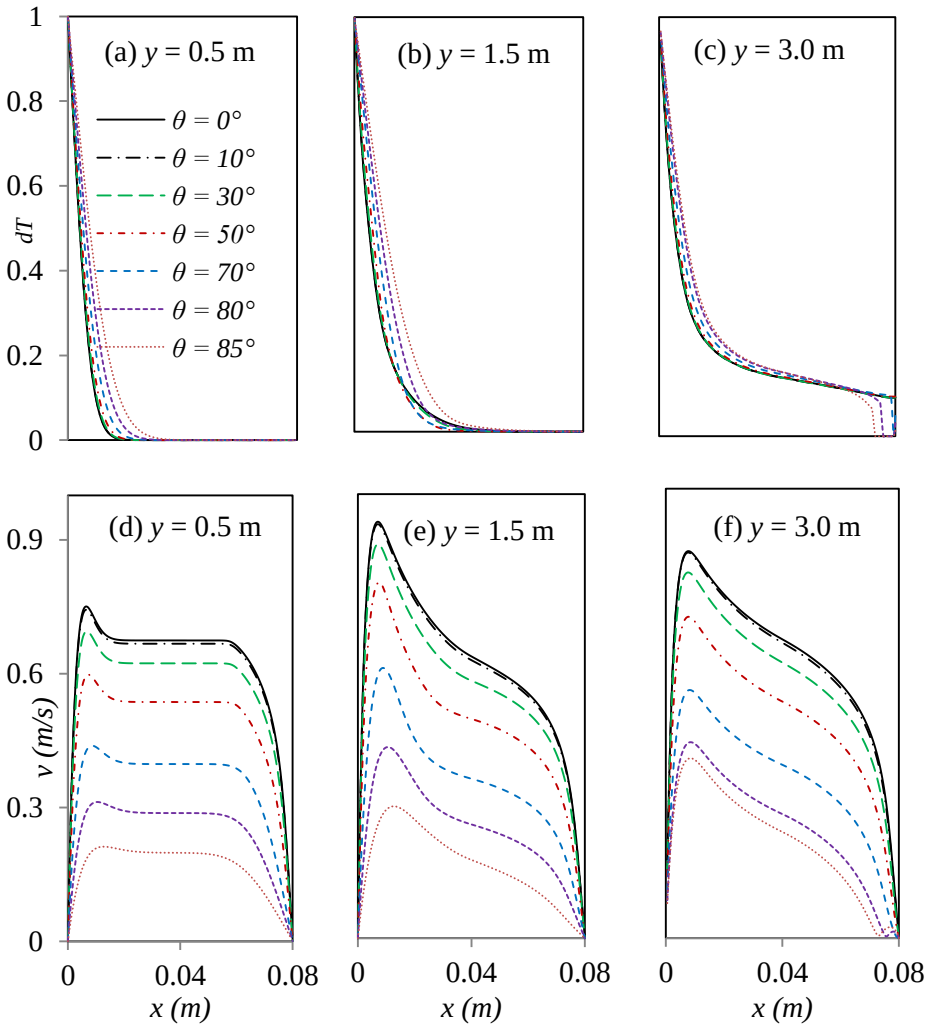

Figure 7. 12 The distributions of the temperature (a-c) and velocity (d-f) for b = 0.08 m.

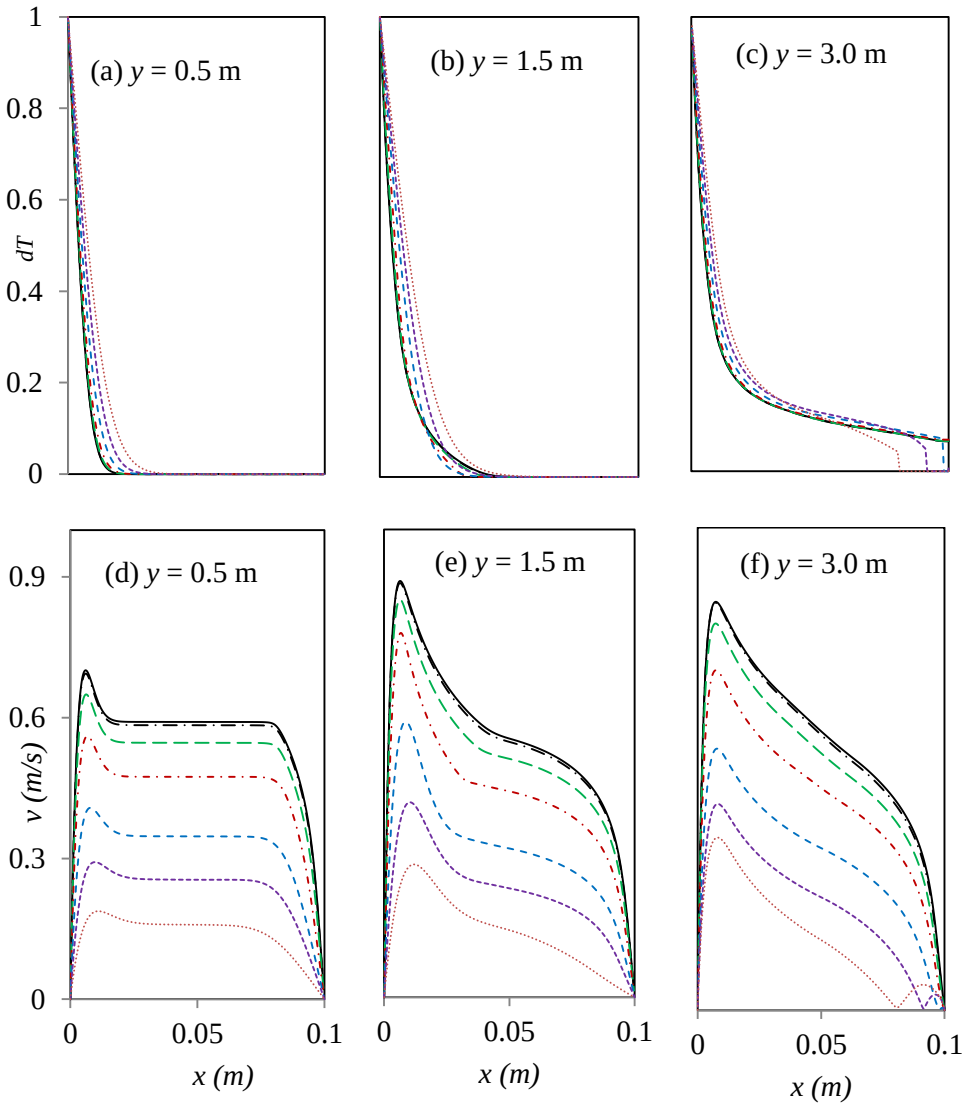

Figure 7. 13 The distributions of the temperature (a-c) and velocity (d-f) for b = 0.10 m.

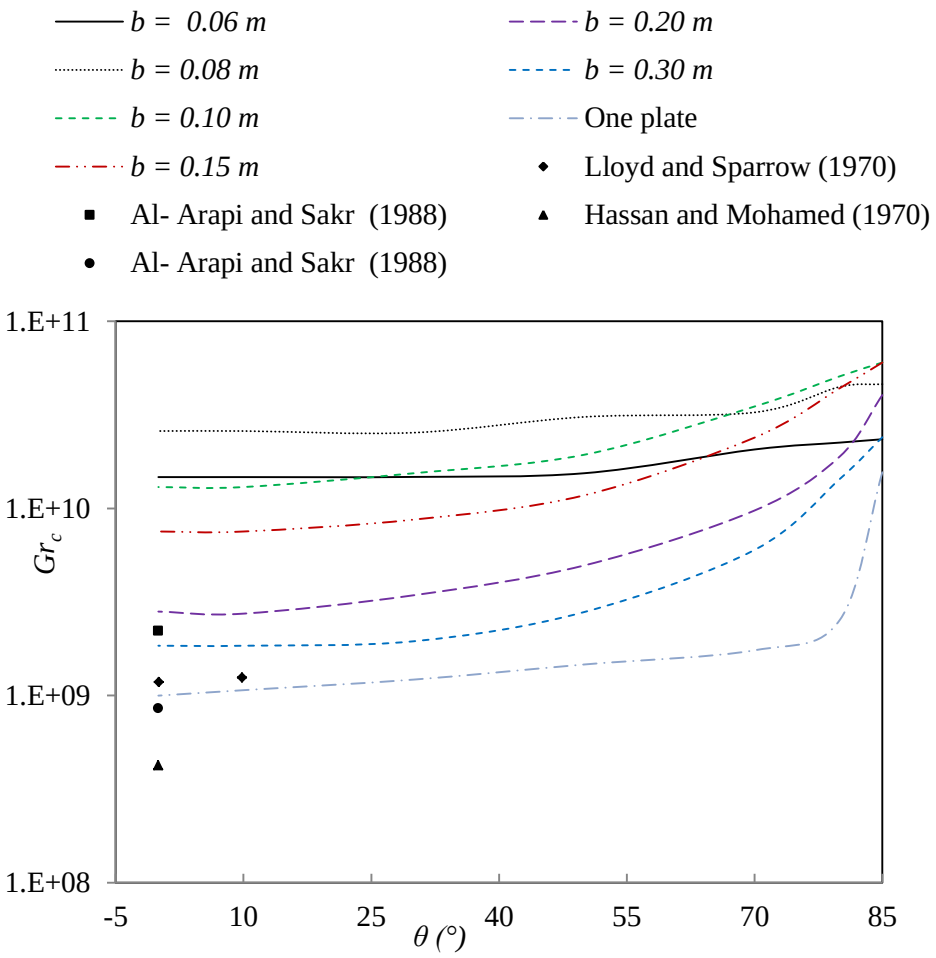

Figure 7. 14 The critical Grashof number derived at different inclination angles and *b*. Symbols = single plate measurements.

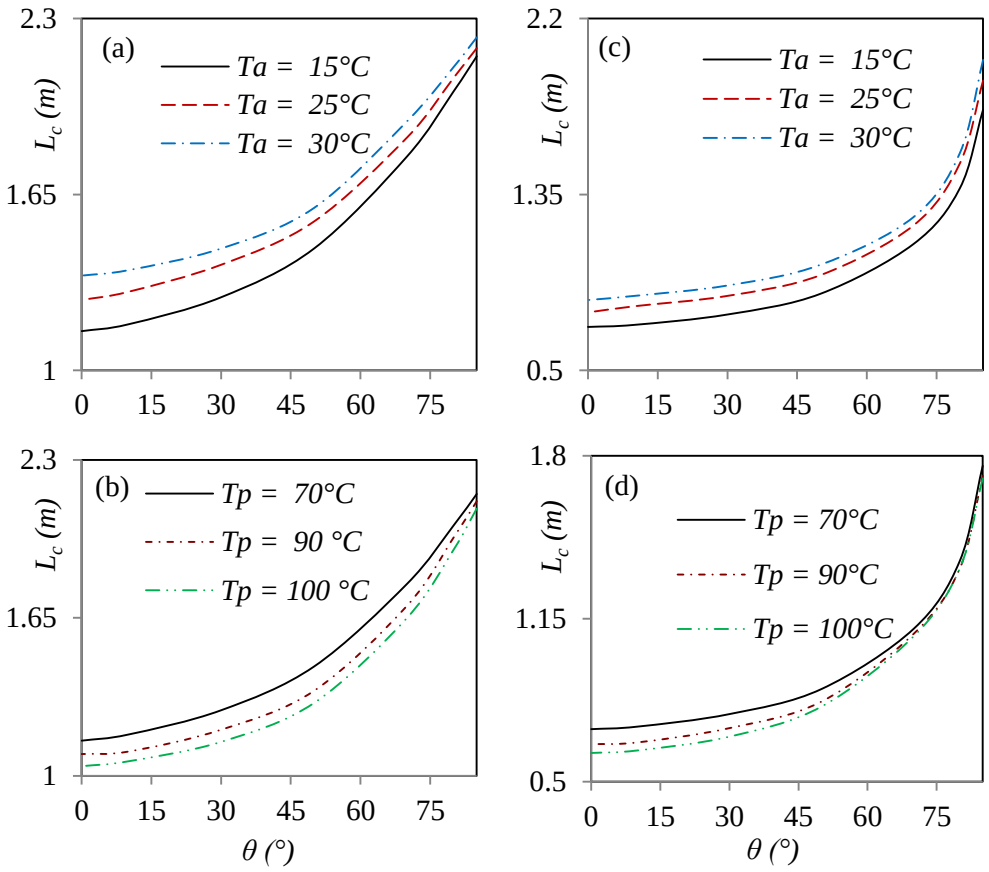

Figure 7. 15 Critical distance on the heated plate for (a, b) b = 0.10 m and (c, d) b = 0.20 m.

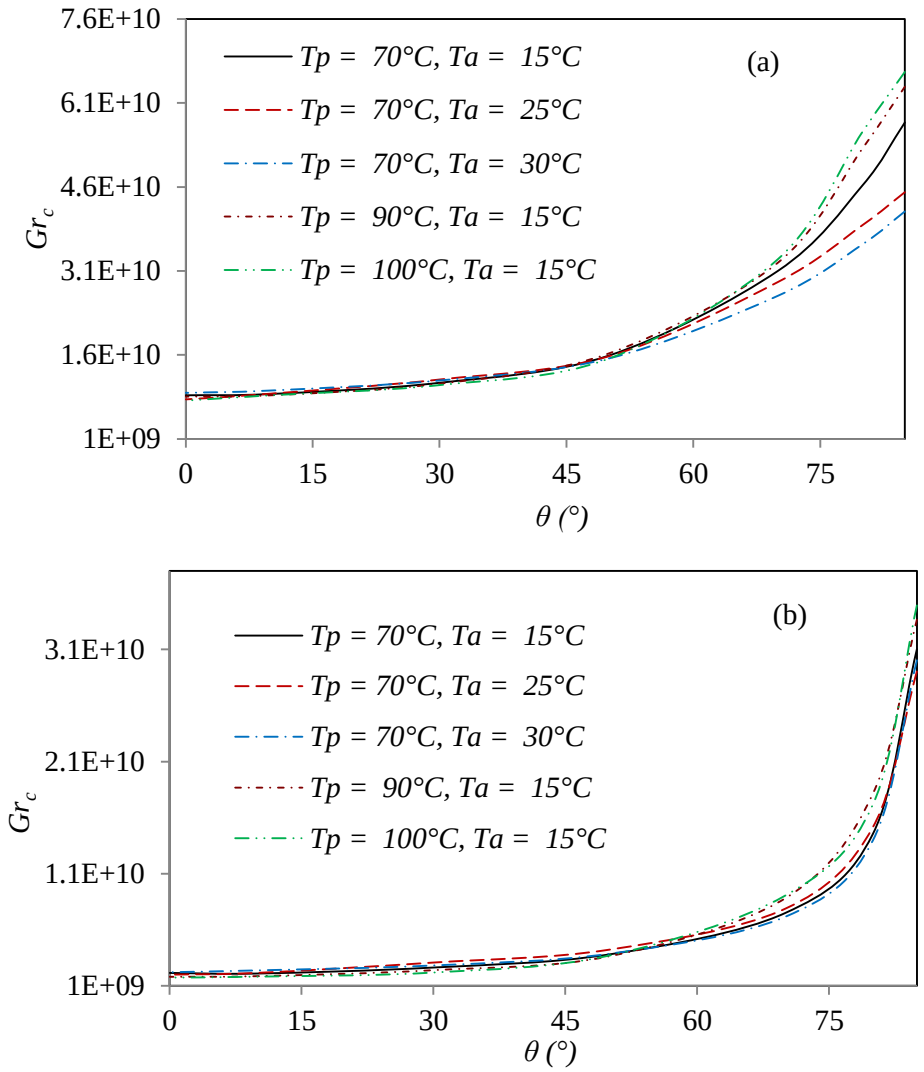

Figure 7. 16 Critical Grashof number on the heated plate for (a) b = 0.10 m and (b) b = 0.20 m.

Chapter 8

Large Eddy Simulation of transition of free convection flow over an inclined heated plate facing upward

8.1. Introduction

In the previous Chapter, numerical simulation of free convection flow inside a heated channel facing downward was carried out by k-ε model and a satisfactory agreement of the critical distance indicating the flow transition was obtained with experimental data. In the case of an inclined heated wall facing upward, initial results obtained by the k-ε models disagree with the experimental data of Hassan and Mohamed [1970], Al arabi and Sakr [1988]. In this case, by using FLUENT code, the k-ε models were unable to predict accurately the transition stage when the plate was rotated at various angles. Particularly, the results obtained by the k-ε models showed that the transition occurs late when the angle of the plate is increased from its vertical position. However, the experimental data suggest the opposite, that is, an early transition will occur for increasing the plate angle. Therefore, it was necessary to change the simulation technique in this case to obtain a satisfactory result.

The Detached Eddy Simulation (DES) and Large Eddy Simulation (LES) of FLUENT were tested, but it was very expensive to run a 3D simulation on a single CPU. Therefore, I have decided to use an in-house LES-BOFFIN code

which is fully parallel and runs on multiple CPUs. It was initially developed for simulating turbulent reacting flow, but has been modified and extended in the present work to solve for free convection flow.

The aim is to provide an in-depth investigation on transition phenomena by an advanced numerical method such as LES. Particular focus is given on the behaviour of transition of free convection flow developing on a heated plate at various inclination angles. Also I investigate how the flow and thermal fields jointly affect the transition process and further examine the effects they have on the turbulent quantities such as fluctuating velocity components which are generated following by the flow transition.

8.2. Model geometry

A schematic of the model geometry with coordinate systems is given in Figure 8. 1. The computational domain used for the LES is three-dimensional. An isothermal heated plate, temperature of which is denoted by *Tp*, is exposed to the environment at an ambient temperature denoted by *Ta*. Driven by the buoyancy force, the air is expected to be heated by the hot wall which will then flow along the heated surface and form natural velocity and thermal boundary layers.

The length ($L=L_y$) of the plate used in the simulation is 3 m in the *y* direction. The free boundary opposite to the plate is placed at a distance equal to 3.5 times the thickness of the fully developed boundary layer downstream. A width (L_x) of 1 m used along the *x*-direction is therefore sufficient for this. The spanwise boundaries (L_z) in the *z*-direction is considered to be 1.5 m apart, which is also sufficiently large for implementing a periodic boundary condition in the spanwise direction.

8.3. Boundary conditions

The boundary conditions applied in the LES are described below.

At the inlet the velocity and temperature boundary conditions are applied as $\bar{u}(x) = 0, \quad \frac{\partial \bar{v}(y)}{\partial y} = 0, \ \bar{w}(z) = 0 \quad$ and $\quad \bar{T} = T_{amb}$

At the outlet boundary, a zero gradient condition of the form $\frac{\partial \bar{u}_i}{\partial n}\Big|_{out} = 0$, where $\frac{\partial}{\partial n}$ denotes the gradient taken to the normal outflow boundary, has been used which was sufficient to minimise any effects of the outlet boundary in the solution. At the heated plate, no-slip condition is applied at a constant temperature *Tp*. A free boundary condition is employed at the side which is opposite to the heated plate. In the spanwise direction, a periodic boundary condition is employed.

8.4. Grid Resolution study

The numerical results to be presented are tested first for their dependence on a set of grid resolutions as shown in Figure 8. 2. Four grids are used to study one case and the results of air velocity and temperature in the laminar and turbulent stages are compared with the experimental data of Tsuji and Nagano [1988] and Yan and Nilsson [2005]. This mesh dependence test was performed by changing the total number of grid nodes in the three directions *y*, *x* and *z* as (n_y), (n_x), (n_z) respectively, which are 256 × 96 × 96, 292 × 124 × 96, 320 × 144 × 96 and 340 × 164 × 96. It is worth noting that the grid used is non-uniform and refined in the regions upstream as well as close to the wall where in most free convection problems a large gradient of velocity and temperature will occur. Mesh refinement is done by using a mesh–successive ratio of 1.016

in both the *y* and *x* directions, while in the *z* direction a uniform mesh distribution is used.

As we can see in Figure 8. 2. (a, b) that the first grid 256 × 96 × 96 provides an overestimation in the velocity and temperature within the laminar region. However the next three grids, 292 × 124 × 96, 320 × 144 × 96 and 340 × 164 × 96, produce satisfactory results, and the relative difference in the results among the last three grids is very small. Therefore, either of these three grids could be used, however to avoid any undesirable discrepancies in the numerical results the grid size of 320 × 144 × 96 is chosen to perform all the numerical simulations with a fixed time step $dt = 10^{-3}$. In addition, the numerical results obtained by the Realizable k-ε model, which was already presented in Chapter 1§ 4.3, are compared in Figure 8. 2, where a satisfactory agreement received between the two numerical results.

The code is fully parallel with an Open-MPI interface to communicate and share data among the multiple central processing units (CPUs) of a HPC cluster "miffy" available at the University of Glasgow. A total of 16 CPUs were used and each simulation took a wall-clock time of about 3 days to complete and reach to a statistically stationary result.

8.5. Results and discussions

8.5.1. Transition toward turbulence

In this section the consequence of events which leads to the onset of turbulence are reported. First, unsteady flow development and structures on a vertical plate are presented in Figure 8. 3 in a mid-location, in terms of the velocity and temperature fields, at three different randomly chosen time instances, 5s, 8s and 12s. However, the contour plots are zoomed in the upstream location to

particularly examine and better visualise the occurrence of the flow separation upstream within the vertical location $0 \leq y \leq 1.3$ m. Previous studies suggested that the laminar boundary layer developing over the uniformly heated surface becomes unstable to specific distance downstream. The contour plots in Figure 8. 3 (a) and (e) clearly provide an evidence of the initial breakdown of the laminar boundary layer, which amplify and then produce three-dimensional shear layers with concentrated turbulent bursts. These bursts are known to consume the laminar boundary layer region in the transition region; however, with an increase in time to 8 and 12 seconds the initial plum starts to expand and rise, causing an increase in the thickness of the boundary layer in the turbulent region as shown in Figure 8. 3 (b), (c) and (d).

The structure of the thermal boundary layer in three-dimensional filed is presented in Figure 8. 3 (h). The temperature varies along the plate with a very green dark colour showing low temperature especially at the bottom of the plate near the inlet section, while in the upstream the green colour appears as the temperature becomes very high there. The temperature on the surface can be used to determine the local heat transfer coefficients as already done in Figure 5. 27 in Chapter 5. The local heat transfer coefficient will be large in the low temperature region in the downstream and will be small in the high temperature in the upstream where some streaks and waves start to appear along the flow. Lloyd and Sparrow [1970] stated that the onset location of these streaks is equal to the position at which the flow takes the transition from its laminar to turbulent stage.

Similar sets of visualisation are carried out in Figure 8. 4 with an inclination plate of θ =-45°, where the breakdown in the laminar boundary layer initially starts (a, e) with more increase in the thickness of the boundary layers compared to the vertical case. As the time simulation time progresses, Figure 8.

4 (b) and (c) show that the thickness of the flow as well as thermal boundary layers becomes larger and widely spreads after a big explosion of the plume. As a result, the separation point of the flow shifts some distance towards the downstream with more unstable flow at the outer edge of the boundary layer.

8.5.2. Visualisation of the 3D boundary and thermal layers

Iso-surface contour plots of the flow fields and surface temperature in the whole computational domain are shown in Figure 8. 5 and Figure 8. 6 respectively at four different chosen angles 0°, -02°, -45° and -70. In general for the vertical plate at θ = 0° the thickness of the boundary and its thermal layers reach their maximum at the outlet section as indicated in Figure 8. 5 (a). With an increase in the plate angle to -20° their maximum value is still located at the outlet section, however the surface of the top shape becomes more flat compared to the vertical case especially in the boundary layer field where its top is very sharp.

Figure 8. 5 (c) at θ = -45° shows that the maximum value of the thickness at the outlet section disappears and the growth of both the boundary layers is likely to become flat along the plate. The same behaviour of the development of the thermal boundary layer can been in Figure 8. 6. However, with an increase in the plate inclination to -70°, both the boundary layer thickness become more disturbed, and the location of their maximum moves backward near the middle of the plate. This behaviour of the boundary layer development can be explained by the only component of the buoyancy force acting in the flow direction, which increases as the length of the plate is increased. Whereas, in the case of an inclination heated plate facing upward, a second component of the buoyancy force exists in the direction away from the heated plate which

causes the pressure in the boundary layer of the flow over the plate to be lower than the pressure surrounding area of the flow. This pressure further causes the flow to be induced near the inlet; as a result both the boundary and thermal layer thicknesses are increased with a magnitude drop in the mean temperature and velocity.

8.5.3. Turbulent velocity fluctuations

Root mean squares (rms) of the turbulent velocity fluctuations occurring very near to the hated vertical surface are shown in Figure 8. 7, in the y and x directions as v_{rms}/v_{max} and u_{rms}/v_{max} respectively. These results are plotted as a function of the dimensionless transverse coordinate, $(x/y)\ Nu$, in order to make a direct comparison with varies experimental data. The numerical profile of v_{rms}/v_{max} appears to have two peaks, where the first one appears in the buoyant sublayer region ($0.1 < (x/y)\ Nu < 1.0$) while the second one is in the outer region ($1.0 < (x/y)\ Nu < 10$), with a maximum situated at a position of the boundary layer beyond the location of the maximum velocity reported in Figure 8. 2. (d). This finding shows a good agreement with the experimental data of Miyamoto and Okayama [1982]. The numerical results of v_{rms}/v_{max} have also an agreeable trend the experimental data of Smith [1972] at a Grashof (Gr) of 4.84×10^{10}. On the other hand, the peak of u_{rms}/v_{max} appears in the outer region and agrees well with Kato et al. [1993] who used a Laser Doppler anemometer to measure the air velocity. However, the data of Tsuji and Naga [1988] at $Gr = 8.44 \times 10^{10}$ are different in both the cases v_{rms}/v_{max} and u_{rms}/v_{max} who used a hot wire measurement technique for the velocity and gave a higher value in the buoyant sublayer.

The distributions of the velocity *rms* along the heated plate are shown in Figure 8. 8 at $\theta = 0°$ and -70° and at different vertical locations of y, 0.5, 1.0, 1.5, 2.0

and 2.5 m. The component of the velocity fluctuation v_{rms} in the flow direction is likely to be equal zero at y = 0.5 m as the flow is in the laminar stage, Fig. 8 (a). As the flow becomes full developed toward the downstream, the peak of the velocity fluctuation v_{rms} and u_{rms} shows a gradual increase. With an increase in the angle to -70°, the two peaks of v_{rms} move out of the heated plate as can be seen in Figure 8. 8 (d). Moreover, compared to the vertical case, the intensity of v_{rms} and u_{rms} drops sharply at θ = -70° because of an increase in the boundary layer thickness, explained in the contour plots in Figure 8. 5. However, the velocity fluctuation in the z direction rises, as shown in Figure 8. 8 (f), with the peaks of w_{rms} recorded in the outer region of the boundary layer, x > 0.01 m, and move to the buoyant sublayer region when θ = -70°. This further indicates that the maximum velocity in the spanwise direction occurs very close to the heated plate.

Figure 8. 9 shows the contours plot of the velocity *rms* at four different angles 0°, -20°, -45° and -70°. As the angle of the plate increases the v_{rms} decreases in the y direction, so the intensity of its fluctuation drops. The variation of v_{rms} shown at 70° in Figure 8. 9 (i) accord with the field of velocity distribution presented in Fig. 5 (d). Overall, it can be seen that with an increase in the angle both the intensity of the velocity in the y and x directions drop but increases in the w direction.

8.5.4. Critical Grashof number

In the final figure, Figure 8. 10, the location of the transition taking place on the heated plate is summarised in terms of the critical Grashof number determined by the critical distance from the local variation of the surface heat transfer coefficient (e.g. see Chapter 5 for details). The value of *log(Grc Pr)* corresponding to the point where the transition starts compare generally well

with that of the experimental data of Al-Arabi and Sakr [1988] and Hassan and Mohamed [1970] obtained at the end of the transition stage (solid lines). While, their data at the beginning of the transition stage (dashed lines) fall below the numerical results at a wide range of the plate orientation angles. The same behaviour found in the experimental data of Lloyd and Sparrow [1970]. However, most of the experimental data $\theta < 25°$ agree reasonably well with the present numerical results. In terms of understanding the transition behaviour of the flow, these results further confirm that an early transition occurs when the plate angle is increased.

8.6. Conclusion

Three dimensional large eddy simulations of free convection along an inclined heated plate are carried out using an in-house LES-BOFFIN code. it reported that the predicted mean temperature and velocity in the turbulent and laminar flows over the vertical plate have good agreement with the experimental data. The *rms* of the velocity fluctuations also compared well.

Visualisations of the boundary layer and its thermal thickness are provided, which indicate that with an increase in the angle of the plate the boundary layers began to roll over the outer edge of the boundary layer after the transition. This leads to a fall in the mean velocity and temperature in the boundary layer.

The inclination of the plate increases the peak velocity fluctuation in the y direction as the v_{rms} moves out of the region of the boundary layer, while in the z direction the peaks of the velocity fluctuation w_{rms} move to the buoyant sublayer region.

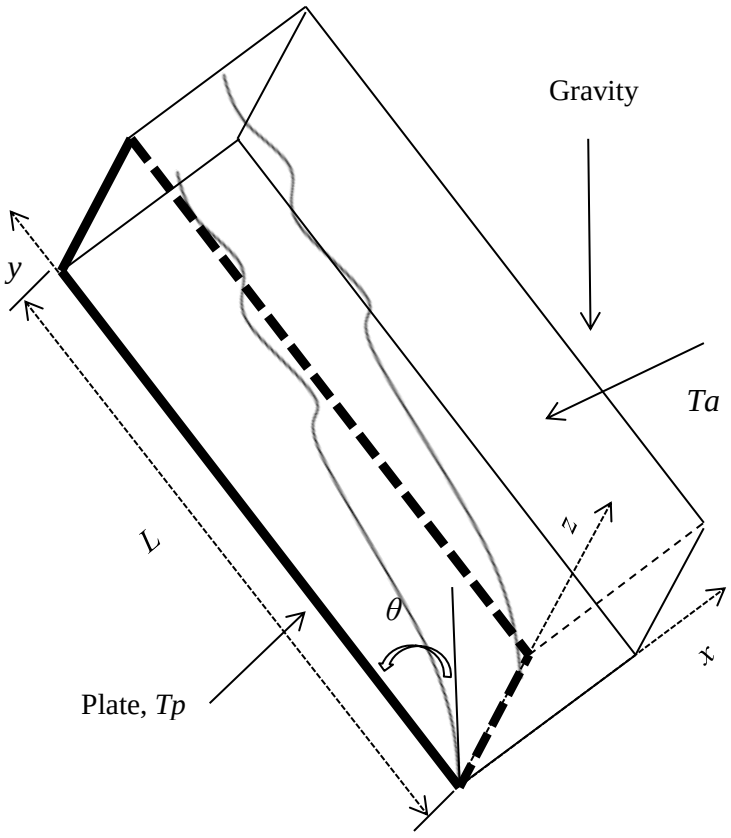

Figure 8. 1 Flow geometry with coordinate systems

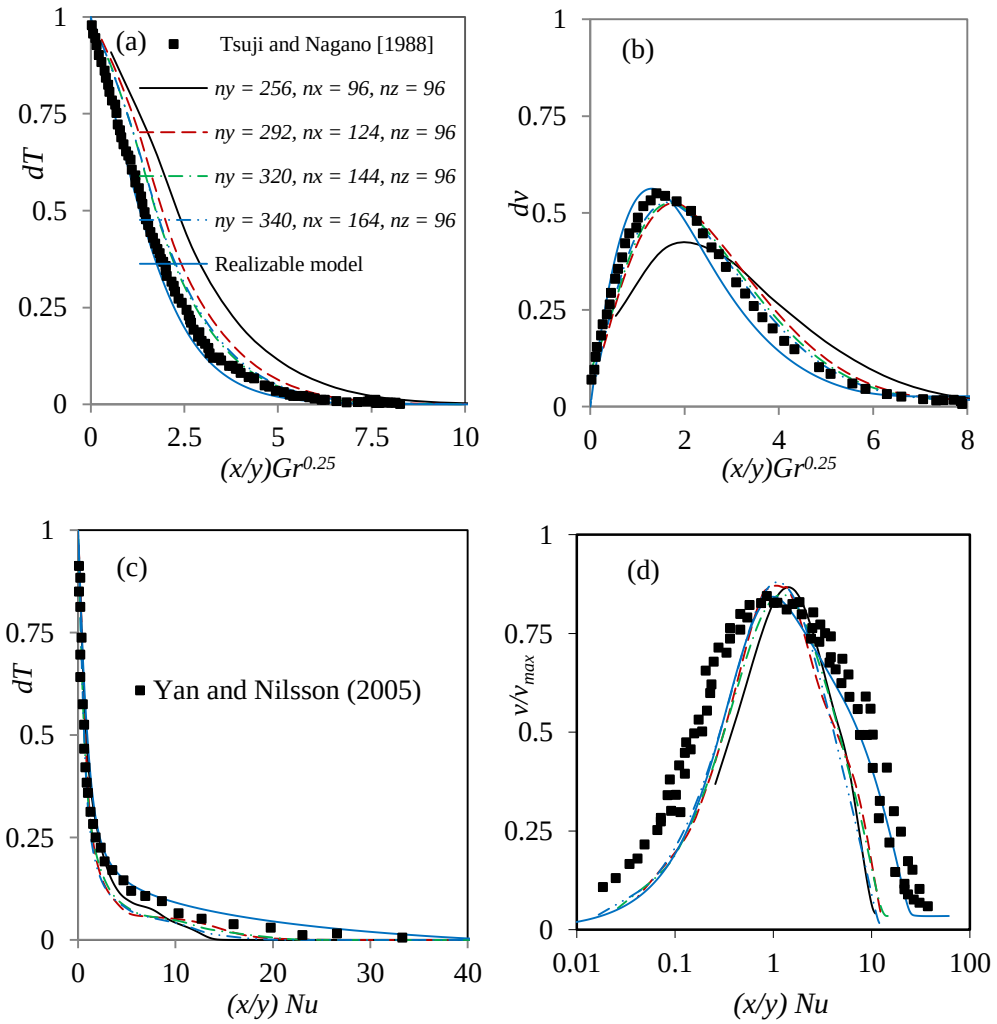

Figure 8. 2 Mesh dependence on the velocity and temperature results in the laminar stage (a, b) and turbulent stage (c, d).

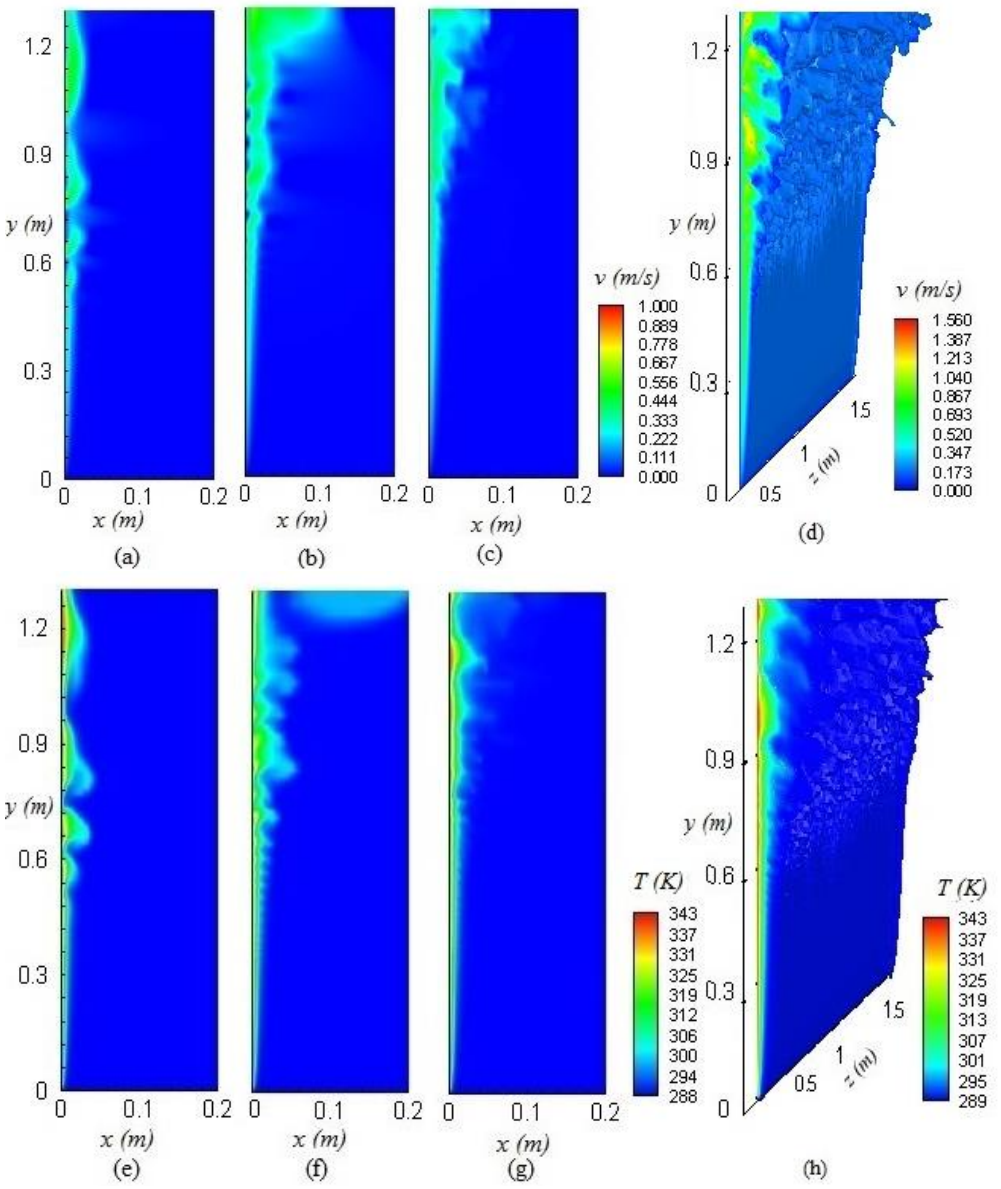

Figure 8. 3 Development of turbulent structure upstream on the vertical plate at $\theta = 0°$, where (a-c) the velocity contours and (e-g) the temperature contours at 5, 8 and 12 seconds respectively. A three–dimensional view of them at the final timestep is shown in frames (d) and (h) respectively

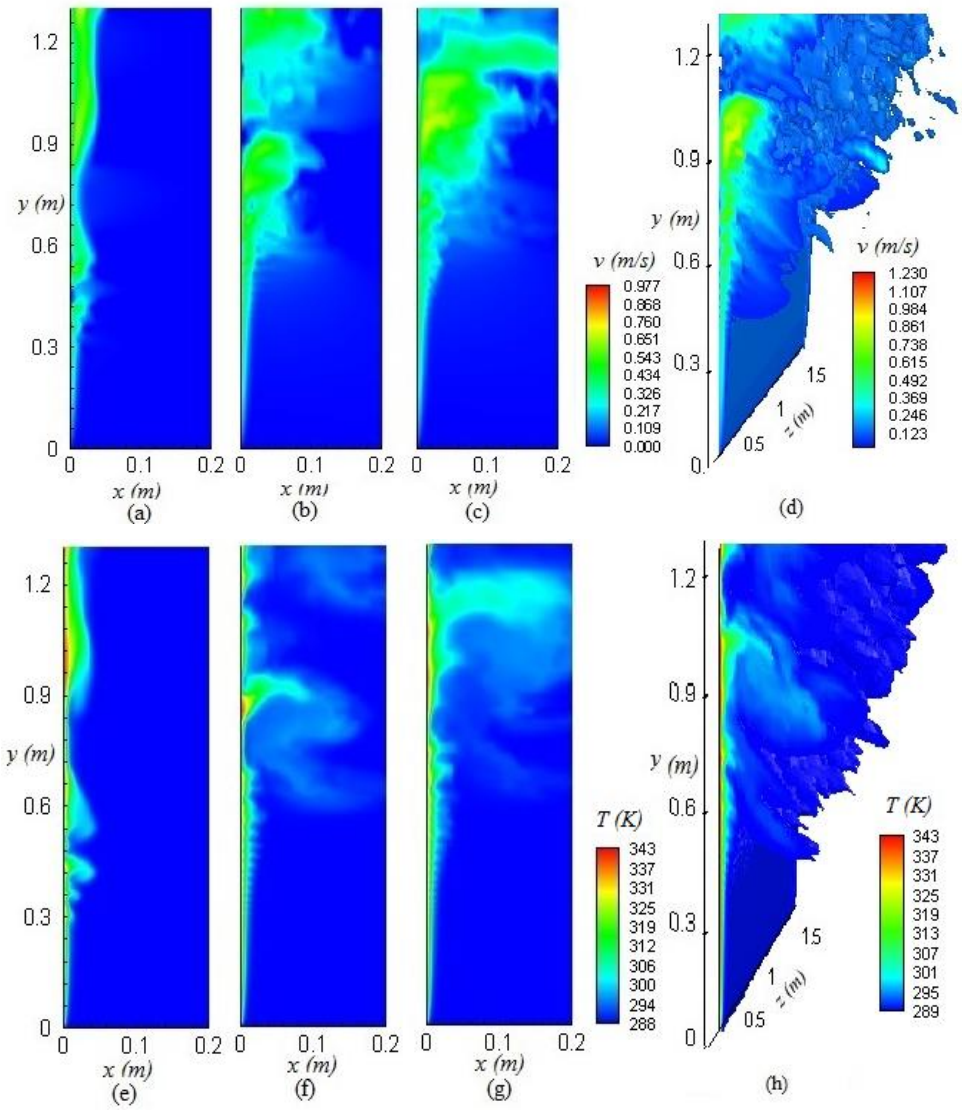

Figure 8. 4 Development of turbulent structure upstream at an inclination θ = *-45°*, where (a-c) the velocity contours and (e-g) the temperature contours at 5, 8 and 12 seconds respectively. A three–dimensional view of them at the final timestep is shown in frames (d) and (h) respectively.

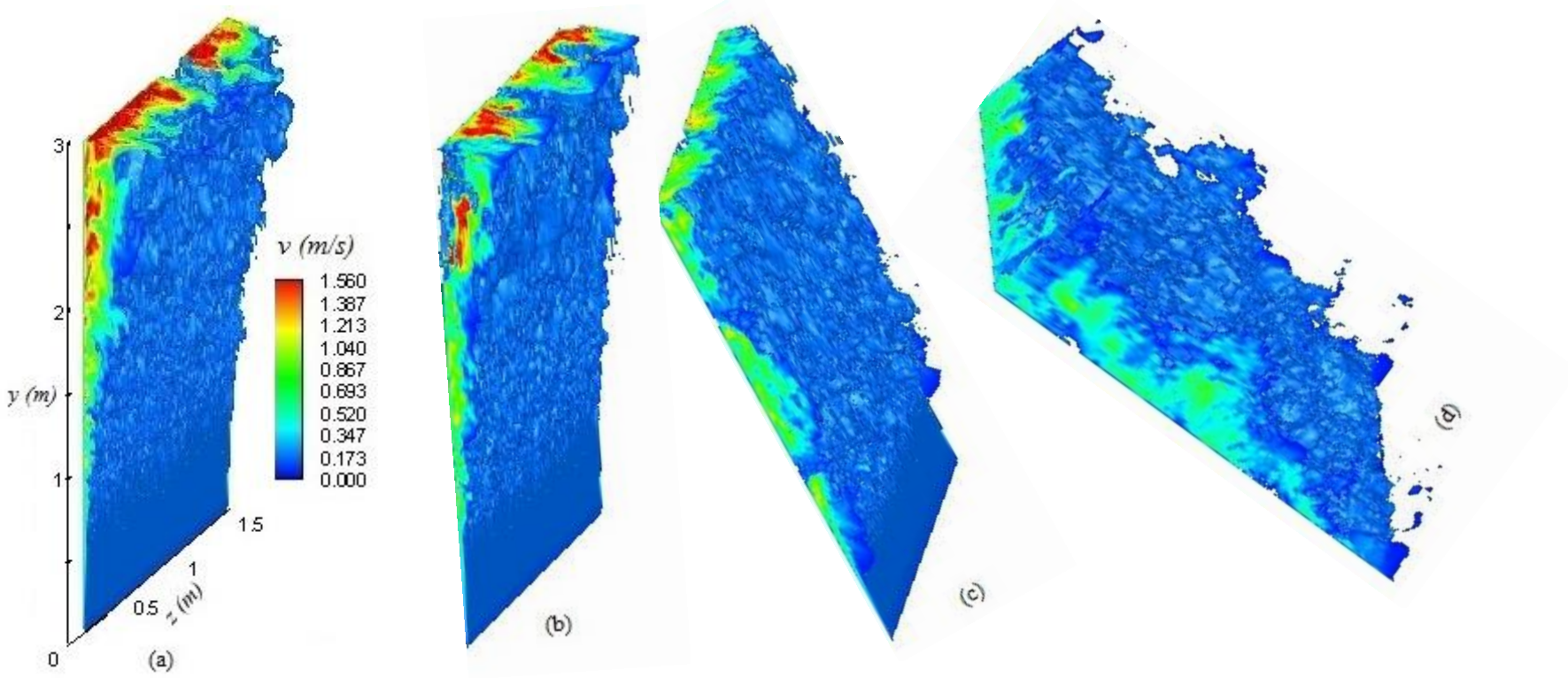

Figure 8. 5 Velocity iso-surface contour plots at θ = 0° (a), θ = -20° (b), θ = -45° (c) and θ = -70° (d)

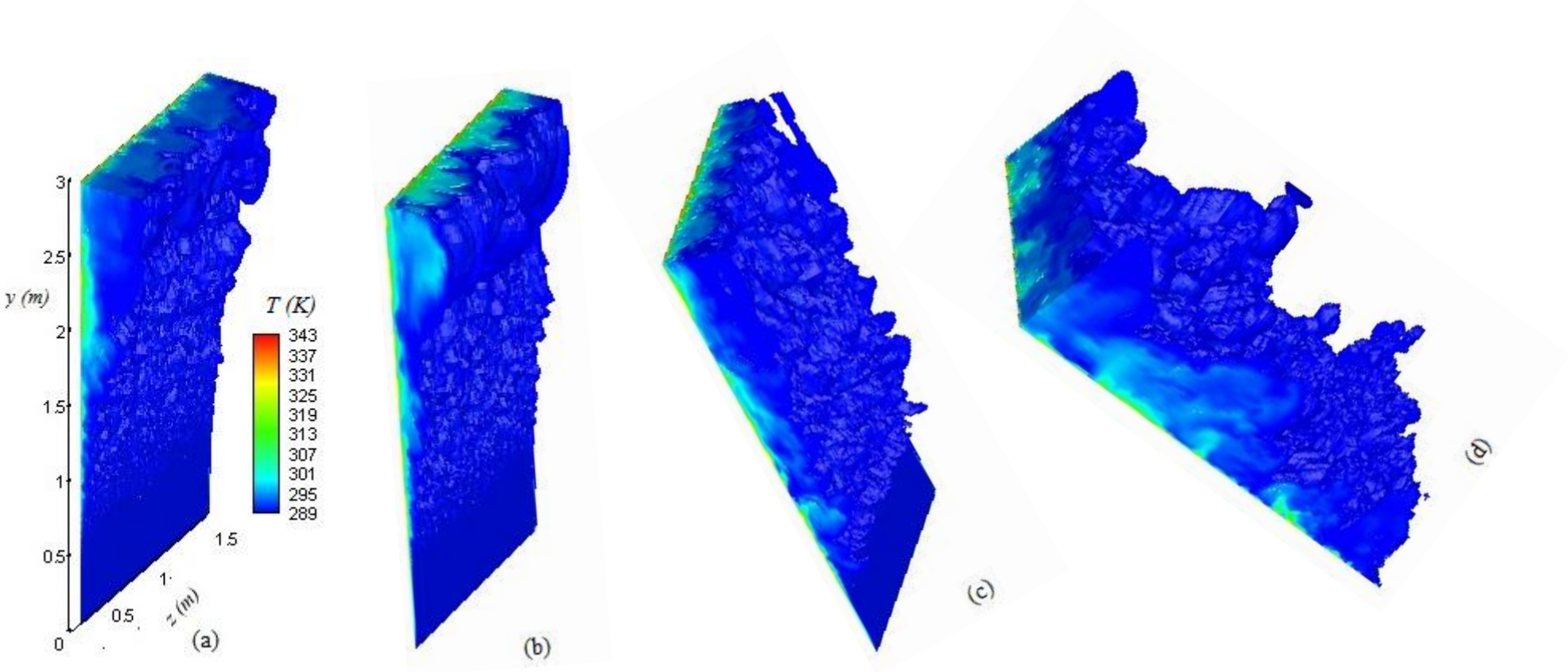

Figure 8. 6 Temprature iso-surface contour plots at θ = 0° (a), θ = -20° (b), θ = -45° (c) and θ = -70° (d)

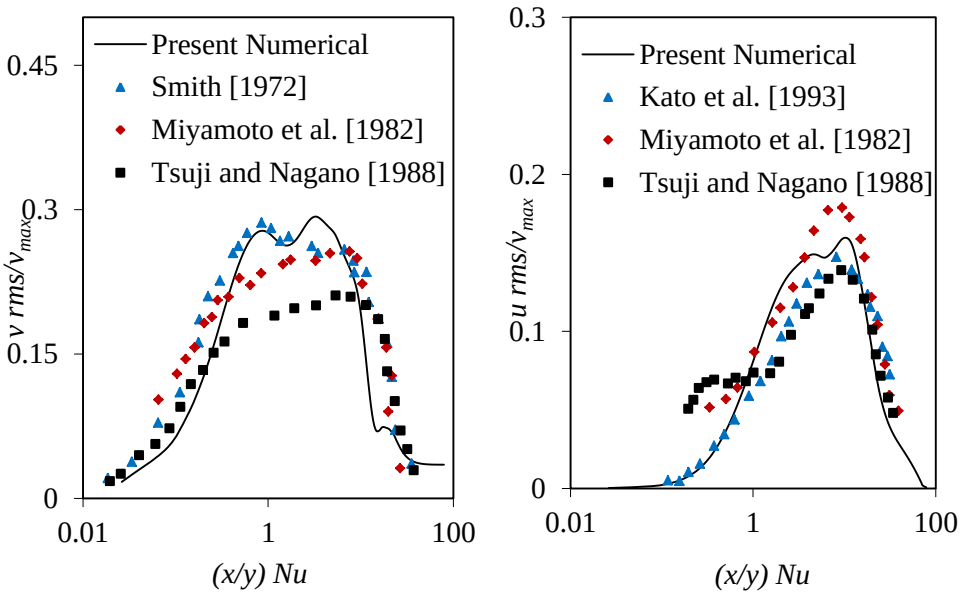

Figure 8. 7 Comparison of the *rms* of the turbulent velocity fluctuations

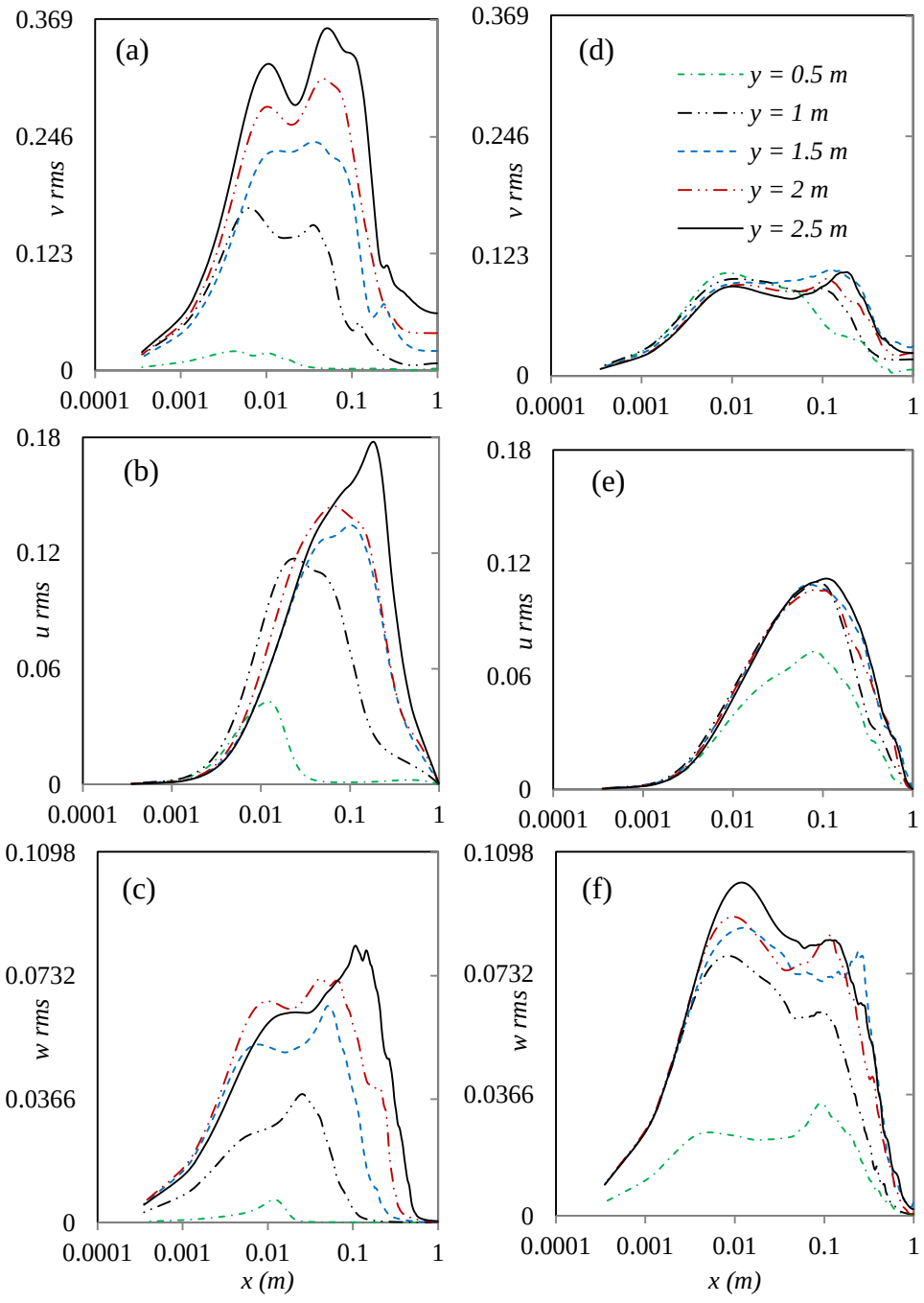

Figure 8. 8 Profiles of the velocity *rms* at θ = 0° (a-c) and θ = -70° (d-f).

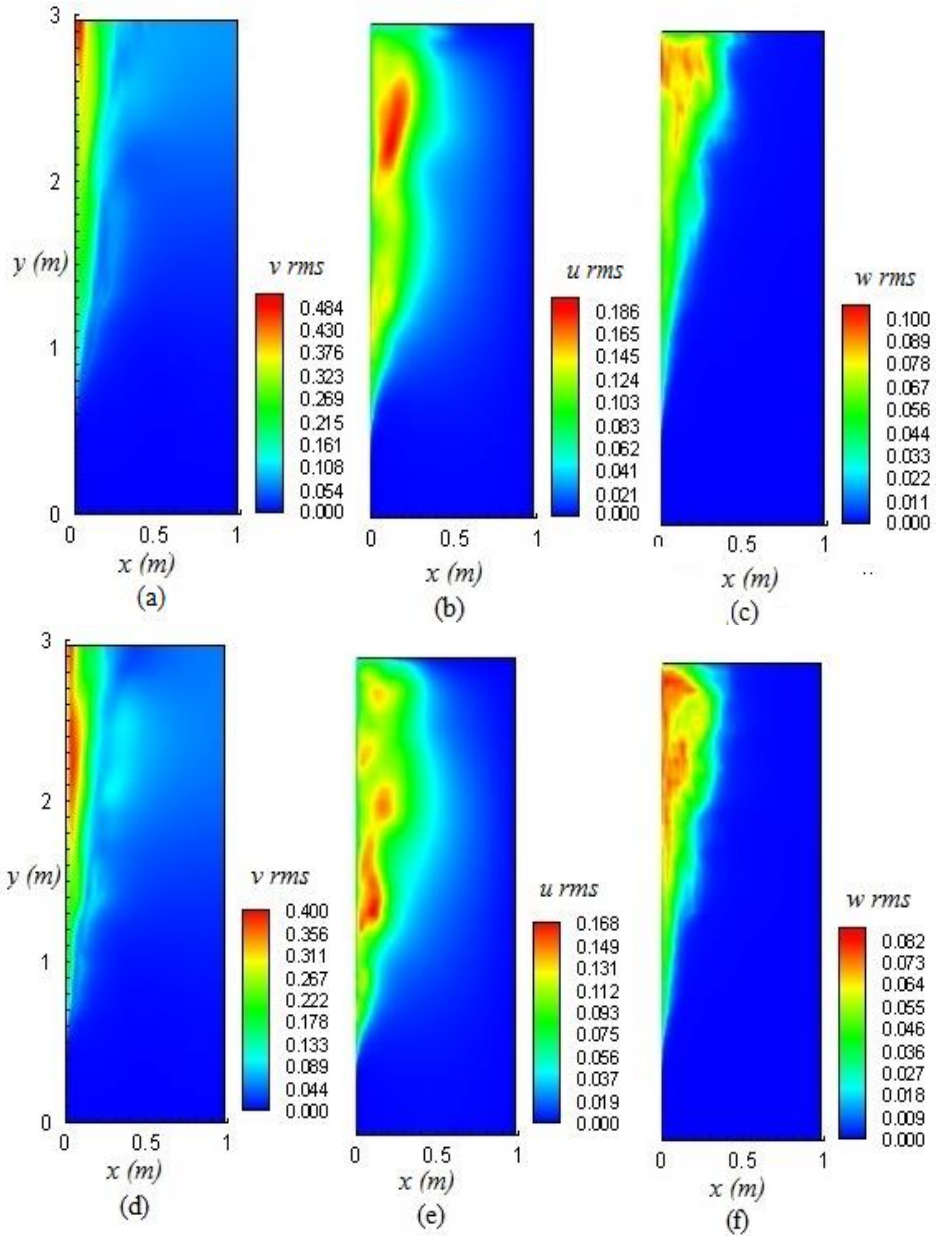

Figure 8. 9 Contours plot of the velocity *rms* at θ = 0° (a-c), θ = -20° (d-f), θ = -45° (g-i), and θ = -70° (j-l)

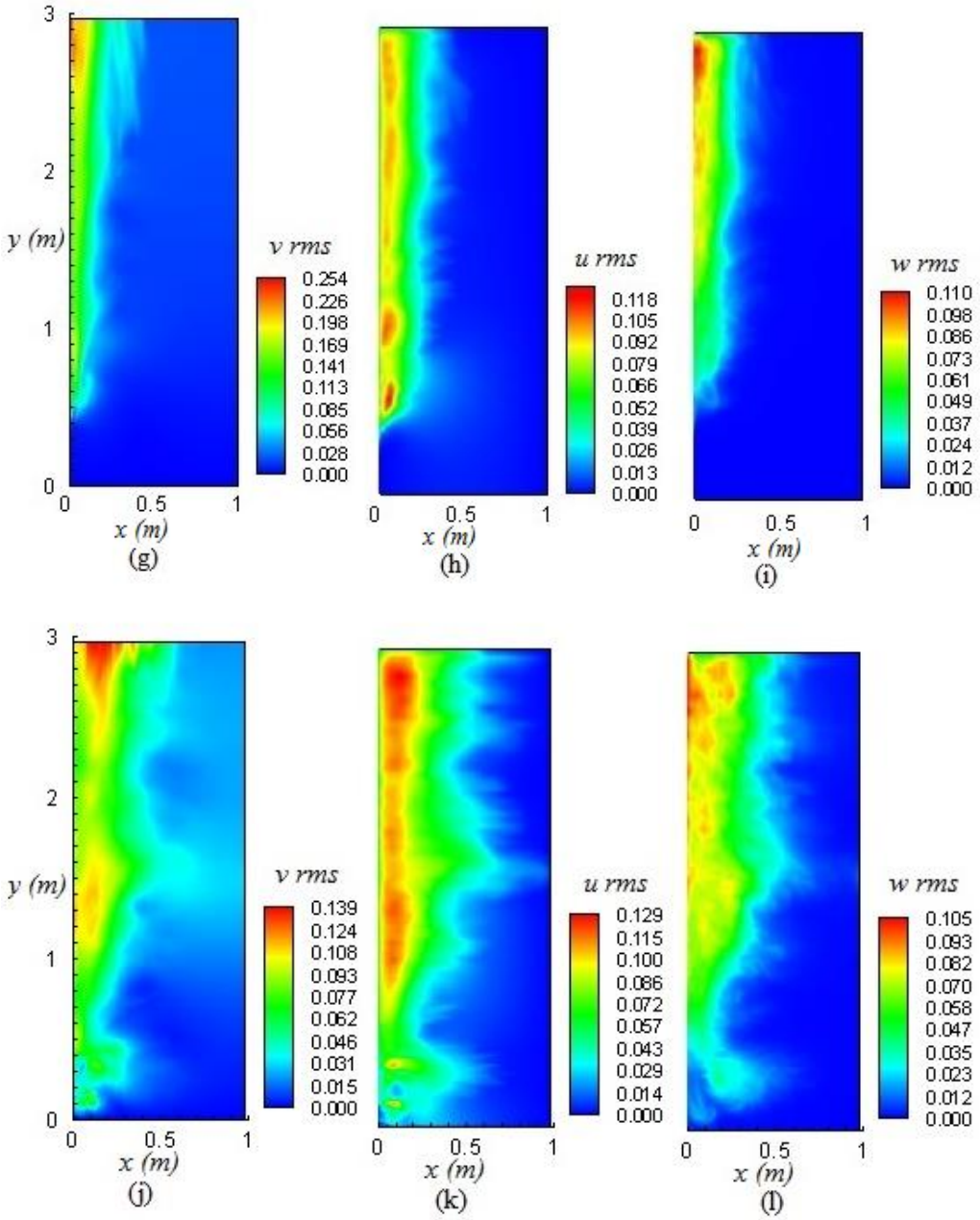

Figure 8. 9. Caption continued

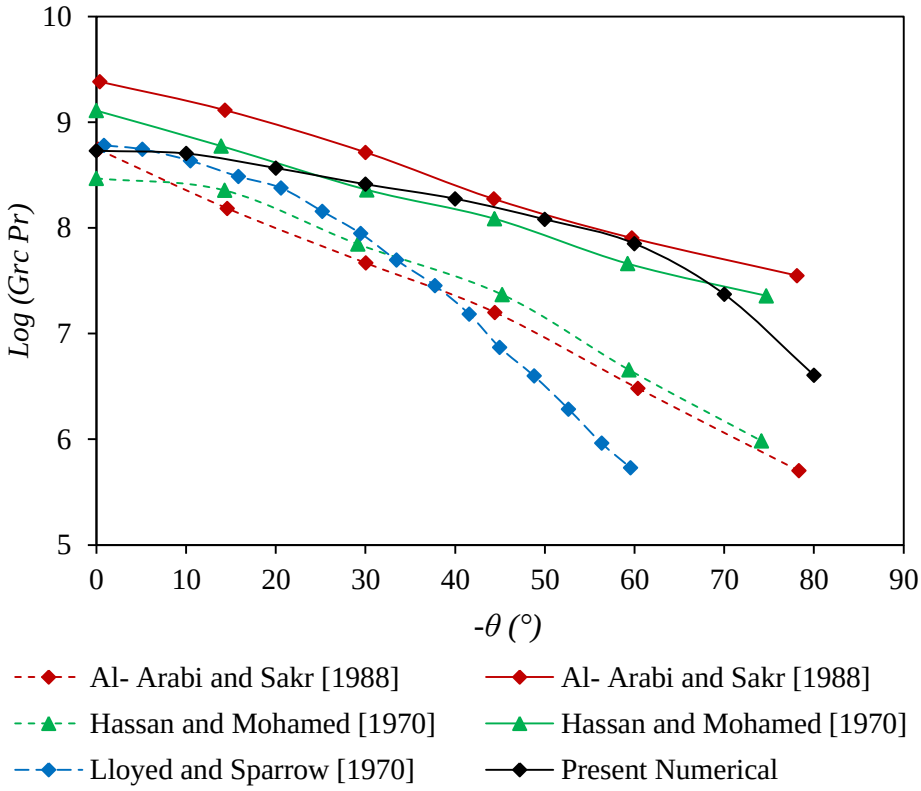

Figure 8. 10 Critical Grashof number compaired at various angular orienations of the heated plate

Chapter 9

Conclusions and future research

In this Chapter, the findings of this thesis are summarised in § 9.1 and some recommendations and suggestions on future research are made in § 9.2.

9.1. Conclusions

Natural convection from a vertical and an inclined flat plates / channel has been numerically studied. In addition, analytical results of the flow over a vertical plate have been reported. Particularly, effects of the air and plate temperatures for different angle of inclination of channel on the distribution of local thermal parameters of flow for a wide range of Grashof number are examined in the Thesis. Transitions of natural convection at various geometrical situations have been considered in the work and the studies described here have provided useful information of the characteristics of air flow and transition behaviour in a channel. The following conclusions for each of the cases studied may be drawn.

In Chapter 4 analytical and numerical result of the physical dimensional of free convection along a single vertical heated plate in the laminar and turbulent regions are studied. Attention is given to the effect of the heated boundary condition of the plate on the growth of the thickness of the boundary layer and its transition stage. The heated plated is tested under different boundary conditions: isothermal and heat flux, while the range of air temperature tested in the range of 9°C to 29°C. The conclusions from this part of the work

indicate that though both the plate and air temperature in the isothermal case have effect on the transition stage, the plate temperature has a significant effect on the transition of the flow. While, in the heat flux case the air temperature has a little effect on the transition which is largely affected by the amount of heat flux used. Some calculations of the thickness of the boundary layer in the turbulent flow are reported, and a comparison between the analytical results of our calculations and some experiments data is presented. The result indicated that the theoretical results predict satisfactorily well the behaviour of the development of the boundary layer of air on the vertical plate.

In Chapter 5 and Chapter 6 a numerical study of the natural convection in a vertical isothermal channel was studied. Attention was given to the transition stage between the laminar and turbulent regions. In addition the effects of the channel width were tested in the range b = 0.04 m to 0.45 m. Three different RANS based turbulent k-ε models namely standard, RNG and Realizable were examined in this work with a standard wall function and an enhanced wall function used in the boundary layer near the wall.

Comparison with the experimental data of Yilmaz and Fraser [2007] showed that the Realizable turbulent model with the enhanced wall function provides the less percentages of error, so they were selected to perform all the other numerical simulations in this study. Local heat flux reached its minimum further upstream of the channel and did not agree with the predictions of velocity and the turbulent kinetic energy since in a small width of channel there is not enough space available for the boundary layer to grow fully which would eventually carry the heat from the heated plate. Also the location of the transition point shifted to a higher distance towards the downstream of the channel when the channel width was increased from b = 0.04 m to 0.08 m. And, particularly, at b = 0.08 m the critical Grashof number reached its

maximum at 2.8×10^{10}. However, the transition occurred early when the channel width was increased from b = 0.10 m to 0.45 m, and the critical distance at the channel width of 0.45 m became similar to that obtained by the one vertical heated plate since the effect from the adiabatic plate at a far distance is negligible.

In Chapter 6, the development of natural convection between the two isothermal plates is reported with an interaction of the natural convection from two vertical isothermal plates is studied. Both the width of the channel and the plate temperature have major effect on the critical distance inside the channel, where a late transition occurs when the two heated plates are kept under the isothermal condition compared to the adiabatic case.

In Chapter 7 a numerical study of natural convection in an isothermal channel is studied. Attention was given to the effects of the inclination angle of the channel, which is varied from 0° to 85°. The upper plate of the channel is heated isothermally and facing downward, while the lower one is kept under the adiabatic condition. The results show that the average of heat transfer coefficient depends on both the channel width as its angle. As the width of the channel is increased, the heat transfer coefficient initially drops to a minimum value followed by an increment at a large width which related to the velocity distribution beside near the heated wall. We also find that with an increase in the channel width the location of the velocity peaks become sharp and move towards the heated wall.

Moreover, both the width and inclination of the channel have major effects on the transition stage. As the inclination angle is increased, the transition stage moves further downstream of the channel. The critical distance predicted by both the velocity and turbulent kinetic energy agrees very well, while it is

slightly over-predicted by the local heat flux as a result of the buoyancy force increasing to the normal direction of the heated plate.

Finally, In Chapter 8 numerical study of the natural convection from an isothermal plate is conducted by using a Large Eddy Simulation method. I focus on how the transition is affected by the inclination angle of the heated plate facing upward. Special attention is paid to the development of the thermal boundary layer and its process of transition from the laminar to turbulent stages. In-house developed LES-BOFFIN code has been modified and extended in this part of the study to solve the incompressible governing equations with a dynamic subgrid model. Results of the transition process of the flow agree well with experiment. With an increase in the angle the peak of the thermal and velocity boundary layers move from the near outlet of the plate for vertical case $\theta = 0°$ to the middle of the plate when $\theta = -70°$, so the thermal and boundary layers become fatter which causes an early transition.

Furthermore, the intensity of the velocity fluctuations in the boundary layer indicated that as the angle is increased the value of the velocity fluctuation *v rms* decreases in the *y* direction and the two peaks of fluctuation *v rms* move out of the heated plate, while the velocity fluctuation in *z* direction rises and the location of the peaks move to the buoyant sublayer region. The prediction of the velocity, temperature and transition stage was in good agreement with different experimental data.

9.2. Future Research

The current study has demonstrated the capabilities of various numerical methods in providing a fundamental understanding of the transition of natural convection flow on a single heated plate as well as inside a heated channel with

an effect of channel width and inclination angle. The study could be extended in future by considering the following important issues:

- Experimental data on free convection, especially on the aspect of transition, is very limited in the literature. Although we have managed to verify some of our numerical results with selected experimental and theoretical data from the literature, it is important that an experimental test rig is designed and developed in a lab for examining as well as validating the results of flow transition in different setups and orientations of channel.

- In Channel 8, LES was performed in a heated plate case. This method can be extended to study the flow transition on a channel case facing upward with a variation of its width and angular orientation.

- Study the effect of sudden heat source (low or extreme) on the development natural convection flow and transition inside a channel.

- Investigate mixed convection flow inside a multi-channel system which has potential application to the ventilation / cooling of solar photovoltaic panels. The heat transfer process in this case will also include the radiation effect.

References

Abedin, M. Z. Tsuji, T. and Hattori, Y. [2009], Direct numerical simulation for a time developing natural convection boundary layer along a vertical flat plate, *International Journal of Heat and Mass Transfer*, Vol. 52, pp. 4525-4534.

Abedin, M. Z. Tsuji, T. and Hattori, Y. [2010], Direct numerical simulation for a time developing combined convection boundary layer along a vertical flat plate, *International Journal of Heat and Mass Transfer*, Vol. 53, pp. 2113-2122.

Armfield, S, W. Patterson, J, C. and Lin, W. [2007], Scaling investigation of the natural convection boundary layer on an evenly heated plate, *International Journal of Heat and Mass Transfer Heat and Mass Transfer*, Vol. 50, pp. 1592-1602.

AL- Arabi, M. and Sakr, B. [1988], Natural convection heat transfer from inclined isothermal plates, *International Journal of Heat and Mass Transfer*, Vol. 31, pp. 559-566.

Aung, W. Feletcher, L.S. and Sernas, V. [1972], Developing laminar free convection between vertical flat plates with asymmetric heating. *International Journal of Heat and Mass Transfer*, Vol. 15, pp. 2293-2308.

Azevedo, L. F. A. and Sparrow, E. M. [1985], Natural convection in open – ended inclined channels, *Journal of Heat Transfer*, Vol. 107, pp. 893-901.

Bacharoudis, E. Vrachopoulos, M. Koukou, M. K. Margaris, D. Filios, A. E. and Mavrommatis, S. A. [2007], Study of the natural convection phenomena

inside a- wall solar chimney with one wall adiabatic and one wall under a heat flux, *Applied Thermal Engineering,* Vol. 27, pp. 2266-2275.

Badr, H. M. Habib, M. A. and Anwar, S. [2006], Turbulent natural convection in vertical parallel-plate channels, *Heat and Mass Transfer,* Vol. 43, pp. 73-84.

Baskaya, S. Aktas, M. K. and Onur, N. [1999], Numerical simulation of the effects of plate Separation and Inclination of heat transfer in buoyancy driven open channels, *Heat and Mass Transfer,* Vol. 35, pp 273-280.

Bayley, F.J. [1955], An analysis of turbulent free convection heat transfer, *Proceedings of the Institution of Mechanical Engineers,* Vol. 169, pp. 361-370.

Bejan, A. [1995]. *Convection Heat Transfer*, New York, Wiley.

Ben-Mansour, R. Habib, M, A. Badr, H, M. and Anwar, S. [2006], Comparison of different turbulent models and flow boundary conditions in predicting turbulent natural convection in a vertical channel with isoflux plates, *The Arabian Journal for Science and Engineering*, Vol. 32, pp. 191-218.

Black, W. Z. and Norris, J. K. [1975], The thermal structure of free convection turbulence from inclined isothermal surfaces and its influence heat transfer, *International Journal of Heat and Mass Transfer,* Vol. 18, pp. 43-50.

Bianco, N. Morrone, B. Nardini, S. and Naso, V. [2000], Air natural convection between inclined parallel plates with uniform heat flux at the walls, *International Journal of Heat and Technology,* Vol. 18, pp. 23-45.

Bodia, J.R. and Osterle, J.F. [1962], The development of free convection between heated vertical plates. *Journal of Heat Transfer*, Vol. 84, pp. 40-44.

Burch, T. Rhodes, T. and Achary, S. [1985], Laminar natural convection between finitely conducting vertical plates, *International Journal of Heat and Mass Transfer*, Vol. 28, pp. 1173-186.

Burek, S.A.M. and Habeb, A. [2007], Air flow and thermal efficiency characteristics in solar chimneys and Trombe Walls, *Energy and Building*, Vol. 39, pp. 128-135.

Cadafalch, J. Oliva, A. Van der Graaf, G. and Albets, X. [2003]. Natural convection in a large inclined channel with asymmetric heating and surface radiation, *Journal of Heat Transfer*, Vol. 125, pp. 812-820.

Charles, Y. W. and S. A. Vedat [1968], An experimental investigation of Turbulent natural convection in air at low pressure along a vertical heated flat plate, *International Journal of Heat and Mass Transfer*, Vol. 11, pp. 397-406.

Cheesewright, R. [1967], Turbulent natural convection from a vertical plane surface,*Technical Report*, No. 05031-8-T, pp. 1-20.

Cheesewright, R. and Mirzai, M. H. [1988], The correlation of experimental velocity and temperature data for a turbulent natural convection boundary layer, 2*th UK National Conference on Heat Transfer*, pp. 78-89.

Chen, Z. D. Bandopadhayay, P. Halldorsson, J. Byrijalsen, C. Heiselberg, p. [2003], An experimental investigation of a solar chimney model with uniform wall heat flux , *Building and Environment*. Vol. 38, pp. 893-906.

Churchill, S. W. and Chu, H. H. S. [1975], Correlating Equations for Laminar and Turbulent Free Convection from a Vertical Plate, *International Journal of Heat and Mass Transfer*, Vol. 18, pp. 1323-1329.

Churchill, S. W. and Ozoe, H. [1973], A correlation for laminar free convection from a vertical plate, *Journal of Heat Transfer,* Vol. 95, pp. 540-541.

Davidson, L. [1990], Calculation of the turbulent buoyancy driven flow in a rectangular cavity using an efficient solver, *Numerical Heat Transfer, Part A*, Vol. 18, pp. 129-147.

Di Mare, L. and Jones, W. P. [2003], LES of turbulent flow past a swept fence, *International Journal of Heat and Fluid Flow*, Vol. 24, pp. 606-615.

Eckert, E. R. G. and Jackson, T. W. [1950], Analysis of turbulent free convection boundary layer on vertical plate, *Technical Report, NACA TN 2207*, pp. 255-261.

Elenbaas, W. [1942], *Heat dissipation of parallel plates by free convection*, Laboratoria, N. V. Philips, pp. 1-28.

Fedorov, A, G. and Viskanta, R. [1997], Turbulent natural convection heat transfer in an asymmetrically heated, vertical parallel-plate channel, *International Journal of Heat and Mass Transfer*, Vol. 40, pp. 3849-3860.

Fujii, T. Takeuchi, M. Fujii, T. Suzaki, K. and Uehara, H. [1970], Experiments on natural convection heat transfer from the outer surface of a vertical cylinder to liquids, *International Journal of Heat and Mass Transfer,* Vol. 13, pp. 735-770.

Gebhart, B. [1973], Instability, Transition, and Turbulence in Buoyancy-Induced flows, *Annual Review of Fluid Mechanics*, Vol. 5, pp. 213-246.

Griffiths, E. and Davis, H. A. [1922], The transmission of heat by radiation and convection, *Food Investigation Board,* Special Report. No. 9.

Hassan, k. and Mohamed, S. A. [1970], Natural convection from isothermal flat surfaces, *International Journal of Heat and Mass Transfer,* Vol. 13, pp. 1873-1886.

Hatami, N. and Bahadorinejad, M. [2008], Experimental determination of natural convection heat transfer coefficient in a vertical flat-plate solar air heater, *Solar Energy,* Vol. 10, pp. 1-8.

Henkes, R. A. W. M. [1990], Natural convection boundary layers, PhD. Thesis Delft University of Technology, Delft.

Henkes, R. A. W. M. and Hoogendoorn, C. J. [1989], Comparison of turbulence models for the natural convection boundary layer along a heated vertical plate, *International Journal of Heat and Mass Transfer,* Vol. 32, pp. 157-169.

Holman, J. P.[2002], *Heat transfer,* 9th ed, McGraw Hill Companies.

Incropera, F. P. Dewitt, D. P. Bergman, T. L. and Lavine, A. S. [2001], *Fundamental of Heat and Mass Transfer*, 5th ed, John Wiley and sons.

Ioan, P. and Derek I. [2001], *Convective Heat Transfer Mathematical and Computational Modelling of Viscous Fluids and Porous Media*, First edn, Elsevier Science, UK.

Jakob, M. [1949], *Heat Transfer*, John Wiley and Sons.

Jones, W. P. and Paul, M. C. [2006]. Combination of DOM with LES in a gas Turbine combustor, *International Journal Engineering Science,* Vol. 43, pp. 379-397.

Kader, B. [1981], Temperature and concentration profile in fully turbulent boundary layers, *International Journal of Heat and Mass Transfer,*Vol. 24, pp. 1541-1544.

Kakac, S. and Y. Yener [1995], *Convective Heat Transfer*, Second edn, CRC Press LLC, United State.

Kaiser, A.S. Zamora, B. and Viedma, A. [2004], Correlation for Nusselt number in natural convection in vertical convergent channels at uniform wall temperature by a numerical investigation, *International Journal of Heat and Fluid Flow*, Vol. 25, pp. 671-682.

Katoh, Y. Miyamoto, M. Kurima, J. and Kaneyasu, S. [1991], Turbulent free convection heat transfer from vertical parallel plates, *JSME International Journal*, Vol. 34, pp 496-501.

Kays, W. M. and Crawford, M. E. [1980], *Convection heat and mass transfer*, 2 ed. McGraw Hill Companies.

Kershaw, D. S. [1978], The Incomplete Cholesky-Cojugate Gradient method for the iterative solution of systems, *Journal of Computational Physics*, Vol. 26, pp 43-65.

Kierkus, W. T. [1968], An analysis of laminar free convection flow and heat transfer about an inclined isothermal plate, *International Journal of Heat and Mass Transfer*, Vol. 11, pp 241-253.

Kimura, F. Kitamura, K. Yamaguchi, M. and Toshihiko, A. [2003], Fluid flow And heat transfer of natural convection adjacent to upward-facing inclined heated plates, *Heat Transfer – Asian Research*, Vol. 32, pp 378-291.

Kimura, F. Yoshioka, T. Kitamura, K. Yamaguchi, M. and Toshihiko, A. [2002], Fluid flow and heat transfer of natural convection at slightly inclined upward facing heated plate, *Heat Transfer – Asian Research,* Vol. 31, pp 362-375.

Koleshko, S. B, Lapin, Y. V. and Chumakov, Y. S. [2005], Turbulent free convection boundary layer on a vertical heated plate Regularities of the temperature layer, *High Temperature,* Vol. 43, pp. 429-440.

Komori,K. Kito,S. Nakamura,T. Inaguman,Y. and Inagaki,T. [2001], Fluid flow and heat transfer in transition process of natural convection over an inclined plate, *Heat Transfer - Asian Research*, Vol. 30, pp. 648-689.

Lam, C. and Bremhorst, K. [1981], Modified form of k–ε model for predicting wall turbulence. *Journal of Fluid Engineering,* Vol. 103, pp. 456-460.

Lau, G. E. Yeoh, G. H. Timchenko, V. and Reizes, J. A. [2011], Large-eddy simulation of turbulent natural convection in vertical parallel-plate channels, *Numerical Heat transfer, Part B,* Vol.59, pp. 259-287.

Launder, B, E. and Sharma, B, I. [1974], Application of the energy-dissipation model of turbulence to the calculation of flow near a spinning disc, *Letters in Heat and Mass Transfer*, Vol. 1, pp. 131-138.

Launder, B, E. and Spalding, D, B. [1972], *Lectures in mathematical models of turbulence,* Academic Press, London, England.

Leonard, A. [1974], Energy cascade in Large-Eddy Simulations of turbulent fluid flows, *Adv Geophys*, pp. 237-248.

Levy, S. [1955], Integral method in natural - convection flow, *Journal of Applied Mechanic.* Vol. 22, pp. 515-522.

Lindon, C. T. [2000], *Heat Transfer*, Second edn, Capstone Publishing Corporation, United State.

Liping, W. and Angui, L. [2004]. A numerical study of vertical solar chimney for enhancing stack ventilation in buildings , *The 21st Conference on Passive and Low Energy Architecture.* Eindhoven, The Netherlands, pp. 1-5.

Lloyd, R. J. and Sparrow, E. M. [1970], On the instability of natural convection flow on inclined plates, *Journal of Fluid Mechanics,* Vol. 42, pp. 465-470.

Louis, C. B. [1993], *Convection heat transfer,* 2ed, John Wiley and sons.

Manca, O. Nardini, S and Naso, V. [1992], Experimental analysis of natural convection in a tilted channel, *11the Australasian Fluid Mechanics Conference*, University of Tasmania, Hobart, Australia, pp. 131-134.

Mickle, F. and Marient, S. T. [2009], *Convective Heat Transfer,* First edn, John Wiley and ISTE, UK and USA.

Miyamoto, M. Kato, Y. and Kurima, J. [1983], Turbulent free convection heat transfer from vertical parallel plates in air, *NII - Electronic Library service, the Japan Society of Mechanical Enginners*, Vol. 34, pp. 1-7.

Miyamoto, M. Katoh, Y. Kurima, J. and Saki, H. [1986], Turbulent free convection heat transfer from vertical parallel plates, *proceeding of the International Heat Transfer, conference 8th*. Vol. 4, pp. 1593-1598.

Miyamoto, M. Kajino, H. Kurima, J. and Takanami, I. [1982], Development of Turbulent characteristics in a vertical free convection boundary layer, *7th International Heat Transfer Conference*, pp. 323-328.

Miyatake, O. and Fujii, T. [1972], Free convective heat transfer between vertical plates-One plate isothermally heated and the other thermally insulated, *Heat Transfer-Japanese Research*, Vol. 1, pp. 30-38.

Morinishi, Y. [1995], Conservation properties of finite difference schemes for Incompressible Flow, *Centre for Turbulence Research*, pp. 121-132.

Nicholas, A, S. and Markatos, C, G. [1978], Transient flow and heat transfer of liquid sodium coolant in the outlet plenum of a fast nuclear reactor, *International Journal of Heat and Mass Transfer*, Vol. 21, pp. 1565-1579.

Oleg, G. M. and Pavel, P. K. [2005], *Free-Convective Heat Transfer*, 1st edn, Springer, Berlin.

Onur, N. and Aktas, M. K. [1998], An experimental study on the effect of opposing wall on natural convection along an inclined hot plate facing downward, *International Communications in Heat and Mass Transfer*, Vol. 25, pp. 389-397.

Onur, N. Sovrioglu, M. and Aktas, M. K. [1997], An experimental study on the natural convection heat transfer between inclined plates (lower plate isothermally heated and the upper plate thermally isolated as well as unheated), *Heat and Mass Transfer*, Vol. 32, pp. 471-475.

Oosthuizen, P. H. and Naylor, D. [1999]. *Introduction to Convective Heat Transfer Analysis*, 1st edn, McGraw-Hill, United State.

Oosthuzien, P.H. [1984], A numerical study of laminar free convection flow through a vertical open heated plane duct. *Fundamentals on Natural Convection - Electronic Equipment Cooling, Vol.* 32, pp. 41-48.

Patankar, S.V. [1980], *Numerical Heat Transfer and Fluid Flow*, McGraw-Hill, New York.

Paul, M. C. [2008], Performance of the various Sn approximations of DOM in a 3D combustion chamber, *Journal of Heat Transfer,* Vol. 103.

Paul, M.C. and Molla,M. M. [2012], Investigation of physiological pulsatile flow in amodel arterial stenosis using large-eddy and direct numerical simulations, *Applied Mathematical Modelling*, Vol. 36, pp 4393-4413

Paul, S. C. Paul, M. C. and Jones, W. P. [2006], Large eddy simulation for turbulent non- premixed fuel rich combustion in a cylindrical combustor, *In, P. Wesseling, E. Onate and J. Periaux Eds. Proceedings of the European Conference on Computational Fluid Dynamics (ECCOMAS CFD), 5-8 September, The Netherlands*, pp.1-15.

Piomelli, U. and Liu, J. [1995], Large-eddy simulation of rotating channel flows using a localized dynamic model, *Physics of Fluids*, Vol. 7, pp. 839-848.

Reynolds, W. C. [1987], Fundamentals of turbulence for turbulence modelling and simulation, *Lecture notes for von karman institute agrad report* 755.

Rich, R. B. [1953], An investigation of heat transfer from an inclined flat plate in free convection, *International Journal of Heat and Mass Transfer*, Vol. 11, pp 241-253.

Said, S. A. M., Habeb, M. A. and Anwar, S. [2005a], Turbulent natural convection between inclined isothermal plates, *Computer and Fluids*, Vol. 34, pp 1025-1039.

Said, S. A. M. Habeb, A. Badr, H. M. and Anwar, S. [2005b], Numerical investigation of natural convection inside an inclined parallel walled channel, *International Journal for Numerical Methods in Fluids*, Vol. 49, pp. 569-582.

Saunders, O. A. [1936], Effect of pressure upon natural convection in air, *Proceedings of the Royal Society of London.* Series A, *Mathematical and Physical Sciences,* Vol. 157, pp. 278-291.

Schmidt, E. and Schumann, U. [1989], Coherent Structure of the Convective Boundary Layer Derived from Large-Eddy Simulations, *Journal of Fluid Mechanics*, Vol. 200, pp. 511-562.

Sedov, L. S. [1959], Similarity and dimensional Methods in mechanics, *Academic Press, New York Smith*, R. R. Thesis University London.

Shih, T, H. Liou, W, W. Shabbir, A. Yang, Z. and Zhu, J. [1995], A new *k-ε* eddy viscosity model for high Reynolds number turbulent flows, *Computers and Fluids*, Vol. 24, pp. 227-238

Simon, O. [1952], An analysis of laminar free convection flow and heat transfer about a flat plate parallel to the direction of the generation body force, *NACA Technical Report* 1111, pp. 63-79.

Smagorinsky, J. [1963], General Circulation Experiments with the Primitive Equations-I. The Basic Experiment, *Monthly Weather Review*, Vol. 91, pp. 99-164.

Smith, R. R. [1972], phy. D. Thesis Univ. London.

Sparrow, E. M. [1955], Laminar free convection from a vertical plate with wall heat flux or Prescribed non uniform wall temperature, *NACA Technical Report* 3508.

Sweby, P. K. [1984], High Resolution Schemes Using Flux Limiters for Hyperbolic Conservation Laws, *SIAM Journal on Numerical Analysis*, Vol. 21, pp. 995-1011.

Taofeek, F. Ayinde, T. F. Said, S. A. M. and Habib, M. A. [2008], Turbulent natural convection flow in a vertical channel with anti-symmetric heating. *Heat Mass Transfer*, Vol. 44, pp. 1207-1216.

Thomson, J. F. Thames, F. and Mastin, C. [1974], Automatic numerical generation of body-fitted curvilinear coordinates system for field containing any number of arbitrary two dimensional bodies, *Journal of Computational Physics*, Vol. 15, pp. 299-319.

To, W.M. and Humphrey A.C. [1986], Numerical simulation of buoyant, turbulent flow—I. Free convection along a heated, vertical, flat plate. *International Journal of Heat and Mass Transfer*, Vol. 29, pp. 573-592.

Tritton, D. J. [1963a], Turbulent free convection above a heated plate inclined at a small angle to the horizontal, *Journal of Fluid Mechanics*, Vol. 16, pp 282-312.

Tritton, D. J. [1963b], Transition to turbulence in the free convection boundary layers on an inclined heated plate, *Journal of Fluid Mechanics*, Vol. 16, pp 417-435.

Tsuji, T. and Kajitani, T. [2006], Turbulence characteristic and heat transfer enhancement of a natural convection boundary layer in water along a vertical

flat plate, *13th International Heat Transfer Conference,* Sydney, TRB08 of CD-ROM.

Tsuji, T. and Nagano, Y. [1988a], Characteristics of a turbulent natural convection boundary layer along a vertical flat plate, *International Journal of Heat and Mass Transfer,* Vol. 31, pp.1723-1734.

Tsuji, T. and Nagano, Y. [1988b], Turbulence measurements in a natural convection boundary layer along a vertical flat plate, *International Journal of Heat and Mass Transfer,* Vol. 31, pp. 2101-2111.

Versteeg, H., K. and Malalasekera, W. [2007], *An introduction to Computational fluid dynamics*, Pearson Education Limited.

Vliet, G. C. and Ross, D. C. [1975], Turbulent natural convection on upward and downward facing inclined constant heat flux surfaces, *Journal of Heat Transfer,* Vol. 97, pp. 549 - 554.

Warner, C. Y. and Arpaci, V. S. [1968], An experimental investigation of turbulent natural convection in air at low pressure along a vertical heated flat plate, *International Journal of Heat and Mass Transfer,* Vol. 11, pp. 397-406.

Wille, M. [1997], Large Eddy Simulation of Jets in Cross Flows, *PhD thesis*, Department of Chemical engineering and Chemical Technology, Empirical College London

William, K. Michael, C. and Bernhard, W. [2005], *Convective Heat and Mass Transfer*, Fourth edn, McGraw-Hill, United States.

Wilson, M.J. and Paul, M.C. [2011], Effect of mounting geometry on convection occurring under a photovoltaic panel and the corresponding efficiency using CFD, *Solar Energy*, Vol. 85, pp. 2540-2550.

Yakhot, V. Orszag, A, S. Thangam, S. and Speziale, G. C. [1992], Development of turbulence models for shear flows by a double expansion technique, *Physics of Fluids*, Vol. 4, pp. 1510-1521.

Yan, Z. H. and Nilsson, E. E. A. [2005], large eddy simulation of natural convection along a vertical isothermal surface, *Heat and Mass Transfer*, Vol. 41, pp .1004-1013.

Yang, Z. and Shih, T, H. [1993], New Time Scale Based $k-\varepsilon$ Model for Near-Wall Turbulence, *American Institute of Aeronautics and Astronautics Journal*, Vol. 31, pp. 1191-1198.

Yilmaz, T. and Fraser, S. M. [2007], Turbulent natural convection in a vertical parallel-plate channel with asymmetric heating, *Int. Journal of Heat and Mass Transfer*, Vol. 50, pp. 2612-2623.

Yilmaz, T. and Gilchrist, A. [2007], Temperature and velocity field characteristics of turbulent natural convection in a vertical parallel-plate channel with asymmetric heating, *Heat and Mass Transfer*, Vol. 43, pp. 707-719.

Yuan, X. Moser, A. and Suter, P. [1993], Wall functions for numerical simulation of Turbulent natural convection along vertical plates, *International Journal of Heat Mass Transfer*, Vol. 36, pp. 4477-4485.

Zamora, B. and Hernandez, J. [2001], Influence of upstream conduction on the thermally optimum spacing of isothermal, natural convection-cooled vertical

plates arrays, *International Communication in Heat and Mass Transfer*, Vol. 28, pp 201-210.

Zamora, B. and Kaiser, A. S. [2009], Optimum wall-to-wall spacing in solar chimney shaped channels in natural convection by numerical investigation, *Applied Thermal Engineering*, Vol. 29, pp. 762-769.